Technische Universität München
TUM School of Computation, Information and Technology

Coherent Interaction of Pulsed Light with a Single Quantum Two-Level System

Katarina Boos

Vollständiger Abdruck der von der TUM School of Computation, Information and Technology der Technischen Universität München zur Erlangung einer

Doktorin der Naturwissenschaften (Dr. rer. nat.)

genehmigten Dissertation.

Vorsitz: Prof. Dr.-Ing. Christian Jirauschek

Prüfende der Dissertation:

1. Prof. Dr. Kai Müller
2. Prof. Jonathan J. Finley, Ph.D.
3. Dr. Carlos Antón-Solanas

Die Dissertation wurde am 20.06.2024 bei der Technischen Universität München eingereicht und durch die TUM School of Computation, Information and Technology am 25.11.2024 angenommen.

Quantum Optics with Quantum Dots.

To those who advocate for equity and fairness in academia, and for a healthier scientific environment.

Abstract

The interaction between light fields and quantum systems stands as a cornerstone in both quantum optics and its applications. While the interplay is of high interest from a fundamental point of view, understanding basic light-matter coupling brings about new ideas and approaches to tackle current challenges in photonic quantum technological applications. Here, optical control and excitation of qubits which commonly relies on coupling of coherent resonant or near-resonant light pulses to two-level systems are of high relevance and a key point in current research. Especially efficient coherent excitation is becoming increasingly relevant with advancing quantum technology, as scaling to multiple qubits or several gate operations requires higher efficiency, brightness and coherence.

In our work, we contribute to and investigate the topic from two different perspectives: We extend the well-studied phenomena of dressed states and the Mollow triplet, arising from a continuous-wave light field coupling to a two-level system, by investigating the dressed states and their emission for a two-level system interacting with short Gaussian pulses, by employing a semiconductor quantum dot as the experimental platform. Related to the Mollow triplet yet fundamentally different, this dynamical Mollow emission spectrum has been studied so far only theoretically in detail, lacking clear experimental proof and confirmation. Our findings reveal the emergence of multiple sidepeaks, as theoretically predicted, with their number controllable by excitation pulse area and their spectral width and detuning determined by the pulse intensity and duration. Further insight into the emission characteristics is given through detuning-dependent measurements, revealing close alignment to the Mollow triplet under continuous-wave excitation with finite detuning. In addition, we provide theoretical calculations of the spectra showing very good agreement with our experimental results.

Furthermore, we investigate the recently proposed and in a proof-of-principle experiment demonstrated swing-up excitation technique in detail which promises to solve challenges currently existing for established excitation techniques. Bracht *et al.* theoretically describe a scheme which allows for spectral isolating the emission from the excitation while being intrinsically coherent by finding excitation resonances

for a two-level system with a specific combination of two far red-detuned pulses. We confirm the operational success and demonstrate the coherent nature of the swing-up technique in experiment. Additionally, we systematically explore the multi-dimensional parameter space of the two excitation pulses to analyze their impact on the excitation fidelity and the feasibility of the scheme in experiments employing quantum dots. As highly relevant for applications, we evaluate the scheme's performance as an excitation method for generating high-quality single photons. The swing-up scheme itself proves highly effective in generating photons with nearly perfect single-photon purity. However, the observed indistinguishability in the studied sample is constrained by the influence of high excitation powers on the semiconductor environment of the quantum dot.

Tracing the mechanism of the scheme back to dynamically dressed states, the strong interplay between current research in fundamental quantum optics and novel applications in photonic quantum technologies becomes evident.

Contents

Chapter 1

Advancing quantum technologies through fundamental light-matter interaction

Quantum optics is a key aspect of modern physics and embodies an area in which the classical laws of electromagnetism merge with the intriguing principles of quantum mechanics [1, 2, 3]. Over the past century, remarkable discoveries in this field have been made that shed light on the fundamental principles of the interaction between light and matter at the quantum level. Since the beginning of the 20$^{\text{th}}$ century, research into the interactions between light and matter at the quantum level has provided deep insights into the fundamental nature of our universe. From the groundbreaking work of pioneers such as Max Planck and Albert Einstein, who laid the foundation with their revolutionary theories and discoveries on the quantization of energy through the blackbody radiation [4, 5] and the photoelectric effect [6, 7], to today's efforts to unravel the mysteries of quantum entanglement [8, 9] and teleportation [10, 11], quantum optics has continuously pushed the boundaries of human understanding.

One of the fascinating phenomena at the heart of quantum optics is resonance fluorescence [12, 13, 14, 15], where a quantum emitter or two-level system (TLS) coherently interacts with a resonant light field, emitting light with specific characteristics in the time and frequency domain [16, 17, 18, 19, 20]. This process reveals basic phenomena like spontaneous emission, photon antibunching, and coherent population trapping, providing valuable insights into the dynamics of quantum systems [21, 22, 23, 24, 25, 26]. Despite significant progress, the intricate interplay between quantum states of light and a single TLS is a constant challenge, demonstrating that not everything is yet fully understood in this field. As an example, dressed states under continuous-wave

(cw) excitation of a single TLS have been well-studied [12, 17, 27, 28, 29, 30, 31], while emission under pulsed resonant excitation has not been investigated experimentally in detail and thus fully understood [32, 33, 34, 35, 36, 37, 38], even though pulsed optical excitation of TLSs if fundamental for photonic quantum technologies [39, 40, 41, 31]. Resonance fluorescence continues to be an active area of research, driving the exploration of the coherent dynamics of quantum systems and their implications for emerging quantum technologies.

Meanwhile, principles of quantum optics form the basis for photonic quantum technologies, enabling the development and implementation of novel devices with transformative capabilities [42, 43, 44, 45, 46]. From quantum communication and cryptography [47, 48], where the security of information and efficiency of transmission depend on purity and coherence of the photonic quantum states, to quantum computing and sensing [49, 50, 45, 51, 52], where quantum coherence and the quantum mechanical interplay between individual qubits lead to unprecedented computing power and precision, photonic quantum technologies promise to reshape the landscape of information processing and scientific research. Utilizing the quantum properties of photons and their interactions with matter, a variety of devices and systems with game-changing effects are being developed. Despite notable achievements, including quantum key distribution protocols and quantum communication networks over 4600 km [53, 48], introduction of photonic quantum gates [54, 51] and the outperformance of classical computers [46] there remains significant scope for further exploration and optimization.

The understanding of optical excitation schemes is crucial for the advancement of both quantum optics and photonic quantum technologies. These schemes determine the generation and manipulation of quantum states in photonic systems and influence their coherence and emission characteristics. Using the insights from quantum optics, tailored excitation schemes for specific applications have been optimized and bridge the gap between theory and experiment. However, non of the state-of-the-art excitation schemes such as cross-polarized resonant excitation [55, 56], phonon-assisted excitation [57, 58, 59], excitation via the p-shell [60, 61], dichromatic excitation [62, 63], or excitation via the biexciton [64, 65, 66] yet offers everything: Coherence, spectral filtering to isolate emission from excitation, good optical properties of the emitted photons, applicability to any TLS and no restriction of the polarization-degree of freedom [17, 67, 16, 68, 69, 65, 70]. Optical excitation schemes play an important role in shaping the performance of photonic quantum devices and require deeper understanding and optimization for improved functionality.

Among the countless quantum emitters that populate the experimental landscape, individual quantum dots (QDs) are proving to be promising candidates, offering unparalleled insights into the quantum world [44, 71, 72, 73] that earned them the

Nobel Prize in Chemistry in 2023 [74]. With their unique optical properties and controllability [41, 75, 76, 77], including discrete energy levels and strong light-matter interaction, they are an ideal platform for investigating fundamental quantum phenomena and practical applications [44, 78, 65, 79]. By integrating single QDs into photonic devices, researchers gain unprecedented control over individual quantum systems, enabling advances in quantum information processing and communication, with QDs as single-photon sources [80, 81, 78, 65, 79], spin qubit systems [82, 83] or as the fundament for generating complex entangled states [84, 85, 86, 87, 88].

In this work, we focus on the investigation of novel yet fundamental phenomena in a single InGaAs QD under pulsed excitation with one resonant and two detuned light fields, respectively. Exploring the dynamics of resonance fluorescence under resonant excitation with finite Gaussian pulses experimentally, we unravel the coherent interplay between a single quantum TLS and a pulsed external light field. We thereby extend the detailed research on dressed states and the Mollow triplet from a cw to a pulsed light field, presenting the first experimentally observed full emission spectrum of the dynamical Mollow and its characteristics. Furthermore, we experimentally explore the recently proposed swing-up excitation technique by Bracht *et al.* [89] which hold great promise for optical excitation and control of qubits in quantum technological applications. By addressing key challenges in fundamental quantum optics and optical excitation, our research aims to deepen the understanding of light-matter interaction and advance the field of photonic quantum technologies towards practical applications and ultimately transformative advances in quantum information processing and communication.

The following thesis is structured in five main chapters; after have given an introduction to quantum optics and photonic quantum technologies with a focus on resonance fluorescence and single self-assembled QDs, and thereby putting this work into the context of state-of-the-art research, in **Chapter 1**, **Chapter 2** focuses on the fabrication and characterization of the investigated sample which is the basis of this work. It includes a detailed description of how a single QD is controlled and used as a TLS. In **Chapter 3** we explore fundamental quantum optics, i.e. the interaction of a QD with a resonant light field. After a theoretical description of the interplay between a TLS and a light field, we look at dressed states under cw excitation and the well-studied Mollow triplet. We then extend this analysis to the emission characteristics under pulsed excitation which have so far not been observed in experiment and look at the characteristics of the multi-peaked spectrum with changing excitation parameters [90]. We continue with a more application-focused study and look at how the recently proposed swing-up excitation technique [89] performs in comparison to

resonance fluorescence using a single QD [91] in **Chapter 4**. Here we investigate excitation resonances in the excitation parameter space for two far red detuned excitation pulses and study the single-photon properties. A summary of our work and outlook at next steps and follow-up experiments conclude this work in **Chapter 5**. We suggest time-resolved analysis of the dressed states under pulsed excitation and propose next steps towards applications of this complex emission opening the doors to generation of complex non-classical states of light. Furthermore, we explain how the swing-up excitation technique could be improved by an optimized sample design, thus potentionally outperforming current excitation techniques employed in photonic quantum technologies.

Chapter 2

Fabrication and control of single quantum dots

Contents

In this chapter, we give an overview over the preparation of our sample that is used throughout this work and show how we control and use a single QD on it as a TLS. Since all aspects, such as all growth of self-assembled QDs in the Stranski-Krastanov mode, fabrication of diodes, excitonic transitions in QDs, and voltage-dependent emission of different charge states under non-resonant excitation have been studied in detail and are well-established in the community, in this chapter we only aim to give an overview over these topics. As a start, we summarize the molecular-beam-epitaxy (MBE) growth of self-assembled InGaAs QDs, which is the heart of the sample fabrication, including additional parts of the sample structure such as the distributed Bragg-reflector (DBR) and the back contact. We then give a description of the fabrication of the Schottky diode, which embeds the QD layer and show its IV-characteristics at room and liquid Helium temperature. Afterwards, we shortly explain the origin of quantized states in the QD and the excitonic transitions within them, and finally show their emission at 10 K under optical excitation in the wetting-layer. The measurements reveal different

charge states which are well separated for different applied gate voltages, including both emission from the neutral exciton X^0 and the negatively charged trion X^-.

2.1 Fabrication of samples with tunable and individually addressable quantum dots

Growth of self-assembled InGaAs quantum dots

The core structure of the sample studied in this work consists of a semiconductor crystal structure grown by MBE on a GaAs wafer. During MBE growth atomically thin layers of a material are deposited onto a substrate in ultra-high vacuum using molecular beams. The materials are usually semiconductors, pure or alloys, which are incorporated into several cells of the MBE machine. Changing the material during growth and carefully controlling parameters such as temperature and material deposition rates, thus allows for precise manipulation of material properties and the formation of complex sample structures with tailored characteristics [92, 93, 94, 95]. For our sample, this technique is utilized to create epitaxial layers on a 2inch GaAs wafer. As a start, a GaAs buffer layer of 300 nm is deposited onto the wafer to ensure a clean crystal surface for consecutive growth. After a pause for temperature adjustment, 18 layers of alternating AlAs with thickness of 80.9 nm and GaAs with thickness of 67.9 nm are grown. During this process, the wafer is slowly and continuously rotated to ensure an equal distribution of the material on the substrate in the radial direction. These 18 layer pairs form a DBR which later enhances the collection efficiency of the light emitted from the QD. The layer thicknesses of the individual layers correspond to one quarter of the wavelength of the expected QD resonance wavelength of 920 nm. Together with different reflective indices of $n_{GaAs} = 3.6$ and $n_{AlAs} = 2.97$ of the two materials [96, 97, 98], here given for a wavelength of 920 nm at room temperature, the layer configuration leads to destructive interference in transmission and constructive interference in reflection for a bandwidth of about 10 nm around the target wavelength [99, 100, 101]. Due to the rotation of the sample in the MBE chamber and a small asymmetry of the deposition of the material on the sample surface, the thickness of the layers is minimally higher in the center of the sample while decreasing towards the outer part, leading to a radial variation of the DBR center resonance. This later enables precise matching of QD density and DBR resonance by choosing a specific region of the sample for further fabrication. Afterwards, an intrinsic layer of GaAs of 50 nm and an n-doped Si-GaAs layer with thickness of 850 nm are deposited in the growth process. The doped layer serves as an electron reservoir which will become essential for charging of the QD,

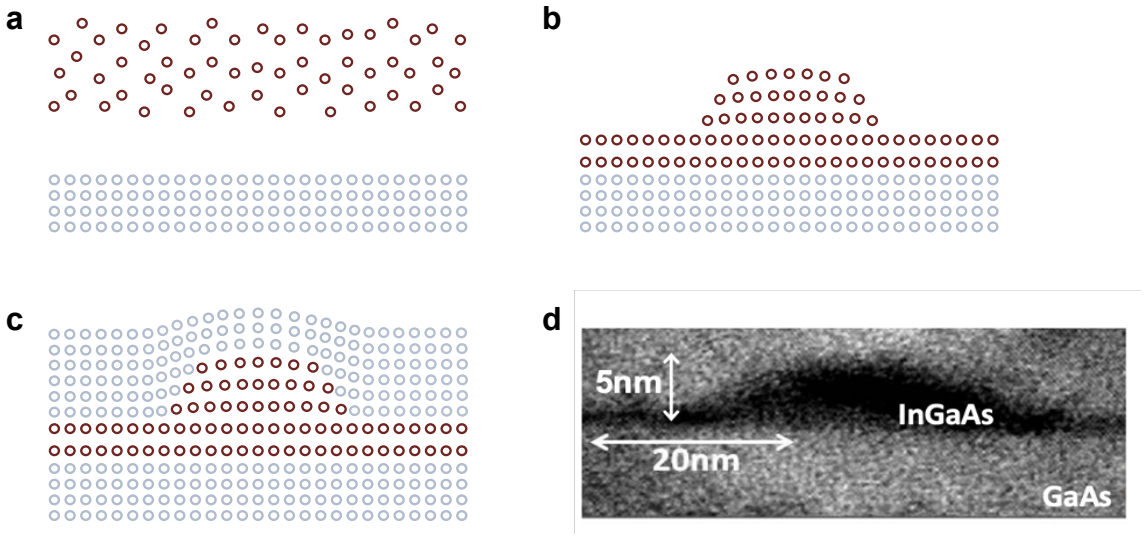

Figure 2.1 | Stranski-Krastanov growth of self-assembled QDs. **a-c**, Schematic of the layer-by-layer growth of QDs: InGaAs is deposited layer-by-layer on the host material GaAs during MBE growth. Due to the different lattice constants of both crystals, strain forms in the InGaAs layer which is released by formation of small islands, the so-called QDs. After this process, the QD layer is capped with the host material. **d**, Transmission-electron-microscopy image of a cross section through a single QD reveals its lens-shaped form and the wetting-layer. The image **d** is adapted from Ref. [102].

and as the basis for the back contact of the diode. The doped layer is followed by an intrinsic GaAs region of 350 nm in growth, before the several monolayers of InGaAs, the QD layer, are deposited onto the sample. This distance of the QD layer to the back contact is crucial for tunneling properties of charge carriers.

The QD layer is grown in the Stranski-Krastanow growth mode [103, 93], as sketched in Figure 2.1a-c. For the QD layer, individual InGaAs monolayers with a Ga 0.556 and In 0.444 composition are deposited onto the GaAs substrate (Figure 2.1a). As these layers have a larger lattice constant than the host material, strain begins to form with increasing crystal height. In a simplified picture, the strain is released via formation of small islands, the QDs, (Figure 2.1b) after a critical thickness of InGaAs is deposited onto the sample. The remaining thin layer of InGaAs underneath the QDs is referred to as the wetting-layer. After formation of the islands, the structure is capped with intrinsic GaAs, embedding the QDs completely in the host material (Figure 2.1c). Typically, the QDs are lens-shaped with a size in the region of 5 nm in height and 25 nm in diameter, as seen in the transmission-electron-microscopy image in Figure 2.1d for a representative InGaAs QD [102]. However, as they are formed spontaneously during growth, their shape and size varies slightly from QD to QD, giving them unique properties. During the QD growth, the rotation of the sample is paused, leading to a linear gradient in QD density across the wafer. Controlling the

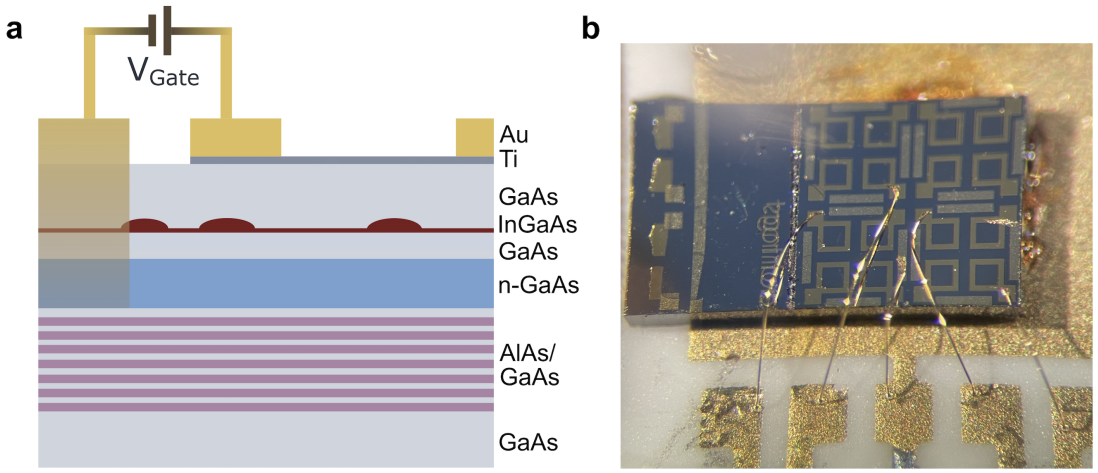

Figure 2.2 | Fabricated sample structure. **a**, Sketch of the sample structure in side view. From bottom to top the crucial elements are the DBR (grey), a n-doped region (blue) serving as the back contact, the QD layer (red), and all embedded in an intrinsic GaAs matrix (light grey). Fabricated on top are the front contact consisting of a Ti and Au layer, as well as the back contact, together forming the Schottky diode. **b**, Microscope image of the fabricated sample in top view. Front and back contacts as well as gold wire-bonded diodes are visible.

indium content and temperature of the sample during QD growth enables adjustment of the mean QD emission frequency. Deposition of another 140 nm of intrinsic GaAs concludes the sample structure grown via MBE. A sketch through the cross-section of the sample after further fabrication is shown in Figure 2.2a. Note that even though the sample growth did not include a top-DBR, a very weak cavity is formed between the DBR below the QD layer and the top layer of the sample due to the high difference in reflective index between sample and environment. Thus, the thickness of the intrinsic layer above the QDs is crucial. It was here optimized to match the cavity length to 1x the wavelength of the QD resonance in GaAs, and thus to place the QD layer near an antinode of the cavity mode. The cavity length in our design matches once the wavelength in the material. After the growth, the reflectivity of the DBR and the ensemble emission of the QDs is spatially mapped over the wafer at 10 K. For details please refer to Ref. [104]. The wafer is afterwards cleaved into 6 mmx7 mm pieces for further processing. A piece with a low enough QD density of $< 1\,\mu m^{-2}$ for optical access to individual QDs, and the DBR reflectivity and the weak cavity resonance matching the mean QD ensemble transition frequency is chosen.

Fabrication of Schottky diodes

To complete the sample, we fabricate the top and back contact of a Schottky diode in three optical lithography steps, embedding the QD layer into the intrinsic region of the diode. The diode structure not only enables charge control of the QD and fine tuning of resonances [105, 106, 107], but also stabilizes the charge environment [108, 109, 110], as will be discussed in the next subsection.

As a first step, the back contacts are fabricated. To this end, the sample is spin coated with photoresist AZ5214E. Following this, the sample is baked, exposed to short-wavelength light in a Mask Aligner SUSS MJB3 to define the back contacts in a specific pattern given by a mask, and then undergoes a reversal bake. Flood exposure and a following development of the resist using AZ400K ensure removal of the exposed parts of the mask and thus proper formation of structures. Oxygen plasma cleaning and stripping the oxide layer prepare the sample for evaporation. During the evaporation in a Leybold L560 physical vapor deposition system, a specific material sequence is deposited onto the masked sample with specific thicknesses: 13 nm of Ge, 30 nm of Au, 10 nm of Ni and finally 100 nm of Au. The first metal combination is necessary for the diffusion of the metal into the sample during a subsequent annealing step while the second part, a thick Au layer is crucial for successful wire-bonding of the contact to the chip carrier. A lift-off process after the evaporation using the solvents acetone or DMSO removes the mask and leaves the evaporated metals in the pre-defined pattern on the sample. In a final annealing step, the sample is heated up to $420°C$ to allow the metals to diffuse into the sample to the n-doped layer, forming an ohmic back contact [106, 111].

The front contacts are fabricated in two analogous steps without annealing, where in a first part 4.5 nm of Ti are evaporated onto the entire diode windows of the front contact, to allow for electrical contact, while in a second step 20 nm of Ti and 150 nm of Au are evaporated using a different front contact mask, which uncovers only the frame of the front contacts and the bond pads, necessary for wire-bonding. The back contacts (stripes in a lighter gold color) and the front contacts (gold squares darker diode windows inside, with additional bond pads, seen in a darker gold color) are shown in the photograph in Figure 2.2b from a top view. The thin layer of Ti inside the diode windows enables electrical access over the whole front contact, while simultaneously allowing for optical access from top to the QD layer inside the sample, with only minimal absorption on the sample surface. In addition, the size of the diode windows with only 300 µm × 300 µm allows for easy orientation on the sample surface and localization of single QDs in the cryostats for optical measurements. Finally, the sample is cleaved into four pieces and after characterization of the individual diodes

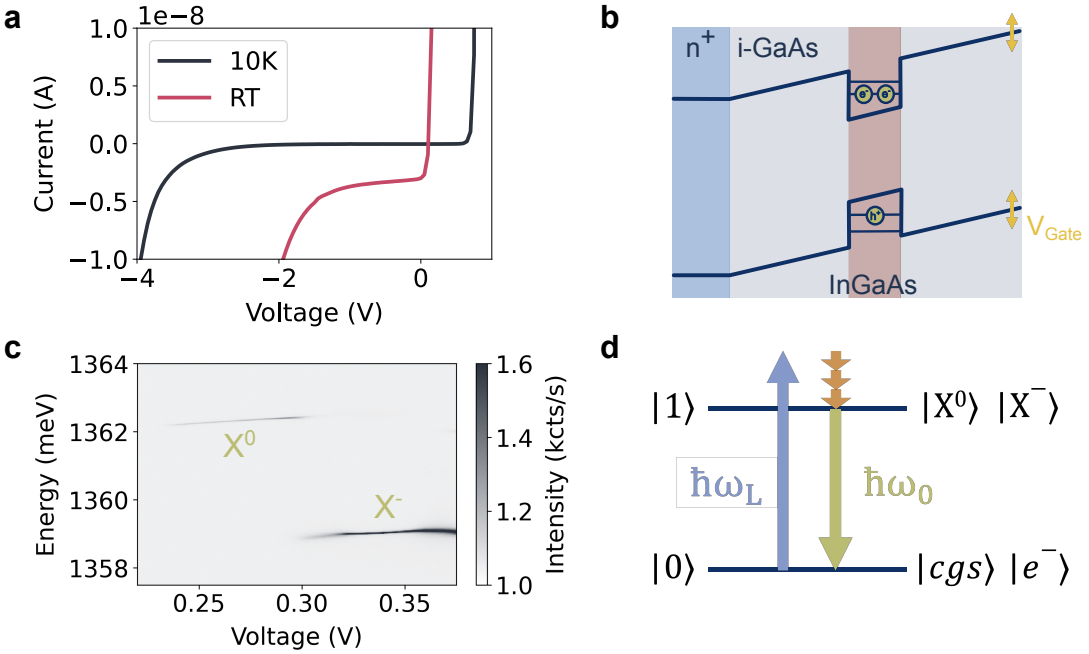

Figure 2.3 | Schottky diode and voltage-dependent QD emission characteristics. **a**, IV-curve of the Schottky diode at room temperature (red) and at 10 K (blue) shows typical diode behavior with the reverse bias and forward leakage region between the temperature-dependent reverse breakdown and forward conduction region. **b**, Schematic energy band structure through a cross-section of the sample reveals the build-in potential and the quantized levels of a single QD. **c**, Voltage-dependent emission of a single QD reveals charge-stable voltage-plateaus which we identify as emission from the neutral exciton X^0 and the negatively charged trion X^-. Both can be individually approximated as TLSs, as schematically shown in **d**.

and is glued onto a chip carrier. Four front contacts and one back contact are bonded with gold-wires to the contacts on the chip carrier as seen in Figure 2.2b. As ideally all the back contacts are electrically connected to the n-doped layer, bonding one back contact is sufficient for all diodes. A sketch of the cross section of the sample structure including MBE grown and fabricated components is presented in Figure 2.2a.

2.2 Electrical and optical characterization

Diode characteristics

To test and characterize the fabricated diode, we measure the voltage-dependent current at room temperature and at 10 K between front and back contact. The resulting curve for the diode used throughout this work is presented in Figure 2.3a in linear scaling. For both temperatures, the typical diode behavior is observed with increasing voltage: diode breakdown, where excessive reverse bias leads to a sharp rise in current,

potentially causing device failure, reverse bias at smaller negative voltages, where a small reverse current flows due to minority carrier injection, the leakage region where forward leakage current occurs due to thermionic emission over the Schottky barrier, and finally forward conduction, characterized by a sharp increase in current as the forward bias voltage overcomes the barrier. The reverse bias current is higher for the diode at room temperature compared to cryogenic temperature due to thermal generation of charge carriers and though room light. The diode was fully covered for the characterization at $10K$ while for the room temperature measurement some stray light was still present. In addition, the breakdown voltage in reverse is increased to about $-3.5\,\mathrm{V}$ at $10\,\mathrm{K}$ compared to $-1.5\,\mathrm{V}$ at room temperature, while the conduction with forward bias only starts around $V_C = 0.65\,\mathrm{V}$ for $10K$ instead of $V_C = SI0.05V$ for room temperature. This allows for a wider tunability of the band structure and charge state control of the QD without flow of charge carriers across the intrinsic region. The strong temperature-dependence in breakdown current and forward conductance originates from the current flow in both cases. For the breakdown current, at high temperatures, the thermal energy can promote the generation of electron-hole pairs within the semiconductor material, increasing the carrier concentration. This effect can lower the breakdown voltage of the diode, as more charge carriers become available to participate in the breakdown mechanism. While for the forward conduction in Schottky diodes, the current involves the movement of majority carriers across the metal-semiconductor junction. At higher temperatures, the thermal energy increases the velocity of these carriers, facilitating their movement across the barrier [112, 113, 114]. Taking the thickness of the intrinsic region d into account, the electric field at the QD layer can be estimated as [104]

$$F = (V_C - V_G)/d. \tag{2.1}$$

Here, V_G denotes the externally applied gate voltage to the diode. Through this electric field charge the state of the QD can be deterministically controlled and the resonance fine-tuned as will be explained in the following subsections.

Quantization of energy levels and excitonic complexes

For the trapping of individual charge carriers in single QDs the combination of the two different materials for the QDs and the host matrix is essential. GaAs, with a bandgap of $E_g = 1.5190\,\mathrm{eV}$ [115] and InGaAs with a lower bandgap of about $E_g = 0.9031\,\mathrm{eV}$ in bulk at liquid Helium temperature [116] form a type I band alignment and in this way create a trapping potential for charge carriers. The small size of the QDs (Figure 2.1d), in comparison to the de-Broglie wavelength of the free charge carriers in the material, quantizes the band structure within the QD and forms discrete energy

levels. These can be occupied by individual electrons and holes (Figure 2.3b). Due to the asymmetric size of the QDs, the confinement in z- or growth-direction and the radial directions x and y are different. The short height in z-direction leads to strong confinement, already shifting the second energy levels outside of the potential trap, leaving a potential well form in z-direction, where only the lowest quantized levels need to be taken into account. With larger extent of the QD in the radial directions, quantization leads to a harmonic, shell-like structure of the quantizes states. In analogy to the shells of the atom, they can be labelled s, p, etc. starting from the lowest energetic level, for both electrons and holes [117, 118]. As the charge carriers are fermions, they can occupy each individual level only twice, providing that their spin state is opposite, following Paulis exclusion principle [119]. Within this work, we focus on the radiative transitions involving electrons and holes from the lowest energetic levels, i.e. the s-shells. The electrons relevant for state occupation within the QD are in the conduction band and thus have a spin of $S_e = 1/2$ and projected angular momentum in growth direction of $S_{e,z} = \pm 1/2$. While for the holes in the valence band different types exist, for self-assembled InGaAs QDs in GaAs, only heavy holes with a total angular momentum of $F_{h,z} = \pm 3/2$ are relevant. Light holes and split-off holes are shifted to higher energies due to confinement, strain and spin-orbit coupling [113, 120, 121].

The recombination of one electron in the conduction band and one hole in the valence band is possible via emission of one photon, if the combined momenta of the charge carriers match the total angular momentum of the photon $M = \pm 1$. This is the case for antiparallel spins which can efficiently recombine radiatively. These excitonic complexes are called bright excitons. Dark exciton, on the other hand, with parallel spins and total angular momenta of $M = \pm 2$ couple less efficiently to light. Among others this leads to longer lifetimes and increased coherence [122, 123, 124, 125]. For the optical transitions, $M = \pm 1$ corresponds to right and left circular polarized light, respectively. The recombination can occur within different excitonic complexes. The most common bright excitonic structures for self-assembled InGaAs QDs in Schottky diodes are the neutral exciton X^0, the negatively charged trion X^- and the biexciton $2X$. They consist of an electron and a hole as an excited state and the crystal ground state as the ground state, of two electrons and one hole in the excited state and one electron in the ground state, and of two electrons and two holes in the excited state which recombine in a cascade via the neutral exciton to the crystal ground state, respectively. For the neutral exciton, the exchange interaction between electron and hole spins in their different configuration leads to a mixing of the states and a energetic splitting in the excited state, the so-called fine-structure splitting. It is strongly dependent on symmetry and strain inside the QD [126]. For details on spin states, excitonic

complexes and optical selection rules, please refer to Ref. [126, 117, 127, 119, 121] The diode provides the choice between exciting the neutral exciton or the negatively charged trion by controlling the ground state. Applying a positive voltage to the diode decreases the band tilting (see Figure 2.3b) and lowers the energies of the quantized states with respect to the n-doped layer. This increases the tunneling probability of charge carriers from the n-doped layer into the QD.

Voltage-dependent emission under blue-detuned excitation

In the experiment, the different charge states can be observed by looking at the photoluminescence from a single QD and varying the applied gate voltage to the diode. To this end, the sample is cooled down to 10 K in a flow-cryostat cooled by liquid Helium and a single QD is excited through an objective with light of 850 nm, while the emission is collected though the same objective and spectrally resolved in a spectrometer. Details on this so-called μPL setup can be found in the appendix. The cooling of the sample is necessary to circumvent decoherence and non-radiative decay paths induced by phonons in the material [75]. Excitation above resonance of the excitonic transitions allows for spectral filtering of the excitation and emission, and facilitates the characterization of voltage-dependent photoluminescence. Upon excitation, the generated charge carriers quickly thermalize to the lowest states inside the QD via emission of phonons before recombining radiatively from the discrete states of the QD (Figure 2.3d). This provides an insight into the QD resonances and excitonic complexes for different electric fields [105, 106]. The spectrally resolved emission for gate voltages from 0.22 V to 0.38 V are shown in Figure 2.3c from the single QD used for the measurement in this thesis. Two clear and well-separated charge plateaus can be distinguished which we identify as emission from the neutral exciton X^0 at higher energy and lower voltage, and emission from the negatively charged trion X^- at lower energy and higher voltages [127, 126, 121, 117]. In the limit of high voltage and therefore a more flat band structure, charge carriers start to flow through the Schottky diode, while for low voltages, the tilt of the bands is increased leading to tunneling of the charge carriers to the contacts before radiative recombination, resulting in no emission.

In addition, the resonance of the excitonic transitions can be fine-tuned within the charge plateaus via the quantum-confined Stark effect (QCSE) [128, 109, 107], as seen by the tilt of the charge plateaus with increasing voltage. Here, the energy of the transitions varies with applied voltage, as the dipole of the excitonic complexes interacts with the electric field induced by the sample design and the externally applied voltage. Thus by choosing the externally applied gate voltage we can choose the

TLS we want to work with in subsequent experiments (Figure 2.3d). For the main measurements in the next two chapters, we will focus on the negatively charged trion as the excited state and a single electron as a ground state within a single QD as a TLS. In comparison to the neutral exciton X^0 it does not have a fine-structure splitting at zero magnetic field and is thus the cleaner TLS [126, 129]. In Chapter 4, we will discuss second-order correlation measurements that prove that the use of the X^--e^- transition as a TLS is justified.

2.3 Summary

In summary, in this chapter we have described the growth of self-assembled InGaAs QDs inside a structure consisting of a DBR and an n-doped layer intended for the diode. Afterwards, optical lithography and fabrication of the diode contacts were described, resulting in our finished sample structure. We briefly explained the origin of discrete levels inside single QDs and optical transitions between different excitonic states. Following this, we looked at the voltage-dependent emission properties of a single QD, identifying the neutral exciton and negatively charged trion. We argued that the trion and electron states will be used as a TLS for subsequent measurements.

Chapter 3

The dynamical Mollow triplet

This chapter includes material from

Katarina Boos*, Sang Kyu Kim*, Thomas Bracht, Friedrich Sbresny, Jan M. Kaspari, Moritz Cygorek, Hubert Riedl, Frederik W. Bopp, William Rauhaus, Carolin Calcagno, Jonathan J. Finley, Doris E. Reiter, and Kai Müller,
Signatures of Dynamically Dressed States, Physical Review Letters **132**, 053602 (2024)
https://doi.org/10.1103/PhysRevLett.132.053602

Contents

In the preceding chapter, we explained the growth and fabrication process of our samples, enabling access to individual single QDs in a tunable diode-structure. Through optical excitation in the wetting-layer, we observed voltage-selective emission of two different quantum TLS, the negatively charged trion X^- and the neutral exciton X^0. We now continue to study the fundamental resonant light-matter interaction of a TLS, the X^--e^- transition in a single InGaAs QD, with a resonant light field. As a start, we describe the interplay between a resonant cw laser and the TLS which has been studied in detail both theoretically and experimentally [12, 17, 27, 28, 29, 30, 31].

Subsequently, we focus on the characteristics of a single quantum TLS coupling to a pulsed light field. The emission spectrum of the resulting dynamically dressed states has predominantly been explored theoretically [32, 33, 34, 35, 36, 37, 38]. After describing the origin of the different peaks in the emission spectrum, we present the first experimental observation of the complete resonance fluorescence emission spectrum of a single quantum TLS, also referred to as the dynamical Mollow triplet, excited by short Gaussian pulses [90]. Our findings validate theoretical predictions, revealing the emergence of multiple sidepeaks whose number and spectral detuning correlate with excitation pulse intensity, while their spectral characteristics are influenced by pulse length. Excitation power- and detuning-dependent measurements offer additional insights into the observed emission features and reveal strong similarities with the Mollow triplet under cw excitation. We additionally provide theoretical calculations, which are in very good agreement with our experimental results.

3.1 Two-level system- field interaction

Semiclassical approach

We start by describing the interaction between a TLS and a classical light field theoretically. Within the dipole approximation, we assume the wavelength of the field being much larger than the size of the TLS, i.e. the dipole [2]. This holds true for InGaAs QDs with a size of several nanometers, while the transition and thus excitation wavelength is approximately 920nm. We describe the laser field by $\mathbf{E}(t) = \epsilon E_0 \cos \omega t$, with angular frequency ω and ϵ being the unit polarization vector of the field. Moreover, we assume without restriction of generality propagation in z-direction, and linear polarization along the x-axis. The detuning of the laser field from TLS resonance is given by $\Delta = \omega - \omega_0$. The two states of the TLS are denoted by $|g\rangle$, the ground state, and $|e\rangle$, the excited state, and are split by the resonance frequency ω_0 [3, 130]. The state can be expressed by the wavefunction

$$|\psi\rangle = c_g |g\rangle + c_e |e\rangle \tag{3.1}$$

with the time-dependent probability amplitudes c_g and c_e. The Hamiltonian of the system is given by $H_{semi} = H_0 + H_{int}$, where $H_0 = \hbar\omega_0\sigma^\dagger\sigma$ is the unperturbed Hamiltonian of the TLS and $H_{int} = -\mathbf{d}\times\mathbf{E}$ represents the interaction with the field. Here, $\mathbf{d}$ denotes the dipole operator and $\sigma = |g\rangle\langle e|$ and $\sigma^\dagger = |e\rangle\langle g|$ the the raising and lowering operators of electronic excitations. $\sigma^\dagger\sigma = |e\rangle\langle e|$ represents the upper-state projection operator [131, 117]. The dipole operator of the TLS can be expressed in

terms of lowering and raising operators such that the system Hamiltonian is expressed as

$$H_{semi} = H_0 + H_{int} = \hbar\omega_0\sigma^\dagger\sigma - \langle g|\, d\, |e\rangle\, (\sigma + \sigma^\dagger). \tag{3.2}$$

By applying the rotating-wave approximation (RWA) we focus on slow dynamics and assume that $|\,\omega - \omega_0\,| << \omega + \omega_0$, neglecting fast oscillating terms, i.e. replacing them by their average value zero [131, 130]. This approximation is valid for interaction near resonance. The RWA simplifies our interaction Hamiltonian to

$$H_{int} = \frac{\hbar\Omega}{2}(\sigma e^{i\omega t} + \sigma^\dagger e^{-i\omega t}). \tag{3.3}$$

Ω denotes the generalized Rabi frequency which quantifies the strength of the TLS-field interaction [131, 132]. In case of resonant excitation where $\Delta = 0$, the generalized Rabi frequency simplifies to the resonant Rabi frequency given by

$$\Omega_R = -\frac{\langle g|\, d_x\, |e\rangle\, E_0}{\hbar} \tag{3.4}$$

in the semiclassical picture. Inserting the state $|\psi\rangle$ of our TLS and the Hamiltonian into the time-dependent Schrödinger equation

$$i\hbar\partial_t\, |\psi\rangle = H\, |\psi\rangle \tag{3.5}$$

gives us the differential equations for the probability amplitudes [131]

$$\partial_t c_g = -i\frac{\Omega}{2}c_e e^{i\omega t} \tag{3.6}$$

$$\partial_t c_e = -i\omega_0 c_e - i\frac{\Omega}{2}c_g e^{-i\omega t}. \tag{3.7}$$

For convenience, we now transform into the rotating frame of the laser, defined by the laser frequency ω. With the upper-state amplitude expressed as $\tilde{c}_e = c_e e^{i\omega t}$, the differential equations are now simplified to

$$\partial_t c_g = -i\frac{\Omega}{2}\tilde{c}_e \tag{3.8}$$

$$\partial_t \tilde{c}_e = i\Delta\tilde{c}_e - i\frac{\Omega}{2}c_g \tag{3.9}$$

and the system Hamiltonian becomes

$$\tilde{H}_{semi} = \tilde{H}_0 + \tilde{H}_{int} = -\hbar\Delta\, |e\rangle\, \langle e| + \frac{\hbar\Omega}{2}(\sigma + \sigma^\dagger). \tag{3.10}$$

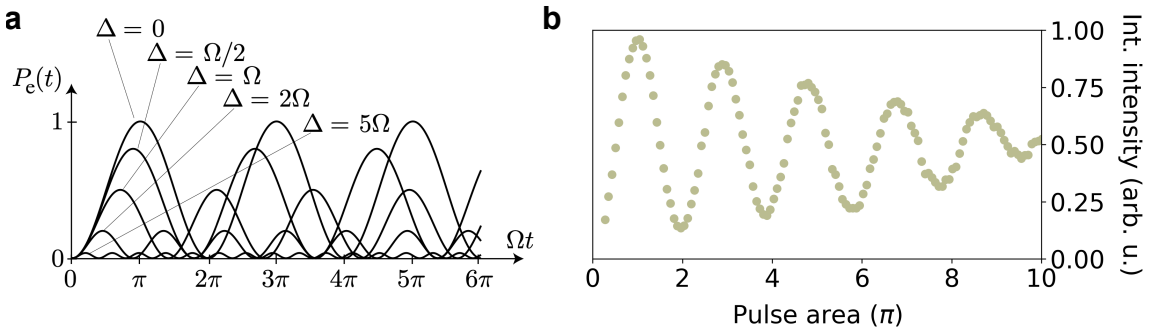

Figure 3.1 | Rabi oscillations. **a**, Calculated upper state population for different detuning Δ of the light field with respect to TLS, dependent on Ωt. With increasing Δ, the frequency of the Rabi oscillation increases, while the amplitude decreases. The TLS is initially in the ground state. **b**, Integrated intensity of the X^- emission as a function of excitation pulse area in the experiment. Rabi rotations up to 10 π are resolved, with damped amplitude for higher pulse area due to dephasing. Graph **a** is adapted from Ref. [131].

Note that in the rotating frame, the excited state is lowered by $\hbar\omega$, leaving it separated only by the detuning $\hbar\Delta$ from the ground state [131].

Rabi oscillations

Solving the coupled differential equations for the amplitudes for arbitrary detuning Δ from resonance [131] gives the time-dependent amplitude probabilities as

$$c_g(t) = e^{i\Delta t/2}\left[c_g(0)\left(\frac{1}{2}\Omega\right) - \frac{i}{\Omega}[\Delta c_g(0) + \Omega_R \tilde{c}_e(0)]\sin\left(\frac{1}{2}\Omega t\right)\right] \tag{3.11}$$

$$\tilde{c}_e(t) = e^{i\Delta t/2}\left[\tilde{c}_e(0)\left(\frac{1}{2}\Omega\right) + \frac{i}{\Omega}[\Delta c_g(0) - \Omega_R c_g(0)]\sin\left(\frac{1}{2}\Omega t\right)\right]. \tag{3.12}$$

Thus optical resonant or near-resonant excitation of a TLS results in oscillation of the dipole moment and oscillation of the population between the two states of the TLS [3]. The oscillation strength and amplitude is given by the generalized Rabi frequency Ω. It varies in frequency with detuning Δ, while decreasing in amplitude with larger Δ as shown in Figure 3.1a [131]. For a TLS initially in the ground state, the population probability of the excited state can thus be expressed as

$$P_e(t) = \frac{\Omega_R^2}{\Omega^2}\left(\frac{1}{1} - \frac{1}{2}\cos\Omega t\right). \tag{3.13}$$

For resonant excitation $\omega = \omega_0$, the excited state population probability reduces to

$$P_e(t) = \mid \tilde{c}_e(t) \mid^2 = \frac{1}{2}(1 - \cos\Omega_R t), \tag{3.14}$$

thus the population oscillated between ground state and excited state with the resonant Rabi frequency Ω_R, reaching both states with unity probability in theory. This is commonly exploited for controlled excitation of TLSs, where a pulse with an area of $\int dt\Omega(t) = \pi$ drives the system from ground state to excited state or vice versa with near-unity fidelity [133, 131, 40, 41]. Increasing the area of resonant excitation pulses while recording the emission intensity reveals Rabi rotations, i.e. emission intensity oscillations dependent on the excitation pulse area.

To experimentally investigate the resonant light-matter interaction, we utilized the negatively charged trion X^- of a single InGaAs QD as a quantum TLS as described in Chapter 2. The sample was cooled down in a custom-made dip stick to the liquid Helium temperature of 4.2K. An optical head on the stick was optimized for cross-polarized filtering [17], to enable efficient filtering of the residual excitation light from the QD emission. For the excitation, a tunable cw Ti:Sapph cavity laser was used, where the pulses were customized to the length of 8 ps. The emission was spectrally resolved and recorded by a spectrometer. A detailed description of the resonance fluorescence setup and picosecond pulse generation can be found in the appendix.

A measurement showing Rabi rotations is presented in Figure 3.1b. Here, the emission of the resonantly excited X^--e^- transition was recorded while the pulse area was varied by increasing the intensity of the excitation pulse, and the pulse length was kept at 8 ps. The damping of the oscillation with increasing pulse area originates from dephasing, mainly due to acoustic phonons [75, 31].

Quantization of the electromagnetic field

A different approach to the TLS-field interaction problem is to treat both TLS and light field quantum-mechanically. To this end, we need to describe the laser field in a fully quantized picture. We start by considering the quantization of a single field mode. The Hamiltonian can be derived to [133, 131]

$$H_L = \frac{p^2}{2m} + \frac{1}{2}m\omega^2 q^2, \tag{3.15}$$

where the coordinate operators are given by

$$q = \sqrt{\frac{\hbar}{2m\omega}}(a + a^\dagger) \tag{3.16}$$

$$p = \sqrt{\frac{m\hbar\omega}{2}}\left(\frac{a - a^\dagger}{i}\right) \tag{3.17}$$

with the photonic creation and annihilation operator $a^\dagger$ and a [131, 130]. Taken together, the Hamiltonian of the light field can be expressed as

$$H_L = \hbar\omega \left(a^\dagger a + \frac{1}{2}\right). \tag{3.18}$$

The description is formally analogous to the harmonic oscillator [133, 131]. The eigenstates of the system are given by $|n\rangle$ where $n = 0, 1, 2, ...$ represents the number of photons in the specific state and the state vector is given by $|\psi\rangle = \Sigma_n c_n |n\rangle$ [131, 130]. The creation and annihilation operators satisfy the equations

$$a|n\rangle = \sqrt{n}\,|n-1\rangle \tag{3.19}$$

$$a^\dagger|n\rangle = \sqrt{n+1}\,|n+1\rangle \tag{3.20}$$

and can be combined to the number operator $N = a^\dagger a$ [133]. In this context, the concept of a photon can be distinguished in terms of a quantum of a single mode of the electromagnetic field, i.e. the operators a and a^+ create or annihilate a photon, or as radiation with the energy of $\hbar\Omega$ [130]. Taken into account that the kinetic and potential energy are always positive, the system must satisfy $0 \leq E < \hbar\omega$. This gives rise to a zero-point energy of $E_0 = 1/2\hbar\omega$ from which the n^{th}-level energy can be derived by repeated application of the creation operator on the corresponding states to [133]

$$E_n = E_0 + n\hbar\omega = \hbar\omega\left(n + \frac{1}{2}\right). \tag{3.21}$$

The system Hamiltonian of coupled TLS and quantized light field in the interaction picture can now be described as

$$H_{quant} = H_0 + H_{int} = \hbar\omega_0 |e\rangle\langle e| + \hbar g(\sigma a^\dagger e^{i\omega t} + \sigma^\dagger a e^{-i\omega t}) \tag{3.22}$$

where $2g$ is the one-photon Rabi frequency [131]. Moving out of the interaction frame into the Schrödinger picture, similar to transforming into the rotating frame in the semiclassical model, results in

$$H_{quant} = \hbar\omega_0\sigma^\dagger\sigma + \hbar g(\sigma a^\dagger + \sigma^\dagger a) + \hbar\omega\left(a^\dagger a + \frac{1}{2}\right) \tag{3.23}$$

$$= H_0 + H_{int} + H_L \tag{3.24}$$

which corresponds to the Jaynes-Cummings-Hamiltonian [131]. Here states of the form $|g, n+1\rangle \rightarrow |e, n\rangle$, split by $-\hbar\Delta$, are coupled. The interaction and coupling strength

is again described by the generalized Rabi frequency, which has now the form

$$\Omega_n = \sqrt{2(n+1)g^2 + \Delta^2}. \tag{3.25}$$

In the limit of large photon number n for a coherent field, corresponding to the classical case, the photonic operator a equals to $a = \sqrt{n}$. Further recognizing $\Omega/2 = g\sqrt{n}$, the quantized model corresponds to the semiclassical description [131].

Dressed states

In the semiclassical picture, the interaction between the TLS and the classical light field, i.e. the Rabi oscillations, give rise to new eigenstates

$$|+\rangle = \sin\theta\,|g\rangle + \cos\theta\,|e\rangle \tag{3.26}$$

$$|-\rangle = \cos\theta\,|g\rangle - \sin\theta\,|e\rangle \tag{3.27}$$

where the Stueckelberg angle θ is defined as $\tan 2\theta_n = -\frac{\Omega_R}{\Delta}$ for $(0 \leq \theta_n \leq \pi/2)$ [131]. The corresponding eigenvalues are given by

$$E_\pm = -\frac{\hbar\Delta}{2} \pm \frac{\hbar\Omega}{2}. \tag{3.28}$$

These new dressed states are split by the Rabi frequency $\Omega = \sqrt{\Omega_R^2 + \Delta^2}$.

In the fully quantized picture, the interaction between the TLS and the quantized light field gives rise to the following new eigenstates

$$|+, n\rangle = \sin\theta_n\,|g, n+1\rangle + \cos\theta_n\,|e, n\rangle \tag{3.29}$$

$$|-, n\rangle = \cos\theta_n\,|g, n+1\rangle - \sin\theta_n\,|e, n\rangle \tag{3.30}$$

where $\tan 2\theta_n = -\frac{2g\sqrt{n+1}}{\Delta}$ for $(0 \leq \theta_n \leq \pi/2)$. The eigenstates now additionally depend on the photon number n [131]. The corresponding eigenvalues at resonance are given by

$$E_\pm = (n+1) \pm g\sqrt{n+1} \tag{3.31}$$

Here, the dressed states are split by the generalized Rabi frequency $\Omega_n = \sqrt{2(n+1)g^2 + \Delta^2}$ and exists in a ladder system with in-/decreasing photon number n. Note that the splitting between the states depends on n, thus it is not equal between adjacent dressed state doublets, which is especially significant for small photon numbers [131].

In the classical limit where $n >> 1$, the difference in splitting between neighboring doublets becomes negligible, and the system can be described by the semiclassical

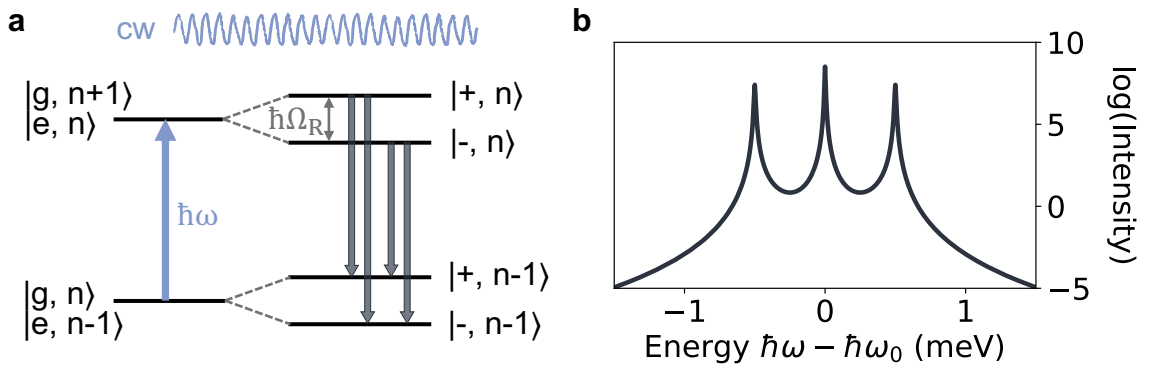

Figure 3.2 | Dressed states under cw excitation. **a**, The coupling of a resonant cw laser results in new eigenstates, the dressed states, which are split by $\omega_0 \pm$ the driving strength Ω_R of the excitation. As the intensity of the cw laser is constant, the splitting is continuous in time. **b**, The 4 possible radiative transitions within the dressed states give rise to the Mollow triplet in emission.

model, i.e. splitting of states by $\Omega = \sqrt{\Omega_R^2 + \Delta^2}$. The dressed states are schematically depicted in Figure 3.2a.

The Mollow triplet

Between the new eigenstates, four transitions with three distinct frequencies are possible, which give rise to the Mollow triplet when time-integrating the emission of the system [12, 3, 130]. A simulated spectrum of the Mollow triplet under resonant cw excitation is depicted in Figure 3.2b in logarithmic scaling. Note that the simulations in this chapter were performed by Bracht *et al.*, as explained in Section 3.2..

The integrated area of the center peak of the Mollow triplet is twice as large as the area of each of the sidepeaks, as two transitions contribute to it, while the splitting of the sidepeaks from the center depends on the generalized Rabi frequency Ω of the field. Another way to interpret the Mollow triplet in emission of a TLS interacting with a resonant cw field is to look at the original carrier frequency ω which is modulated in amplitude. This modulation occurs naturally due to Rabi oscillations within the TLS and it generates sidebands split by the modulation frequency [131, 134]. Having established the origin of the emission spectrum originating from the interaction between a TLS and a coherent resonant or near-resonant light field with constant intensity in time, we now look at the characteristics of the Mollow triplet with changing parameters in the experiment.

To experimentally investigate the TLS-field interaction, we excite the trion-electron transition in our QD resonantly with a resonant laser, while separating emitted signal from residual laser in the cross-polarized resonance fluorescence setup and recording the signal with a spectrometer, as described in the appendix.

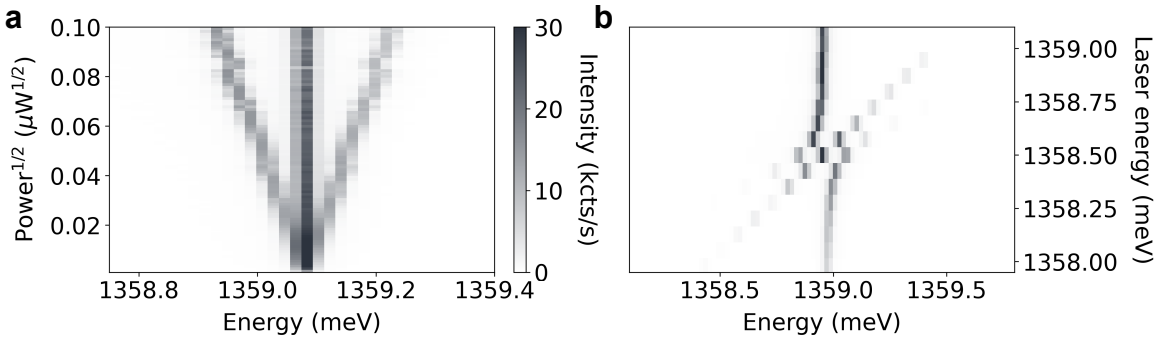

Figure 3.3 | Power- and detuning-dependent characteristics of the Mollow triplet. **a**, With increasing Rabi frequency Ω_R of the excitation, the splitting of the sidepeaks with respect to the center increases. **b**, Detuning the excitation laser from resonance leads to an additional splitting as well as an asymmetry in the Mollow triplet.

For increasing field intensity, the spectra are shown in Figure 3.3a, where TLS and field are in resonance. Consistent with theory, we see the Mollow triplet sidepeaks shift linearly towards the outside with increasing Rabi frequency $\Omega_R \sim$ excitation power$^{1/2}$. Furthermore, we look at the detuning-dependent spectra where the field frequency is tuned across resonance while keeping the intensity constant (Figure 3.3b). As expected from generalized Rabi energy $\Omega = \sqrt{\Omega_R^2 + \Delta^2}$, the detuning induces an additional splitting of the sidepeaks. The whole triplet is centered at the laser frequency and decreases in intensity for increasing $\mid \Delta \mid$. Our experimental results are in good agreement with earlier theoretical and experimental work [12, 17, 27, 28, 31, 29, 30].

3.2 Dressed states under pulsed excitation

A retrospective on the dynamical Mollow

After having described the dressed states and the resulting Mollow triplet, originating from the interaction of the TLS with a resonant coherent light field with constant intensity in time, we now move on to investigate the dynamics and emission characteristics of our TLS when interacting with a resonant and near-resonant pulsed light field. We assume pulse durations which are short with respect to the radiative lifetime of the excited state, that is, pulse durations in the picosecond range, as are typically employed for control, excitation and spin rotation in QD systems [39, 40, 41, 31, 44, 77]. Remarkably, even though pulsed excitation is common in a variety of quantum optical and technological applications for quantum systems, especially QDs [39, 40, 41, 31, 44, 77], the fundamental interaction of a single TLS with the pulsed light field and the subsequent emission characteristics have been studied in detail only theoretically. Initially predicted for atoms in the 80s and subsequently studied in multiple work [32, 33, 34, 35, 36],

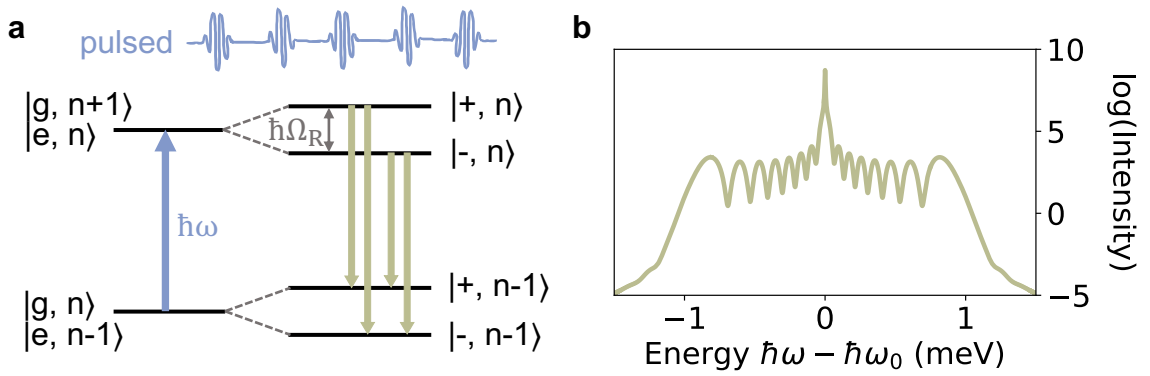

Figure 3.4 | Dressed states under dynamical dressing. **a**, Resonant excitation with short pulses gives rise to Rabi oscillations and dressing of the TLS states only at the presence of the pulse. **b**, Due to the additional modulation in time, the integrated emission spectra exhibits a multipeaked structure.

similar emission spectra are to be expected from QDs as described by Moelbjerg *et al.* [37]; emission under resonant pulsed excitation of a TLS is predicted to manifest itself in a broad complex emission spectrum containing multiple sidepeaks, whose number, detuning and form depends on excitation pulse parameters such as intensity or pulse length. In the experiment, demonstration of the full emission characteristics has been solely achieved in ensembles of TLSs represented by microplasma [135, 136] or QD-cavity systems where the cavity strongly alters the emission spectrum [137]. Before demonstration the first observation of the full emission characteristics of a TLS excited by short resonant pulses, we start by looking at the origin of the resulting multipeaked spectrum.

Origin of the multipeaked emission spectrum

For simplicity, we assume both light field and TLS in resonance, $\hbar\omega_L = \hbar\omega_0$. For a fixed point in time the new eigenstates originating from the interaction of the TLS and the light field are split by the Rabi energy of the laser $\hbar\Omega_R$ as depicted in Figure 3.4b . However in contrast to excitation, the intensity of the excitation and thus the splitting of the dressed states is not constant in time (Figure 3.4a), i.e. it is present only for a short period of time within the excited-state lifetime. During the presence of the pulse, Rabi oscillations are driven between the ground and excited state, with the frequency depending on the Rabi energy of the excitation and the number of oscillations depending on the pulse area. This thus leads to an oscillation of the emission probability during the interaction, with highest change of emission at uneven multiple of π in absorbed pulse area. For a time-integrated emission spectrum, as is the case for emission recorded by a spectrometer, the emitted parts at different times

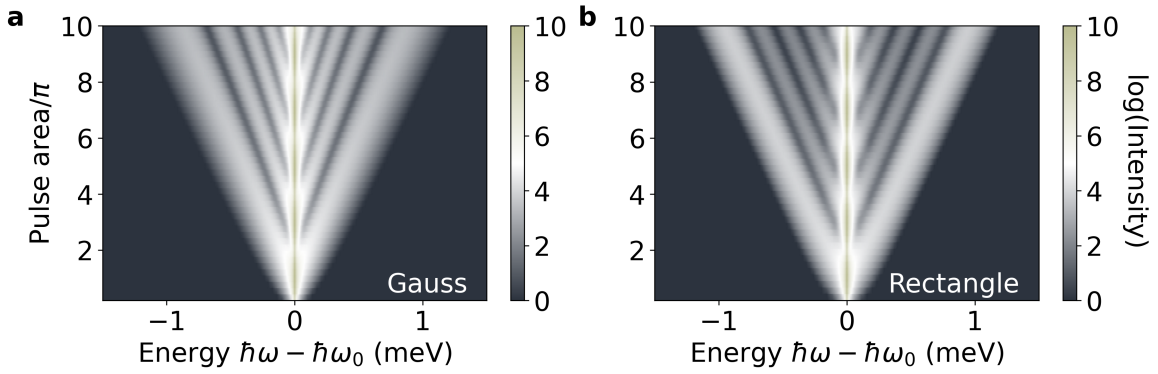

Figure 3.5 | Simulated emission spectra of the power-dependent dynamical Mollow triplet for different pulse shapes. **a**, Resonant excitation with a Gaussian pulse and **b**, resonant excitation with a rectangular pulse both result in similar emission characteristics: With increasing pulse area the main emission line at $\hbar\omega_0$ undergoes Rabi rotations, while multiple sidepeaks periodically appear and shift linearly away from the center. Note that the absolute maximal intensity of both pulses was chosen to be the same, thus the splitting of the sidepeaks is identical.

interfere, resulting in a spectrum containing multiple sidepeaks [37, 33] besides the main trion transition line at zero detuning, as shown in the simulated spectrum in Figure 3.4b.

The theoretical emission spectra were calculated by our collaborators Thomas Bracht, Jan Kaspari and Doris Reiter from the Technical University Dortmund and Moritz Cygorek from Heriot-Watt University, Edinburgh. For details, refer to Ref. [90] and [138, 139, 140, 37].

An alternative approach to understanding the origin of the sidepeaks is to see the intensity variation given by the short pulse as an additional modulation of the classical Mollow triplet emission spectrum under cw excitation [36]. The sidepeak spectrum varies in several aspects to the Mollow triplet. The sidepeaks themselves are lower in intensity with respect to the main emission peak by half an order of magnitude, and their number depends on the pulse area, i.e. it corresponds to the number of Rabi oscillations induced by the pulse [32]. The FWHM of the peaks decreases from the outside inwards. The splitting of the outermost sidepeaks corresponds to the maximal absolute intensity of the pulse [33, 37]. Taken no phonon interaction into account, the sidepeak spectrum is symmetric with respect to energy.

Generating additional sidepeaks with Rabi oscillations

A simulated spectrum of the dynamical Mollow triplet is presented in Figure 3.5a as a function of driving strength. A main emission line at the resonance of the trion dominates the spectrum, which undergoes Rabi rotations, visible as oscillations in

intensity with increasing pulse area. Consistent with literature [37], we see emergence of multiple peaks from the center. With increasing pulse area the sidepeaks on both sides shift linearly towards larger detuning, while with each additional 2π in pulse area, two new peaks emerge from the center, with decreasing FWHM peak-by-peak. Notably, the intensity of the sidepeaks is constant with increasing pulse area, i.e. independent of the Rabi rotations and the final state occupation after the QD-pulse interaction. This strongly indicates that the multiple peaks of the dynamical Mollow are emitted during the presence of the pulse and is consistent with the dressing of the states persisting only during the short presence of the pulse. In contrast to other pulse parameters, which will be discussed in the following subsections, the pulse form itself only has a minor impact on the formation of the sidepeaks and their characteristics as theoretically explored in previous work [33, 35, 36, 141]. In Figure 3.5a and b, we compare simulated power-dependent emission spectra of a TLS excited by finite Gaussian pulses and rectangular pulses, respectively. The pulse duration, defined by the FWHM with respect to the intensity, with values of 13.3 ps and 20.73 ps varied significantly between the two different pulses, while the maximal absolute intensity is kept the same. The main characteristics of the emission spectrum are in agreement for both pulse forms, the number, shift, intensity and form of the dynamical Mollow sidepeaks. For the performed measurements in the subsequent study, we chose short Gaussian pulses for the excitation of our TLS.

Experimental demonstration of the dynamical Mollow

For the experimental measurements, the negatively charged trion-electron transition of our QD was used as a TLS. Cooled down to 4.2K in the resonance fluorescence setup, the QD was excited by a pulsed Ti:Sapph laser, while the emission was detected with a spectrometer. The 150 fs pulses of the excitation laser were customized with a folded 4f pulseshaper [142] to be able to generate Gaussian-shaped pulses with variable duration and energy. For a detailed description of the resonance fluorescence setup and the generation of customized pulses, we refer the reader to the appendix. For an enhanced signal-to-noise ratio in the spectra, especially to account for laser leakage through the filtering process, in each measurement we averaged between 5 spectra and subtracted 5 averaged spectra where the QD was tuned out of resonance. Thus, electrical noise and oscillation in the laser suppression can lead to some negative values in the spectra. Therefore, an overall offset of 10 counts was added to the experimental data, to be able to reasonably plot the results with logarithmic scaling without neglecting datapoints.

Figure 3.6 shows the full experimental emission spectrum under pulsed excitation for increasing pulse area of 0π to 15π (left 2D plot), with its simulated counterpart in the

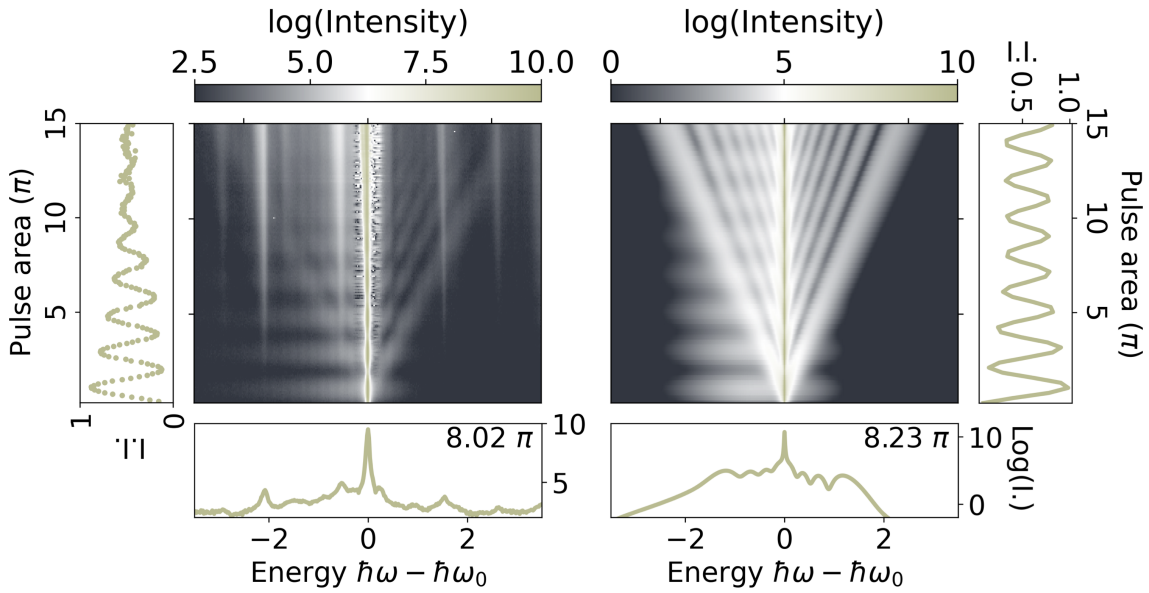

Figure 3.6 | Experimental pulse area-dependent emission spectra under excitation with 8 ps-long Gaussian pulses alongside theoretical spectra. The intensity is plotted in a logarithmic scaling. For both experiment (left) and theory (right), with increasing pulse area of the excitation, the main emission line of the QD resonance undergoes Rabi rotations, as explicitly shown by the integrated main peak as a function of pulse area, on the outside boxes. In addition, sidepeaks emerge from the center with each additional π in excitation pulse area and shift linearly towards the outsides. A cross-section of the emission spectra is plotted in the boxes below at a pulse area of around 8 π. Moreover, the phonon sideband is visible in broad horizontal lines, following the Rabi rotations.

right colorplot, both with logarithmic scaling in emission intensity. The pulse duration is kept constant at 8 ps. In agreement to the simulated data, at zero detuning the main QD emission line in the experimental spectra undergoes Rabi rotations with increasing pulse area, as is highlighted in the boxes left and right of the colorplots by the integrated intensity of the main peak as a function of the excitation pulse area. Rotations up to 15 π are visible, while decoherence and interaction with phonons lead to a damping of the rotations for large pulse areas, and noise of the suppressed resonant laser overlays the emission at zero detuning. In addition, renormalisation of the rotation frequency with pulse area in the experiment leads to a faster oscillation than the scaling on the y-axis, which is normalized to 1 π pulse area. This originates in the non-linear scaling of the phonon-interaction with pulse area [143, 75]. In the experiment, the center peak exhibits a red-shift of a couple µeV for large pulse intensities which we attribute to local heating of the material by the increasing power of the laser. As the spectral pulse width with 228 µeV, for a length of 8 ps in time, is large with respect to this shift and therefore does not tune the QD out of resonance, we do not account for the shift in the experiment or the analyzed data. In addition to the main emission line at the trion

resonance, the experimental data features sidepeaks emerging from the center on both sides, shifting linearly towards larger detuning. They are in very good agreement with sidepeaks in the corresponding simulation regarding width, origin and spectral shift of the peaks. A cross section of the pulse-area dependent spectra around 8 π is given below the colormaps. Overall, the sidepeak spectrum in the experiment is lower in intensity, as will be discussed in the following section in detail. Moreover, the experimental data exhibits the well-known phonon sideband emission [144, 145, 146], visible as broad horizontal lines, which follows the Rabi rotations with varying pulse area. It is well represented in the simulated data in Figure 3.6, as here exciton-phonon-interaction was taken into account [90]. The vertical lines in the experimental spectra originate from charge states from other QDs in the vicinity which are driven non-resonantly at high excitation intensities.

3.3 Shaping the dynamical Mollow spectrum in the experiment

Changing the spectral width

We continue to study the impact of the pulse length on the emission spectrum of the dynamical Mollow both experimentally and in the simulations. In Figure 3.7a to e, we decrease the pulse length of the resonant excitation from 12 ps to 4 ps. The pulse duration has a strong impact on the shape and width of the multipeaked spectrum. In contrast, the number of sidepeaks per given pulse area and a linear shift towards larger detuning hold true for all pulse durations. For decreasing pulse length, the slope of the outermost sidepeaks continuously increases from approximately 0.13 meV per pulse area in π to 0.39 meV per π in the experiment, and from 0.11 meV per π to 0.33 meV per π in the simulated data, while the inner sidepeaks have a stepwise higher increase. The sidepeak slopes for the three outermost sidepeaks are presented in Figure 3.8a in dependence of the pulse length. Experimental data and datapoints extracted from simulations are depicted as dots and lines, respectively. To approximate the slope of the sidepeaks, a linear fit was made in five maxima along the sidepeak at higher energy, for the three outermost peaks. We attribute the offset between experiment and datapoints from the simulations to the renormalization of the Rabi rotation with increasing excitation intensity in the experiment, which is not accounted for in the y-axis scaling, as described above. In the limit of long pulses, i.e. transitioning to cw excitation, the outermost emission peaks become the Mollow triplet sidepeaks [37]. The strong increase of sidepeak detuning per given pulse area with decreasing pulse

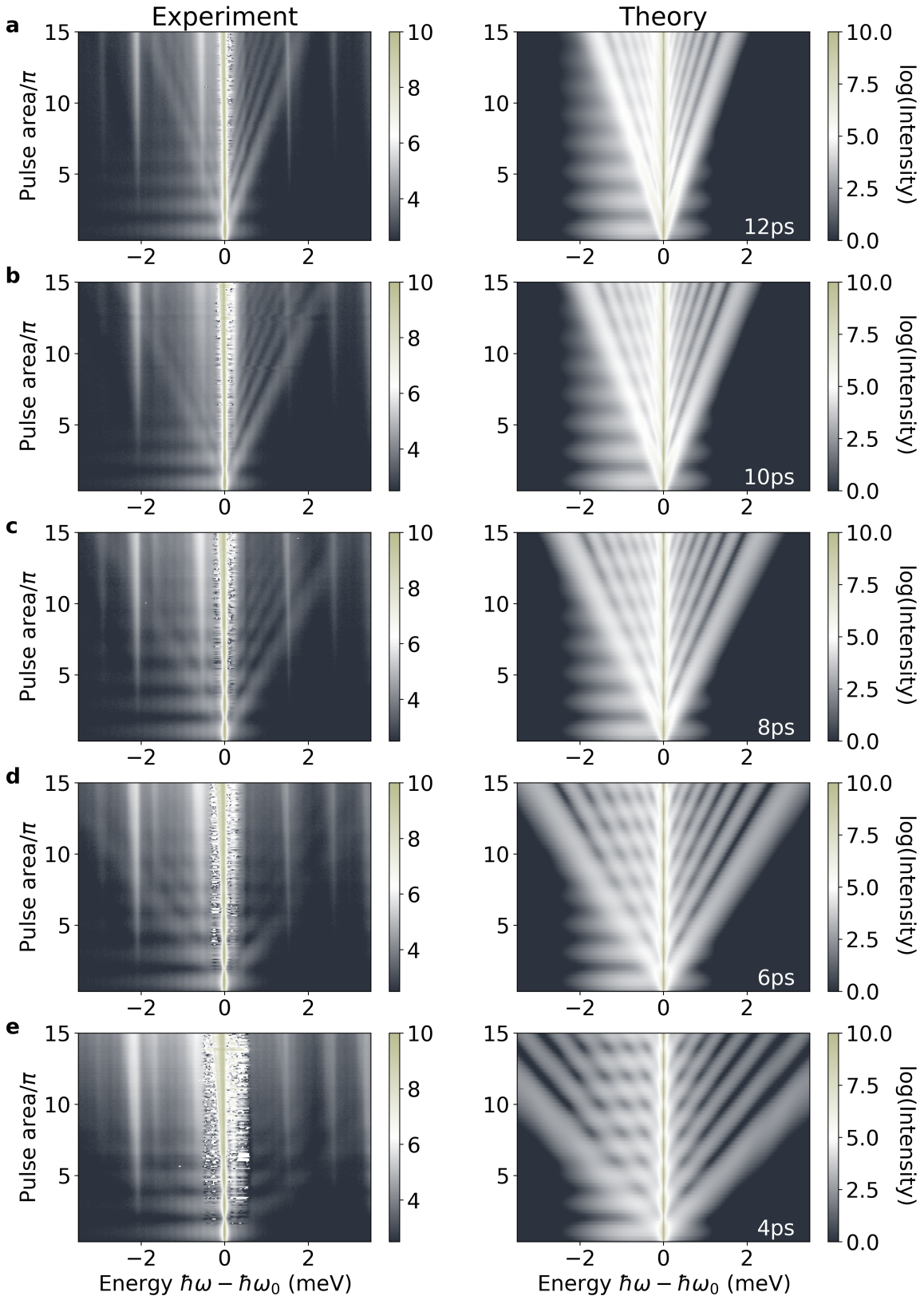

Figure 3.7 | Measured and simulated power-dependent emission spectra for varying pulse length. **a-e**, Similar characteristics can be observed for decreasing pulse length from $12\,\mathrm{ps}$ (**a**) to $4\,\mathrm{ps}$ (**e**), while the splitting of the sidepeaks per normalized pulse area increases strongly. Simultaneously, lower intensity and broader FWHM of the sidepeaks decrease the signal-to-noise ratio in the experiment.

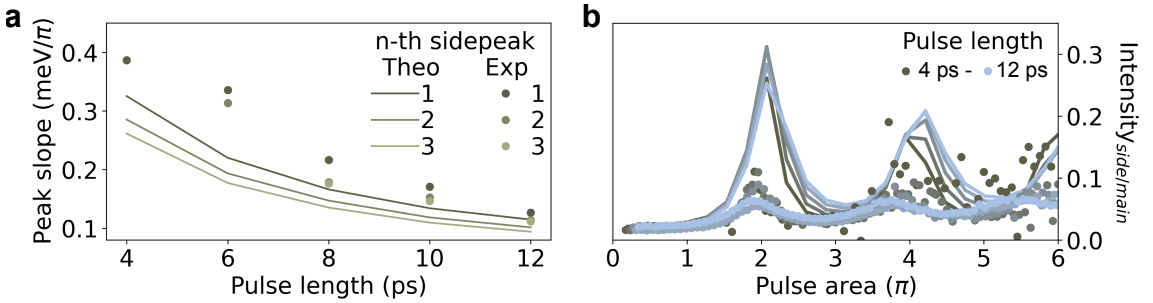

Figure 3.8 | Qualitative analysis of the sidepeaks for varying excitation pulse length. **a**, Approximated slopes for both experiment and theory. Both show a clear decrease with increasing pulse area, while the overestimation of the slope for shorter pulses originates from the renormalisation of the Rabi rotations and the resulting misfit of the y-axis scaling for larger pulse area. **b**, Estimated normalized amount of emission into the sidepeaks per pulse area for both experiment and theory.

length can be attributed to the higher maximal pulse intensity, thus stronger dressing of the states during the pulse, which determines the maximal splitting of the dynamical Mollow sidepeaks [33]. In addition, for shorter pulses which have a higher maximal intensity and broader energetic spectrum, the FWHM of the sidepeaks in the emission spectrum increases as well. As the sidepeaks are overall low in intensity, the larger FWHM contributes to the sidepeaks being harder to see in the experimental data. Figure 3.8b shows the estimated ratio of sidepeak emission to emission into the center peak for experiment (dots) and theory (lines) in dependence of the normalized pulse area. It becomes evident that emission into the sidepeaks does not follow the Rabi rotation and is thus non-negligible for even multiple of π in pulse area. Note that the dressed part of the spectrum exhibits a peak at the trion resonance as well, which overlaps with the sharper QD emission after interaction with the pulse. This center peak of the dynamical Mollow was not taken into account in the approximated emission ratio in Figure 3.8b resulting in a small underestimation of the sidepeak intensity in both experiment and theory.

Spectrally separating dressed and non-dressed emission

Moving forward, we now investigate the effect of finite detuning of the pulse on the dynamical Mollow emission spectrum. Here, the excitation pulse of 12 ps is scanned across the trion resonance from -0.7 meV to 0.7 meV, while the pulse intensity is kept constant at a value corresponding to pulse areas of 3 and 11 π at resonance. The resulting emission spectra are presented in Figure 3.9a and b, respectively, both for experiment and for simulation. The emission spectra can be divided into two parts. The first represents the bright independent emission at the trion resonance energy

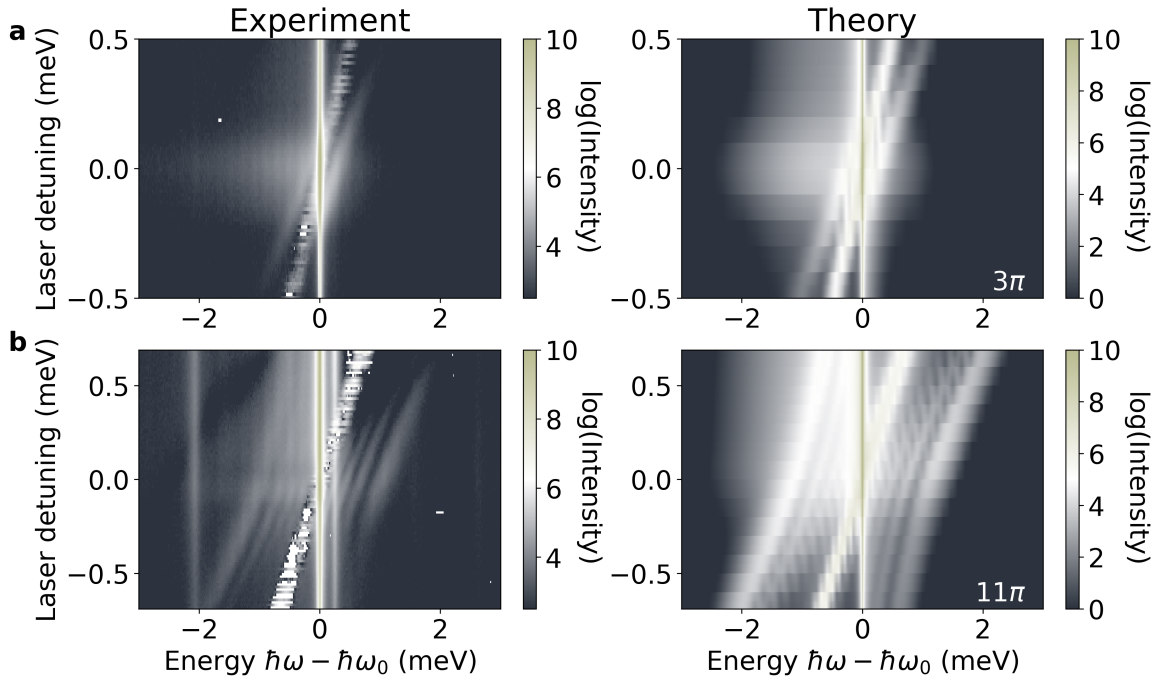

Figure 3.9 | Experimental and theoretical emission spectra under pulsed excitation with varying detuning. **a**, The 12 ps excitation pulse is scanned across resonance while keeping the pulse area fixed, corresponding to 3π at resonant excitation and **b**, corresponding to 11π. The spectra consist of a dominant emission at the QD resonance, and the dressed part including the sidepeaks. In analogy to the detuning-dependent Mollow triplet under cw excitation, the dressed part of the emission is positioned at and follows the energy of the laser, while with increasing absolute detuning the splitting of the sidepeaks increases. The number of sidepeaks is determined by the resonant pulse area of the excitation.

which remains unaffected by the detuning of the laser pulse. It has a narrower spectral FWHM in comparison to the pulse, which represents the lifetime via the Fourier-transform when neglecting additional line-broadening mechanisms. The second part of the emission consists of the spectrally broad emission of the dressed states, which includes the sidepeaks of the dynamical Mollow and a similarly broad center peak. The center position of this dressed part of the spectrum follows the laser energy when detuning from resonance. The center peak of the dressed part is only clearly visible in the simulated spectra, while in the experiment it is indicated but hard to observe as it overlays with noise of the suppressed laser. The number of sidepeaks is given by the pulse area at resonance, with 3 and 11 π in Figure 3.9a and b, respectively, and remains the same when detuning the light field. The splitting of the sidepeaks, however, with respect to the center of the dressed part of the emission, increases with increasing absolute detuning. The positioning of the dressed emission with the laser energy and the increasing splitting of all the sidepeaks with finite detuning is in agreement with the detuning-dependent Mollow triplet under cw excitation [17, 27, 28]. Here,

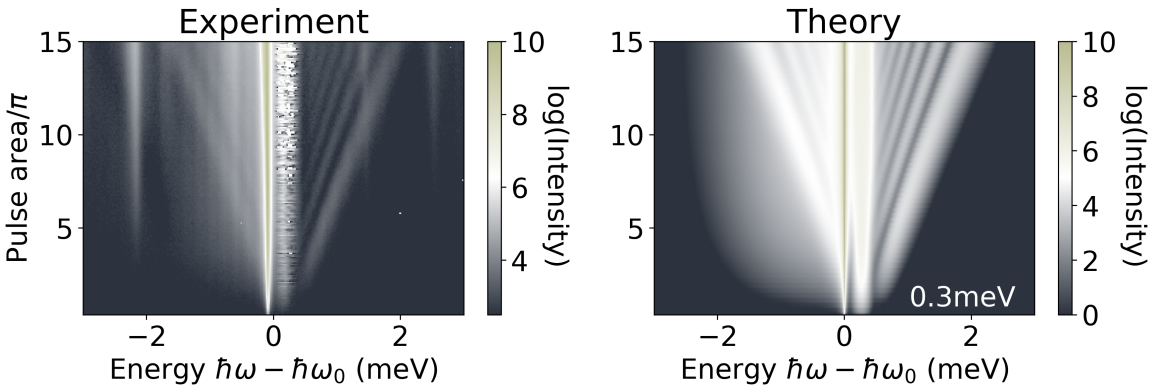

Figure 3.10 | Power-dependent emission spectra for excitation with a fixed blue-detuning of 0.3 meV and 12 ps pulse length. With increasing pulse area the splitting of the sidepeaks centered at the excitation energy increases while the separated emission peak at the QD resonance dominates the spectrum.

taking detuning into account, the new eigenstates originating from coupling of the TLS to the light field are described by the generalized Rabi frequency $\Omega = \sqrt{\Delta^2 + \Omega_R^2}$, which incorporates the resonant Rabi frequency Ω_R as well as a detuning Δ. This is valid only for small detuning with respect to the transition frequency $\hbar\omega_0$. As the generalized Rabi energy now determines the splitting of the states, their separation increases with increasing Δ. Furthermore, consistent with the Mollow triplet, the overall intensity decreases with increasing absolute detuning.
The clear separation of the dressed part of the emission and the main emission line at the trion resonance with detuning, and their differing spectral widths indicate different timescales of the emission and further confirm that the dressed part of the spectrum is emitted during the presence of the pulse. This is consistent with very recent time-resolved measurements of the first two sidepeaks of a dynamical Mollow spectrum by Liu *et al.* [147] which clearly show emission of the sidepeaks on shorter timescales compared to the excited-state lifetime of the main peak. The phonon sideband is here visible as an area with low emission intensity at the lower energy side of the QD resonance and zero laser detuning. Our simulated spectra are in very good agreement with the experimental data, showing both a clear separation of the independent emission line at the trion resonance, as well as the full dressed emission spectrum changing with varying excitation detuning. Remarkably, the detuning of the sidepeaks from the center for a given laser energy is very consistent with its experimental counterpart.

To empirically reinforce these statements, we investigate power-dependent emission spectra for blue-detuned excitation pulses relative to the QD resonance, as shown in Figure 3.10, both in experiment and in simulation. The pulse area is increased from 0 to 15 π, while the pulse length is kept constant at 12 ps and the detuning from

resonance is fixed at 0.3 meV. Similar characteristics to the resonant power-dependent emission spectra (Figure 3.7) can be observed, only that now the dressed part of the emission, centered at the laser energy, and the emission line at the trion resonance are separated by 0.3 meV. With increasing pulse area the splitting of the sidepeaks increases while new ones emerge from the dynamical Mollow center peak with a periodicity of 2π. However, now the sidepeaks are not directly connected to the center peak, even though they originate from it. Since the laser suppression works better for lower laser intensities in the resonance fluorescence setup, the center peak of the dressed emission is now visible in the experimental spectra at low pulse areas.

3.4 Summary

In summary, in this chapter we described the origin of dressed states with respect to light-matter coupling and the properties of the resulting well-studied Mollow triplet both in theory and experiment. Afterwards, we moved on to dressed states under pulsed excitation, i.e. a TLS driven by finite Gaussian pulses, where we explain the origin of the emission peaks and experimentally confirm the long-predicted multi-peaked resonance fluorescence spectrum [37, 33, 32, 90]. Investigating the properties of the spectrum dependent on the excitation pulse parameters, we confirm that the number of the emerging sidepeaks corresponds to the number of Rabi oscillations driven by a given pulse area, and show a strong dependence of the spectral width of the emission on the peak pulse intensity. Energetic detuning of the excitation pulse to the TLS results in spectral separation of the dressed emission and main TLS emission line, whereby the dressed part of the spectrum behaves analogous to the Mollow triplet under finite detuning. The presented theoretical simulations by Bracht *et al.* are in very good agreement with our experimental findings [90].

Chapter 4

Swing-up excitation

This chapter includes material from

Katarina Boos*, Friedrich Sbresny*, Sang Kyu Kim*, Malte Kremser, Hubert Riedl, Frederik W. Bopp, William Rauhaus, Bianca Scaparra, Klaus Jöns, Jonathan J. Finley, Kai Müller, and Lukas Hanschke,
Coherent Swing-Up Excitation for Semiconductor Quantum Dots, Advanced Quantum Technologies 2300359 (2024)
https://doi.org/10.1002/qute.202300359

Contents

Having studied the dressed states under cw and pulsed excitation in detail, we take a look at how the dynamical Mollow can be applicable in efficient and coherent excitation of TLSs. In this context, we experimentally investigate the recently proposed and in a proof-of-principle experiment demonstrated swing-up excitation mechanism [89, 148] in detail, with the trion-electron transition of a single InGaAs QD as the TLS. Currently it is under investigation as one of the most promising excitation techniques for quantum-

technological and quantum-optical applications [89, 148, 149, 150, 91, 151, 152, 153]. The scheme allows for spectral filtering due to detuning of the excitation pulses from the targeted resonance, while being coherent and efficient inherently. After giving a short overview oder the state-of-the-art excitation mechanisms for QDs, we explain the concept behind the swing-up excitation technique theoretically and from an intuitive physics-point of view. We then move on to the experimental observation of population inversion by the swing-up scheme where we extend the work by Karli *et al.* [148] and demonstrate coherence by resolving resonance lines with changing excitation intensity or detuning. Next, we look in detail at the influence of the excitation parameters on the feasibility and performance of the scheme and compare our experimental results with simulations. Observing strong background emission at high excitation intensities in the experiment, we find a compromise between high inversion efficiency and minimal background luminescence. Finally, we investigate the single-photon purity and indistinguishability of the photons emitted from the trion transition under swing-up excitation compared to the single-photon quality under resonant excitation [91].

4.1 The swing-up excitation scheme

Swing-up in the world of excitation methods

For quantum technological applications such as optical measurement-based quantum computing [154, 155, 156, 157, 158], key distribution for quantum communication [159, 160] or quantum repeaters [161, 162, 163], the on-demand generation of single photons with high quality is crucial. The performance of single-photon sources generating such photons is characterized by several key metrics [44, 164, 165]:

The **generation rate** refers to the frequency at which single photons are produced, indicating the source's productivity. This rate is typically engineered and optimized through photonic structures like resonators via the Purcell enhancement, in combination with an increased repetition rate of the excitation. **Efficiency**, or brightness, measures how effectively a single-photon source produces usable photons, considering losses and other inefficiencies. Beyond quantum efficiency, factors such as collection efficiency, which can be enhanced by resonators, detection efficiency, and the efficiency of the excitation contribute to this metric. The **single-photon purity**, given as $p_1 = P_1 / \sum_{n>0} P_n$ with P_n denoting the probability to have n photons in a pulse, describes the likelihood that the source emits exactly one photon at a time. This is essential for many quantum applications and can be approximated experimentally by measuring the second-order coherence function for good single-photon sources. **Indistinguishability** describes the ability to exhibit two-photon interference [166]. In particular, it quantifies

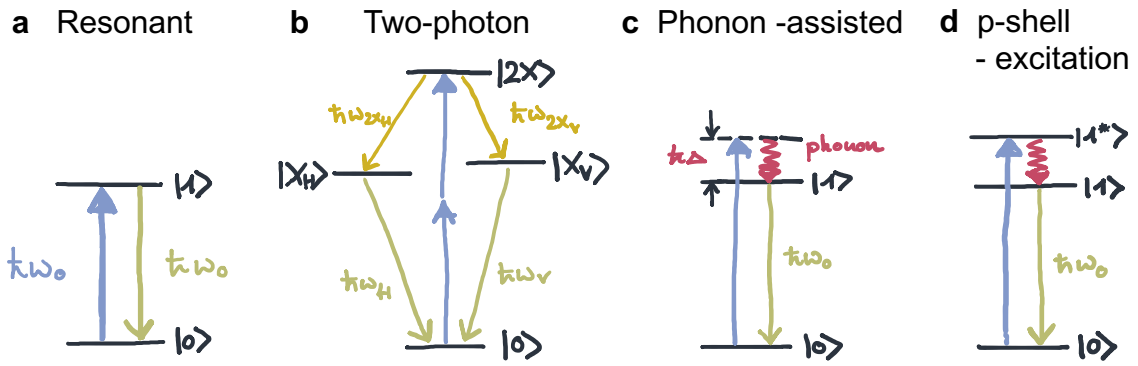

Figure 4.1 | State-of-the-art excitation methods for QDs. **a**, For resonant excitation, the excitation and emission have the same energy and are commonly separated via cross-polarized filtering. **b**, Excitation via the two-photon cascade relies on the two-photon excitation of the biexciton from the crystal ground state. Radiative decay occurs through the intermediate, fine-structure-split neutral exciton states. **c**, For phonon-assisted excitation, the excitation is blue-detuned with respect to the resonance and non-radiative decay to the lowest excited state of the QD follows within picoseconds of the excitation pulse by emission of a phonon. **d**, When exciting the TLS via the p-shell, the excitation is resonant with an excited state of one of the charge carriers. The system decays to the s-shell before recombining radiatively.

how identical the emitted photons are in terms of properties such as wavelength, polarization, mode and temporal profile. This is essential for ensuring coherent interactions between photons in quantum networks.

While these properties strongly depend on the emitters and sample structures themselves, for highly optimized quantum emitters and single-photon sources such as QDs [80, 81, 78, 44, 65, 79], especially the brightness, single-photon purity and indistinguishability is significantly influenced by the excitation method. Furthermore, several applications require coherence and flexibility in polarization for the excitation process [167, 86, 61, 168, 169], and precise filtering of the excitation laser from the emission to ensure minimal background.

In recent years, various excitation techniques have been realized and optimized for QDs with regard to applications in quantum technologies, with individual advantages and disadvantages: In resonant excitation, as schematically depicted in Figure 4.1a, the TLS is excited with a pulsed or cw laser having the same frequency. This resonant driving enables coherent excitation and control of the TLS while keeping the laser intensities minimal, in particular for TLSs embedded in cavities. The absence of relaxation methods prior to photon emission ensures a high degree of indistinguishability of the emitted photons. However, the separation of the emitted signal from the residual excitation light is non-trivial. Besides spatial filtering, where excitation and emission modes are orthogonal [16], the commonly employed filtering

method is cross-polarized filtering [17, 55, 56], as discussed in Chapter 3 and in the appendix. In this filtering technique the polarization of the detected photons is always fixed [17, 67, 16] with respect to the polarization of the excitation laser, thus, commonly a large part of the emitted photons is omitted. While for the study of fundamental light-matter interaction such as coherent driving and dressed states this can often be neglected, for many applications relying on the polarization-degree of freedom this becomes problematic. Such applications involve generation spin-photon and photon-photon entanglement in polarization, as well as the generation of more complex photonic graph states. Another commonly employed excitation method for QDs is the two-photon excitation of the biexciton [64, 65, 66], as sketched in Figure 4.1b. Here, the ground state-biexciton transition is resonantly excited with two photons. Decay takes place via the finestructure-split neutral exciton levels. The excitation resonance is energetically centered between the biexciton-exciton and exciton-ground state transitions, enabling spectral filtering. This coherent excitation is an excellent method for generating high-purity single photons when combined with spectral filtering, as re-excitation is suppressed [66, 65]. Additionally, a high degree of indistinguishability can be guaranteed when including a stimulation pulse that drives the biexciton-exciton transition, eliminating the timing-jitter [170, 70]. This excitation method is however not suitable for any applications involving arbitrary level configurations, such as the negatively or positively charged trion in a magnetic field, commonly used as a spin qubit. Other excitation techniques for QDs include phonon-assisted excitation [57, 58, 59] and excitation via the p-shell [60, 171] as shown in Figure 4.1c and d. For both, the excitation is blue-detuned from the QD resonance and relaxation via phonons to the lowest excited state occurs, before the charge carriers recombine radiatively. For phonon-assisted excitation, a virtual level is excited while for p-shell excitation, one charge carrier is excited to an excited state. The spectral detuning of the excitation to the QD resonance enables spectral filtering. This ensures high brightness and a freedom in choice of polarization both for excitation and detection separately. These features make the excitation method convenient for generation of complex entangled states [169, 171]. Yet, a lack of coherence and efficiency in both excitation techniques become problematic when scaling up. Furthermore, the relaxation via phonons induces an additional timing-jitter and delay, which should best be avoided [68, 69].

In this context, Bracht *et al.* [89] recently proposed a new optical excitation method which promises to overcome all above named challenges. They showed that two far red-detuned pulses with a specific detuning, intensity, pulse duration and time delay can excite a TLS coherently with near-unity efficiency. This allows not only for spectral filtering and high brightness, but enables excitation and detection of superpositions of states via polarization, and is applicable to any TLS without inherent limitations [89].

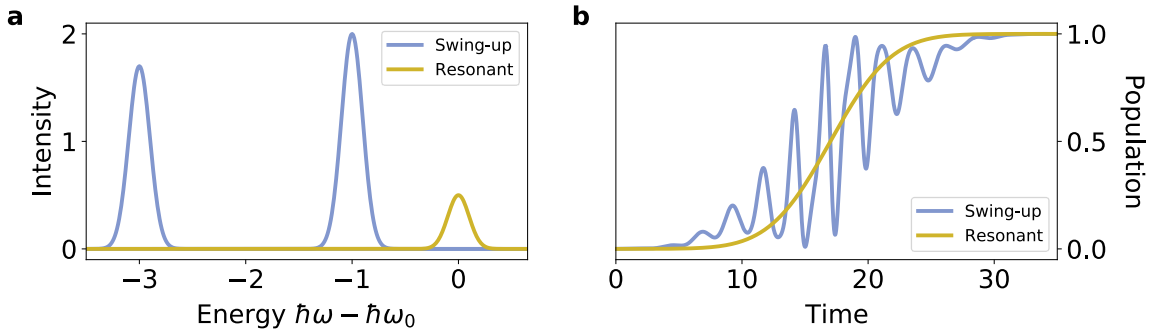

Figure 4.2 | Schematic illustration of the swing-up excitation technique. **a**, Representation of the energetic detuning of the two swing-up pulses (blue) with respect to resonance and resonant excitation (yellow), and their relative intensity. **b**, Simulated time-resolved population inversion during the presence of the pulse for swing-up (blue) and resonant (yellow) excitation. While for resonant excitation the population is driven smoothly from lower to upper state, during the swing-up excitation the population oscillates into the excited state.

Furthermore, the excitation method is promising for excellent properties of the emitted single photons.

The swing-up concept and theoretical description

We now start by explaining the swing-up excitation technique itself in detail. For theoretical description, we consider a general TLS with transition frequency ω_0. The laser field interacting with out TLS consists of two independent red-detuned pulses and is expressed by $\hbar\omega_i = \hbar\omega_0 + \hbar\Delta_i$ where $i = 1{,}2$. The pulse configuration is schematically shown in Figure 4.2a in blue, in comparison to a resonant π-pulse excitation shown in yellow. For the following analysis we define the less detuned swing-up pulse as pulse 1 or the first pulse and the far detuned pulse of the swing-up excitation as pulse 2 or the second pulse. The swing-up excitation can be described by the system Hamiltonian

$$H = -\hbar\Delta_1\sigma^\dagger\sigma + \frac{1}{2}\hbar(\Omega^*(t)\sigma + \Omega(t)\sigma^\dagger) \tag{4.1}$$

with the excitation field

$$\Omega(t) = \Omega_1(t) + \Omega_2(t+\tau)e^{-i(\omega_2-\omega_1)t}. \tag{4.2}$$

Here, the RWA was already taken into account and the system is in the rotating frame of pulse 1. The pulses have Gaussian envelopes $\Omega_i(t)$, and integrated pulse areas of $\alpha_i = \int_{-\infty}^{+\infty}\Omega_i(t)\,dt$. The time delay between the two pulses is given by the duration τ. The phase difference between the two pulses was not accounted for as it can be

neglected [89]. We now calculate the upper-state population as $\langle 1|\,\rho(t_f)\,|1\rangle$ with the von Neumann equation

$$\frac{\partial}{\partial t}\rho(t) = -\frac{i}{\hbar}[H, \rho(t)] \tag{4.3}$$

with the density matrix ρ [91, 89]. While the density matrix is used to describe the statistical state of a quantum system, including both pure and mixed states, we use it here solely to describe the pure state of our TLS $|\psi\rangle$, where $\rho = |\psi\rangle\langle\psi|$. For follow-up on and an extension of our work this formalism allows for an easy integration of decoherence and dephasing processes which were not taken into account here.
Figure 4.2b shows population inversion of the TLS, initially in the ground state, by a resonant π-pulse (yellow) and via swing-up excitation (blue). In contrast to resonant excitation where the population is smoothly driven from ground to excited state during interaction of the TLS with the swing-up pulses, the population oscillates between ground and excited state while being inverted, ending up with near unity fidelity in the excited state for a specific combination of the excitation pulse-parameters.
This process can intuitively understood in two different ways. On the one hand, the two red-detuned pulses give rise to faster Rabi oscillations with reduces amplitude, characteristic to their Rabi frequency, while the combination of the two different frequencies, i.e. a beating, oscillates the population from initial to the opposite state [89]. The other way is to look at it in the dressed-state picture [149]. Here, the pulse 1 can be interpreted as being used to dress states of the TLS as explained in Chapter 3, while the second pulse drives transitions between those dressed states.

4.2 Experimental demonstration and exploration of the excitation parameter space

While the swing-up scheme is applicable to any TLS, in the subsequent experiments we use the trion-electron transition in a single QD embedded in a Schottky diode structure as the TLS, as described in Chapter 2. The sample is cooled down to liquid Helium temperature in the resonance fluorescence setup which is in detail explained in the appendix. To be able to fully cover the parameter space of the excitation pulses, we split and send the 150 fs pulse of the Ti:Sapph laser into two separate folded 4f pulseshapers (details can be found in the appendix) where the output of one pulseshaper is sent over a variable delayline. Both pulse paths include optical attenuators each and are afterwards merged into a single-mode polarization-maintaining fiber which is sent to the resonance fluorescence setup. This way, the intensity, energy and duration of each pulse can be adjusted separately, and the pulses can be delayed with respect to each other with sub-picosecond precision. The emission of the QD is spectrally

filtered and recorded with a spectrometer and a CCD camera for spectral analysis, or detected with single-photon avalanche diodes (SPADs) and analyzed using a quTAG timing correlator for time-resolved correlations.

Experimental demonstration of the swing-up scheme

The complexity of the excitation parameter space with 7 degrees of freedom poses a challenge for investigating the swing-up technique in detail. As a start, we aim to find resonances of high inversion efficiency and study the impact of individual excitation parameters and demonstrate coherence of the scheme in the experiment. To this end, we record the emission intensity of the trion-exciton transition and calculate the upper state population after interaction of the pulses with the TLS in the experiment and simulations, respectively. The emission intensity in the experiment is normalized to the emission intensity of the trion-electron transition under resonant excitation with a pulse area of 1π. We plot the results in two-dimensional colorgraphs, where we keep the pulse length, pulse separation in time, the intensity and the detuning of the first pulse constant, and vary the pulse area and the detuning of the second pulse. Such a dataset is shown in Figure 4.3a for fixed parameters of 10 ps pulse length for both pulses, zero time delay, $\hbar\Delta_1 = -0.7\,\mathrm{meV}$ and $\alpha_1 = 8\pi$. Experiment and simulation are shown in the left and right panels, respectively. The intensity of the first pulse is normalized to the pulse area of a resonant pulse with 1π, while the pulse area of the second pulse is normalized to the pulse area of the first pulse. This allows for describing resonances and efficiency of the swing-up scheme independently of setup and sample specifications. In Figure 4.3a, the pulse area of the second pulse is varied from $\alpha_2/\alpha_1 = 0.44$ to 1.81, while the detuning is scanned from $\hbar\Delta_2 = -3\,\mathrm{meV}$ to $-0.92\,\mathrm{meV}$. The colorscale represents the emission intensity with respect to resonant excitation in the experiment and the normalized excited state population in the simulated spectra. The experimental and simulated spectra both clearly show one dominant resonance line at around $\hbar\Delta_2 = -2\,\mathrm{meV}$ slightly shifting towards larger detuning with higher intensity. The resonance clearly confirms successful population inversion of the TLS via the swing-up excitation technique in the experiment. Several further resonances at lower detuning are visible which are weaker in intensity. The appearance of those resonances and the position with respect to the excitation parameters is in very good agreement between experiment and simulation. The resonance lines, i.e. oscillation of the intensity with varying detuning and with varying excitation intensity, similar to Rabi oscillations under resonant excitation, are consistent with the proposed coherence of the scheme as previously discussed. Looking at the efficiency of swing-up excitation for this parameters set, we observe a maximal efficiency of 0.66 in the experiment,

at $\alpha_2/\alpha_1 = 1.1$ and $\hbar\Delta_2 = -2.05\,\mathrm{meV}$ which is lower than the population inversion fidelity of 0.97 in the simulation for similar excitation pulse parameters. This would already outperform cross-polarized resonant excitation where the extraction efficiency is limited to 0.5 via cross-polarized filtering for the case of absent polarizers in the experimental setup. However, the maximal achieved efficiency in the experiment varies significantly from the near-unity fidelity as proposed by the simulations for this parameter set. We attribute this reduction in efficiency to noise and decoherence induced by the high laser intensities that are necessary for the scheme. In particular, loss of charge carriers by interaction of the laser light field with defects and free electrons, and uncertainties such as deviation in pulse shape, power fluctuations and birefringence are expected to contribute to the process. Operating at 8π and 8.8π for the two laser pulses results in absolute power in the µW regime, while for resonant excitation, pulse intensities in the low nW regime are typical.

Impact of the pulse intensity

To study the impact of the pulse intensity, we increase the pulse area of pulse 1 from $\alpha_1 = 8\pi$ to 11π, while keeping the pulse duration fixed at 10 ps. In analogy to before, the detuning of the first pulse remains at $\hbar\Delta_1 = -0.7\,\mathrm{meV}$ while both pulses fully overlap in time. Detuning and intensity of pulse 2 are varied to investigate resonances and the point of highest efficiency. The results are shown in Figure 4.3b. Similar characteristics as for lower pulse 1 intensity can be seen, exhibiting several resonance lines in both experiment and theory. For the higher pulse area of 11π, the resonance line pattern is more complex, showing a larger dependence on the intensity of the second pulse, while still overall one dominant emission line and multiple weaker resonance lines at lower detuning can be distinguished. In comparison to emission spectra at lower first pulse intensity, a slight mismatch between experimental and simulated resonances can be observed. In the simulation the resonance lines are shifted towards higher detuning, in particular for higher pulse intensities of the second laser pulse. This shift originates most likely from a mismatch in measured excitation power to the actual light intensity in the sample at the vicinity of the QD, as the weak cavity formed by the DBR and the top layer of the sample induces a non-linear wavelength-dependent coupling of the excitation pulses into the cavity. As the pulse intensities of the swing-up pulses are normalized to the resonant pulse area of 1π, in particular for high intensities and detuning a small deviation is to be expected. For the given parameters of the first laser pulse, we find a maximal swing-up efficiency of 0.68 at $\alpha_2/\alpha_1 = 0.93$ and $\hbar\Delta_2 = -2.08\,\mathrm{meV}$ in the experiment and in the simulation a value that is so close to unity that is rounds to 1.00 if three or fewer decimal places are taken into consideration.

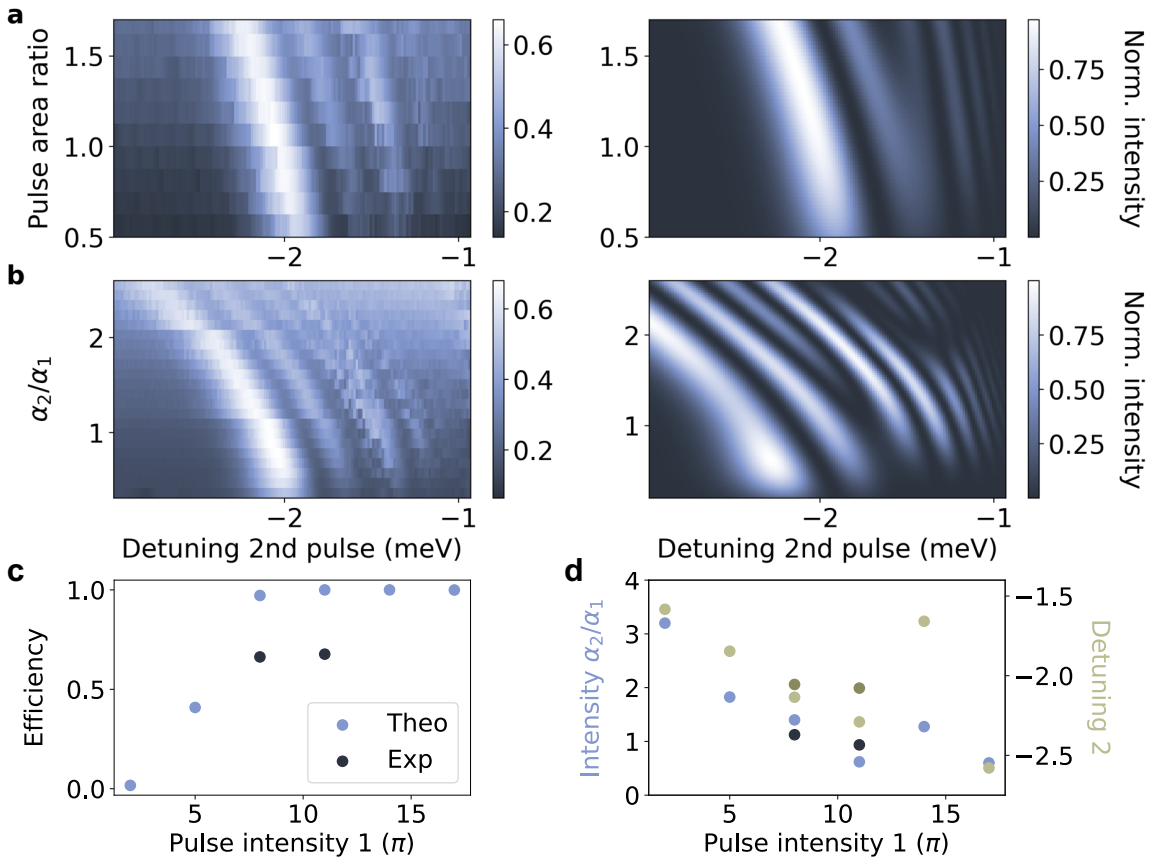

Figure 4.3 | Swing-up excitation resonances for varying excitation parameters in both experiment and simulation. In the colorplots, the normalized emission intensity of the trion (experiment) and calculated upper state population (simulation) is plotted as a function of detuning and intensity of the second pulse. For each plot the parameters of the first pulse are kept constant, both pulses have a length of $10\,\mathrm{ps}$. **a**, The first pulse is fixed at $\hbar\Delta_1 = -0.7\,\mathrm{meV}$ and $\alpha_1 = 8\pi$. Multiple resonances confirm the coherence of the excitation scheme. **b**, The first pulse is kept at $\hbar\Delta_1 = -0.7\,\mathrm{meV}$ and increased in intensity to $\alpha_1 = 11\pi$. **c**, Maximal inversion efficiency as a function of first pulse intensity. The lighter points represent efficiencies and the corresponding pulse parameters extracted from simulations while the darker marks show maximal fidelities from measurements in **a** and **b**. For each point the intensity and detuning of the second pulse were optimized for maximal inversion. Simulations suggest a lower bound of $\alpha_1 = 8\pi$ for efficient excitation. However, in the experiment higher intensities introduce background emission (**b**). Maximal excitation efficiency is found to be 0.68 in the experiment and 1.00 in theory. **d**, Intensity (blue) and detuning (green) of the second pulse needed for maximal inversion efficiency for different first pulse intensities. The two datapoint extracted from the experiment (darker color) are in good agreement with the trend given by the simulations (lighter color).

This is only a slight increase to the case of lower first laser intensity. However, we can hereby confirm that theoretically population inversion with unity fidelity is possible with the swing-up technique with zero time delay between the pulses [91], in contrast to claims in previous work [89]. For higher pulse areas of the second laser pulse, a background becomes visible in the experimental emission spectra. In this context, we define background as emission from the trion under non-resonant excitation by the laser pulses for high pulse intensities, i.e. emission beyond and in-between the swing-up resonance lines. As this emission is non-coherent, we suggest to stay at lower intensities for any applications requiring high-quality single photons or a specific precise excitation within an energy level configuration. Tracking the maximal inversion efficiency across a series of first pulse intensities from $\alpha_1 = 2\pi$ to 17π in the simulation (Figure 4.3c) we see a strong approximately linear increase in inversion efficiency for increasing pulse area from 2π to 8π. Consistent with our experimental results, for larger first pulse intensities we see a saturation of the inversion efficiency around 1.00 in the simulations, and around 0.68 in the experiment, for pulse areas above 8π. Note that the intensity and detuning of the second laser pulse were optimized for each point. The parameters of the second laser pulse for highest population inversion for each first pulse intensity are given in Figure 4.3d. With increasing first pulse intensity, the required detuning of the second pulse (green) decreases, while the intensity of the second pulse (blue), normalized to the first pulse, decreases as well. The experimental datapoints, shown in a darker color, extracted from the measurements in Figure 4.3a and b follow the trend seen in the simulation. The full simulation data is provided in the appendix.
Taking increased background emission at higher laser intensities into account, a trade-off between high efficiency and good single-photon quality and coherent excitation might be unavoidable for implementation of the swing-up scheme in solid-state systems.

Sensitivity on pulse delay

To further study the parameter space of the excitation, we look at the timing of the two swing-up excitation pulses. Therefore, we reduce the intensity of the first pulse to 8π to have a simpler resonance structure for comparison and to minimize the background (Figure 4.4a). We then delay the second pulse by 4 ps with respect to the first pulse. For 10 ps pulses, this corresponds to roughly 40% of the pulse length. Theory suggests that the spectra are identical for positive and negative time delay [89]. The results both for experiment and simulation are shown in Figure 4.4b. The resonance lines visible in the spectra are very similar to the ones for zero time delay, with the dominant resonance and the weaker ones occurring at similar detuning

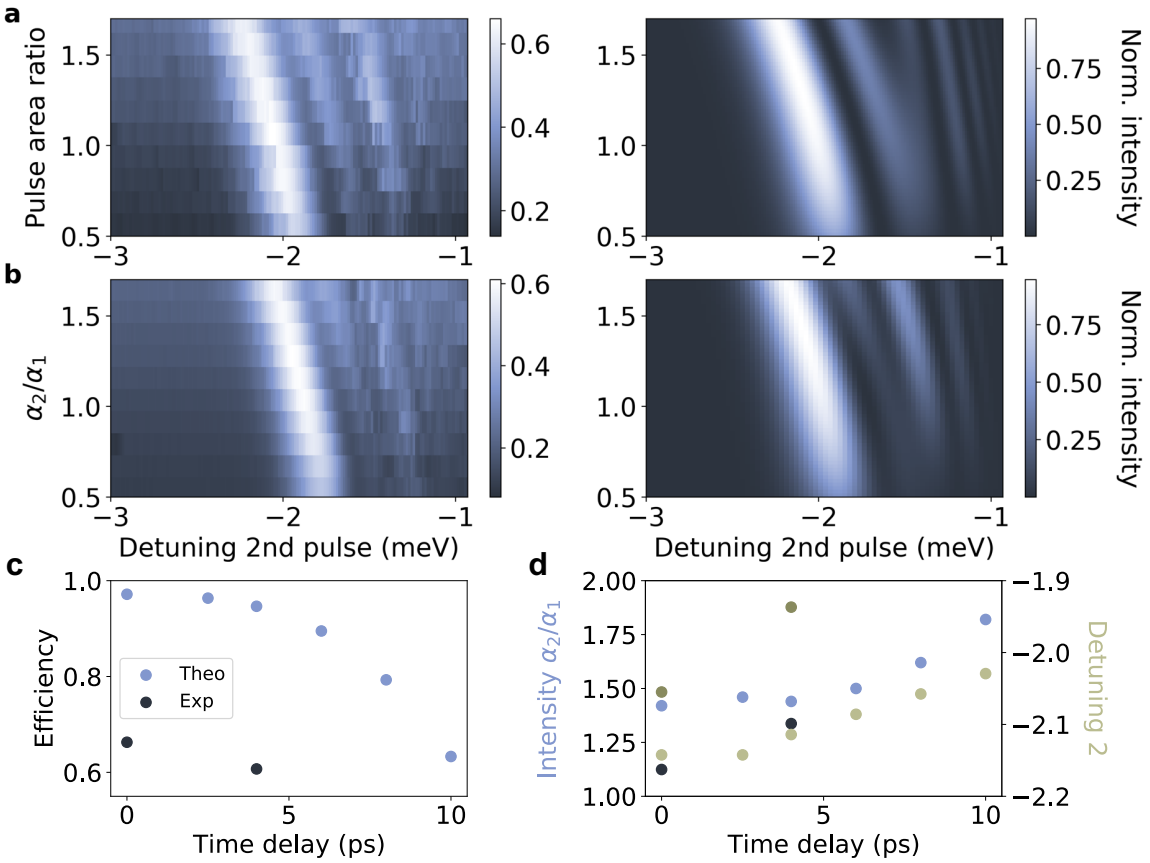

Figure 4.4 | Impact of time delay between the swing-up pulses. **a**, Swing-up resonances for the parameters of the first pulse constant at $\hbar\Delta_1 = -0.7\,\mathrm{meV}$ and $\alpha_1 = 8\pi$, without timedelay between the pulses, as reference. **b**, The second pulse was delayed by $4\,\mathrm{ps}$ while the parameters of the first pulse were kept constant. To find resonances and characterize the excitation for these pulse parameters, the detuning and intensity of the second pulse was varied. **c**, Lighter marks represent the maximal efficiencies and corresponding excitation parameter sets of the swing-up inversion as a function of time delay while the darker marks give maximal efficiencies and their position for experimental results. For each time delay ranging from 0 to $10\,\mathrm{ps}$, the intensity and detuning of pulse 1 were kept constant at $\hbar\Delta_1 = -0.7\,\mathrm{meV}$ and $\alpha_1 = 8\pi$, while the detuning and intensity of pulse 2 were optimized for maximal efficiency at each point. **d**, Optimal values for detuning and intensity of the second pulse for each time delay. Overall, the efficiency decreases only for significant separation of the two pulses in time, while the position of the maxima varies only slightly.

and intensity of the second pulse. Interestingly, the maximal population inversion efficiency is only slightly reduced to 0.61 at $\alpha_2/\alpha_1 = 1.33$ and $\hbar\Delta_2 = -1.94\,\mathrm{meV}$ in the experiment and to 0.95 in the simulation. Scanning the time delay from full overlap of the pulses at 0 ps to full separation in time at 10 ps in the simulation, we see a clear decrease in excitation fidelity as shown in Figure 4.4a in light blue. However, for time delays where both pulses significantly overlap in time, the variation in efficiency is only minor. Consequently, the swing-up technique is robust for uncertainties in timing of the pulses. Our experimental values, as shown in the darker color in the figure, are consistent with the trend of the simulated series. For this time-dependent analysis, the parameters of the first pulse were not changed, while the intensity and detuning of the second pulse was optimized for each time delay for maximal efficiency. The position of the maximal efficiency with respect to the intensity (blue) and detuning (green) of the second pulse are shown in Figure 4.4d. Consistent with experimental observation, the position does not change much for both parameters. The full simulations for the time delay series are provided in the appendix.

Pulse duration-dependence

As a next step, we decrease the pulse length from 10 to 5 ps and investigate the characteristics of the swing-up technique using a second QD on the same sample and within the same diode window.

For resonant excitation of QDs shorter pulses have the advantage of reduced re-excitation [172]. At the same time, however, with decreasing pulse length the required power for similar pulse area increases quadratically. Hence, significantly higher excitation intensities for shorter pulses in the experiment are necessary. In particular, going from 10 to 5 ps pulses, the average excitation intensity as measured with a powermeter in the resonance fluorescence setup is increased by a factor of 3. While for resonant excitation this has little impact, scaling up to multiple π in pulse area as common for swing-up excitation results in high differences in absolute excitation power. This is observable by the noticeably higher background emission for larger second pulse intensities in Figure 4.5, where we fix the first laser pulse at $\hbar\Delta_1 = -1.65\,\mathrm{meV}$ and $\alpha_1 = 9\pi$ and scan the detuning and intensity of the second laser pulse in analogy to the measurements above. Additionally, there is a larger mismatch between experimental and theoretical data which can be attributed to the higher absolute intensities, in agreement with measurements for longer pulses and higher pulse intensities as previously discussed (Figure 4.3). Overall, characteristics as for longer pulses are observable, including resolving several resonances. Here, we achieve a maximal efficiency of 0.80 at $\alpha_2/\alpha_1 = 2.00$ and $\hbar\Delta_2 = -5.24\,\mathrm{meV}$ in the experiment. However, it is strongly

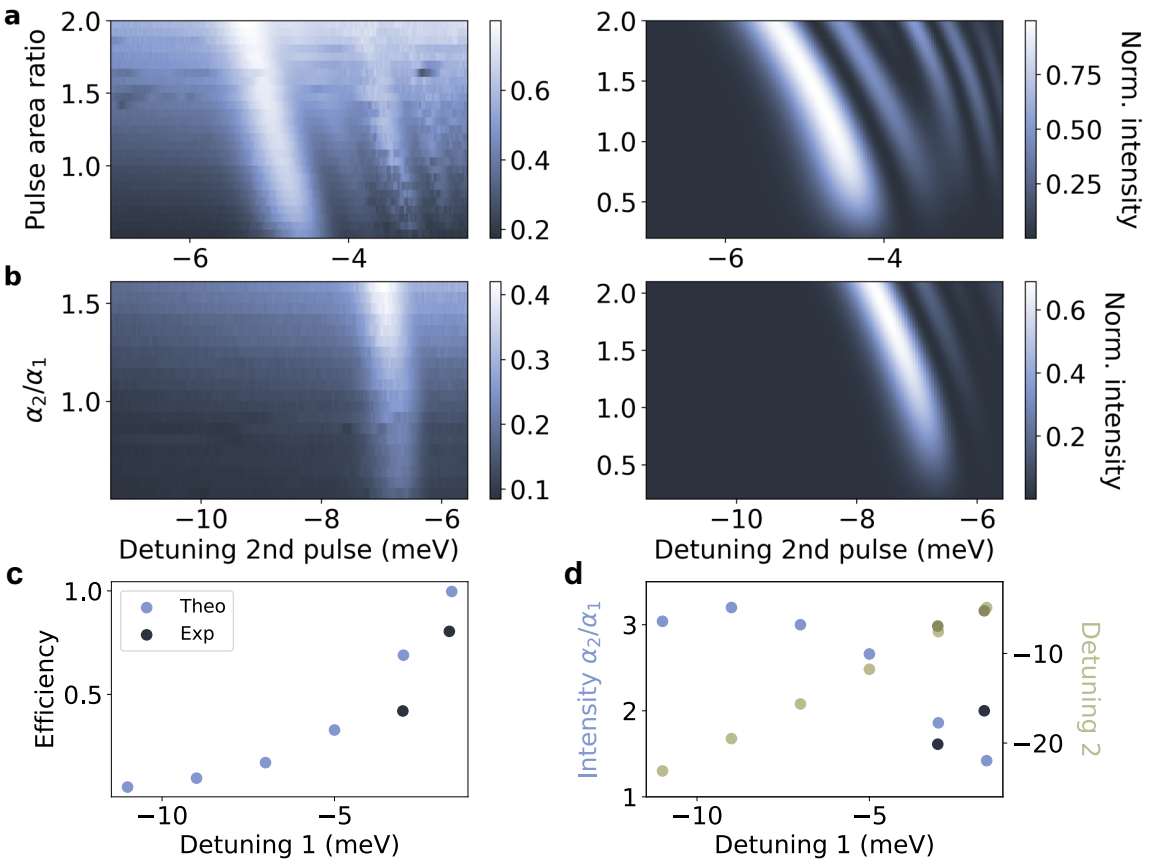

Figure 4.5 | Trion emission intensity and simulated population inversion efficiency for swing-up excitation with $5\,\mathrm{ps}$-pulses and varying pulse detuning. **a**, The detuning and normalized intensity of the second pulse is varied in each subgraph, while the parameters of the first pulse are fixed at $\hbar\Delta_1 = -1.65\,\mathrm{meV}$ and $\alpha_1 = 9\pi$. **b**, The detuning of the first laser pulse was increased to $\hbar\Delta_1 = -3\,\mathrm{meV}$, while being kept constant at $\alpha_1 = 9\pi$. **c** Maximal achieved efficiencies for varying first pulse detuning with fixed first pulse intensity at 9π. The lighter marks represent simulations, whereas the darker markers denote maximal efficiencies and their respective positions for the experimental results from **a** and **b**. For each point, the detuning and intensity of pulse 2 were optimized for maximal efficiency, the corresponding parameters are shown in **d** in green and blue, respectively. Note that the experimental points (darker color) only represent a lower bound for efficiency and second pulse parameters, as the point of maximal efficiency is outside the measured region. For both shorter pules and increasing detuning or the first pulse, the detuning of the second pulse needs to be increased.

overlayed with background emission and is at the edge of the measured parameter regime, so that no definite conclusion can be drawn from this value. In the simulation, we observe a maximal upper state population of 1.00 at slightly lower second pulse intensities. The maximal efficiency values and their corresponding parameters are presented in Figure 4.5c and d.

Influence of pulse detuning

As a last excitation parameter, we increase the detuning of the first laser pulse to $\hbar\Delta_1 = -3\,\mathrm{meV}$. Tuning the intensity and detuning of the second pulse while recording the emission intensity and calculating the upper state population, respectively, reveals resonance lines with a clear maximum that is shifted to larger detuning and higher pulse intensity. Both in experiment and simulation it is shifted outside the measured region in Figure 4.5b, with efficiency maxima observed at the edge of the plot with 0.40 at $\alpha_2/\alpha_1 = 1.61$ and $\hbar\Delta_2 = -6.95\,\mathrm{meV}$ in the experiment and an inversion efficiency of 0.68 in the simulation. The shift to higher intensities and detuning is consistent with earlier theoretical work [89]. This trend becomes evident in the simulation series for varying the detuning of the first pulse as presented in Figure 4.5c and d. Here, the maximal achievable efficiency is plotted against the detuning of the first pulse in c, while the corresponding intensity and detuning of the second pulse, optimized for highest efficiency for each point, are shown in d. Note that the intensity of the first laser pulse was kept constant at 9π. The efficiency of the swing-up excitation drops significantly with increasing detuning of the first laser, as seen in Figure 4.5c. We observe a linear increase in detuning of the second laser pulse with the detuning of the first laser pulse and an increase in second pulse intensity with increasing detuning (Figure 4.5d). The experimental values match well to theory with respect to detuning, while for intensity of the second pulse, no clear statement can be made, as the values represent a lower bound for the second pulse intensity in their specific plots. The full simulations from which the points of maximal inversion efficiency are extracted are presented in the appendix.

The optimal parameter set

Overall, the results suggest keeping detuning and intensities of the laser pulses low, for efficiency excitation and low background emission. Moreover, choosing longer excitation pulses facilitates spectral filtering and further reduces the background. For the specific case of our sample, we find optimal excitation with the first pulse set to $\hbar\Delta_1 = -0.7\,\mathrm{meV}$ and $\alpha_1 = 11\pi$, the second pulse at $\alpha_2/\alpha_1 = 0.94$ and $\hbar\Delta_2 = -2.08\,\mathrm{meV}$, and a pulse duration of 10 ps for both pulses, corresponding to the maximal excitation efficiency in

Figure 4.3b. This excitation parameter set yields a high inversion efficiency of 0.68 in the experiment and near-unity population inversion in theory, while having minimal background emission. Compared to previous work [148] where swing-up excitation is compared to two-photon-excitation of the biexciton, we achieve a slightly lower inversion fidelity for this chosen parameter set in the experiment. Using these above mentioned parameters for optimal swing-up excitation in our sample, we now move on to investigate the properties of the photons emitted using this method.

4.3 Single-photon properties

General emission characteristics

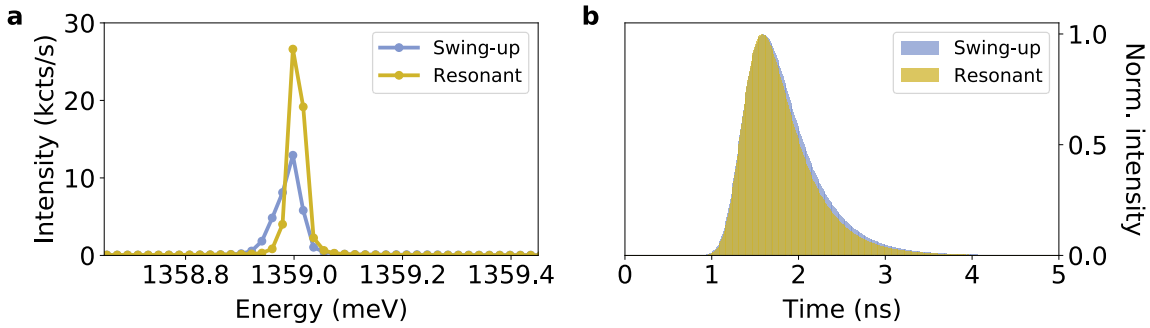

Figure 4.6 | Emission characteristics under swing-up excitation (blue) in comparison to resonant excitation (yellow). **a**, Trion emission under the two excitation methods recorded by a spectrometer. The emission peak under swing-up excitation is broadened and red-shifted in energy with respect to resonant excitation. **b**, The radiative lifetime under the swing-up excitation with $450 \pm 14\,\mathrm{ps}$ is comparable to the resonant lifetime of $419 \pm 13\,\mathrm{ps}$.

As a start to analyzing the emission properties of the QD under swing-up excitation, we look at its time-integrated frequency-resolved emission and compare it to resonant excitation. The resulting spectra are plotted in Figure 4.6a. As both spectra were taken in the resonance fluorescence setup which includes cross-polarized filtering which reduces the intensity by 50%, and taken the previously discussed reduced inversion efficiency under swing-up excitation of 0.68 into account, the emission under swing-up excitation results in lower integrated intensity than emission under resonant excitation. Note that the cross-polarized filtering would not be necessary for swing-up excitation when employing spectral filtering which would increase the detection efficiency and the recorded emission intensity by a factor of 2. Furthermore, the emission under swing-up excitation is red-detuned by 11 µeV and slightly broadened. Even though choosing lower pulse intensities for swing-up excitation to avoid background emission

and divergence from the theoretical calculations, the absolute powers for the used pulse parameter set are still in the μW regime. Laser intensities in this power range cause local heating, leading to a shift in resonance. Moreover, high laser intensities generate charge noise which causes spectral diffusion, i.e. establishing itself as broadening of the emission line in the experiment. We confirm that these artifacts solely originate from the high laser intensities in combination with our sample by looking at other excitation methods under similarly high absolute excitation powers, i.e. two-photon excitation of the biexciton cascade and phonon-assisted excitation, where we observe similar emission characteristics. Details on these measurements and the results are given in the appendix. This observation implies that the swing-up excitation itself does not decrease the emission quality directly, meaning that the emission properties can be optimized using more sophisticated samples. One way would be to use broadband cavities such as bullseye resonators or weak planar cavities, which increase the coupling of the TLS to the light field and thus reduce the required intensities in the experiment while still allowing for off-resonant excitation [173]. Moreover, one could reduce the charge noise by embedding the QDs in a p-i-n diode instead of a Schottky diode, or by improving the design and quality of the Schottky diode itself.

We next look at time-resolved emission. To this end, we additionally filter the emission peak spectrally from the remaining laser reflection off the sample and record it with a SPAD and a quTAG time-to-digital converter. To study the excited-state lifetime under both excitation methods, the emitted photons were detected time-tagged with respect to the laser pulse and integrated in time to obtain a clear histogram. The results are shown in Figure 4.6b. The lifetimes of 450 ± 14 ps and 419 ± 13 ps for the trion emission under swing-up and resonant excitation, respectively, are in very good agreement within the measurement uncertainty. This rules out unwanted effects related to the swing-up excitation process, by confirming excitation on the picosecond timescale.

Single-photon purity

To determine the single-photon purity of the photons emitted by our TLS under swing-up and resonant excitation and thus quantify the performance of the QD as a single-photon source under different excitation methods, we take a look at the second order coherence function $g^{(2)}(\tau)$. The degree of second order coherence in terms of photonic operators a and $a^\dagger$ is given by

$$g^{(2)}(\tau) = \frac{\langle a^\dagger(t)a^\dagger(t+\tau)a(t+\tau)a(t)\rangle}{\langle a^\dagger(t)a(t)\rangle\langle a^\dagger(t+\tau)a(t+\tau)\rangle} \tag{4.4}$$

where τ is the time delay. For zero time delay $\tau = 0$ it can be simplified to

$$g^{(2)}(0) = \frac{\langle a^\dagger a^\dagger a a \rangle}{\langle a^\dagger a \rangle^2} \tag{4.5}$$

The shape of the second order correlation function, in particular the value at $g^{(2)}(\tau = 0)$ provides information on the nature of the light and the statistical distribution of intensity or photons within the field [133, 131, 164]. The $g^{(2)}(\tau)$ function itself is normalized to 1 for long time delays τ where the photons are uncorrelated. In contrast, the value at $g^{(2)}(\tau = 0)$ depends strongly on the properties of the light, i.e. the distribution of photons/intensity with time or space within the investigated light beam. For coherent light like a laser field $g^{(2)}(\tau = 0) = 1$, making the curve overall flat. For such a light source the intensity is constant over time and the distribution of photons within the light beam is perfectly random and can be described by a Poissonian distribution. This changes for thermal light, where the photons are grouped in bundles, giving rise to 'bunching' at zero delay, i.e. $g^{(2)}(\tau = 0) > 1$. In terms of photon distribution, this kind of light can be described as super-Poissonian. Note that for a classical description of the second order coherence, the value of $g^{(2)}(\tau = 0)$ is limited to ≥ 1. However, in the above picture $g^{(2)}(\tau = 0) < 1$ is by all means possible, describing quantum light with a sub-Possonian distributions of photons within the field. This could be realized by coherent excitation of a single-photon source consisting of a TLS, which is able to emit only one photon at a time. It can be calculated that a value of $g^{(2)}(\tau = 0) < 0.5$ proves single-photon character for a quantum emitter, with $g^{(2)}(\tau = 0) = 0$ being a perfect light source in that regard [133].

In the experiment, the second order correlation function is approximated by auto-correlation measurements in a Hanbury-Brown-Twiss-type of setup [174]. Here, the photon stream of the light source is divided by a beamsplitter into two different paths. Single-photon detectors record incident photons in both paths separately and their detection events are then correlated in time. For a perfect single-photon source where single photons are emitted and sent to the beamsplitter one after another, only one detector can detect a photon at a time. An individual photon can never create a signal in both arms simultaneously, as the photon is projected to either one of the beamsplitter outputs upon detection. Thus, in the correlations between the two detectors, no signal is detected for zero time delay in the ideal case. For details, please refer to the appendix.

The resulting correlations for emitted photons under swing-up and resonant excitation are presented in Figure 4.7 in blue and yellow, respectively. Without subtracting a background, the raw values are $g^{(2)}(0)_{\text{swing,raw}} = 0.033 \pm 0.001$ and $g^{(2)}(0)_{\text{res,raw}} = 0.031 \pm 0.001$. As correction of the $g^{(2)}(0)$ value for background com-

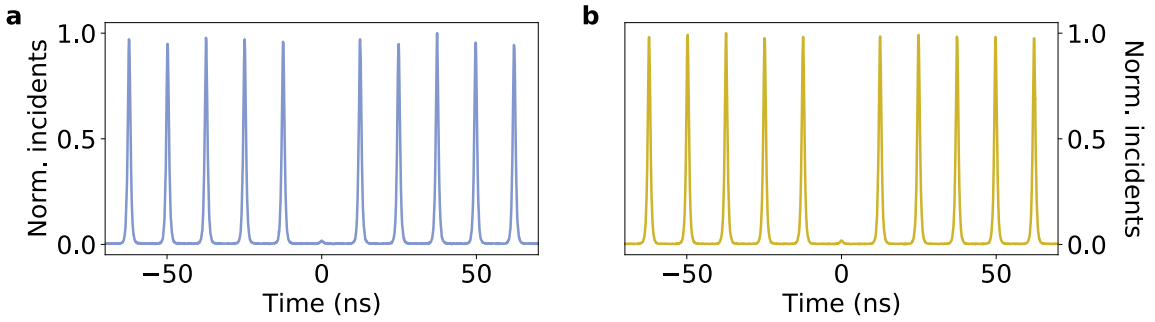

Figure 4.7 | Second-order correlation function in the experiment. **a**, Emission of the trion under swingup excitation characterized in terms of single-photon purity. The resulting values of $g^{(2)}(0)_{\text{swing,raw}} = 0.033 \pm 0.001$ is in very good agreement with **b**, the value under resonant excitation $g^{(2)}(0)_{\text{res,raw}} = 0.031 \pm 0.001$.

monly increases the error for the resulting values and a variety of different analyzation methods is used within the research community, we specifically state the raw values here as an upper limit for the $g^{(2)}(0)$ value. However, as the SPADs used for single-photon detection cause significant background due to their non-negligible darkcount rate, we additionally provide the background-subtracted $g^{(2)}(0)$ values yielding corrected results of $g^{(2)}(0)_{\text{swing, corr}} = 0.013 \pm 0.001$ and $g^{(2)}(0)_{\text{res,corr}} = 0.016 \pm 0.001$ for swing-up and resonant excitation, respectively. The values under the two different excitation techniques are not only in excellent agreement, but also close to the intrinsic limit given by re-excitation for the chosen pulse length of 10 ps [175]. From these results we conclude that the swing-up excitation method does not influence the single-photon purity of a quantum emitter.

Indistinguishability

Another important parameter to quantify is indistinguishability of the emitted photons. It is highly relevant for any application involving operations relying on interference, such as generation of complex graph states through linear optics [54, 176, 177, 178, 158, 87, 61], or interference of photons between different repeater nodes [162, 163]. The evaluation of the indistinguishability of single photons in the measurement is based on the Hong-Ou-Mandel effect [166] which relies on the interference of two photons on a beamsplitter. For two identical photon inciding on a beamsplitter from the two different input ports, the output state can be calculated to

$$|\psi\rangle_{out} = -r^* t\,|2,0\rangle + (|\,t\,|^2 - |\,r\,|^2)\,|1,1\rangle + rt^*\,|0,2\rangle \tag{4.6}$$

where $|i,j\rangle$ are the joint Fock states for the output and r and t are the reflection and transmission coefficient of the beamsplitter [131]. In the term representing output of

the two photons in each port separately $|1,1\rangle$, destructive interference occurs, reducing its observance in the experiment. For a 50/50 beamsplitter $\mid r \mid^2 = \mid t \mid^2 = \frac{1}{\sqrt{2}}$, thus the mixed term vanishes completely leading to

$$|\psi\rangle_{50/50,out} = \frac{1}{\sqrt{2}}(|2,0\rangle - |0,2\rangle) \tag{4.7}$$

In the experiment this means that two incident photons from different ports on an equal beamsplitter are projected on either one of the output ports with a 50/50 probability by the act of measurement. With the measurement, the state collapses to either $|2,0\rangle$ or $|0,2\rangle$, whereby the two photons always remain paired in their output port. As this is only valid for identical photons, the degree of indistinguishability of single photons can be measured by overlapping them on a beamsplitter and measuring the correlations of the output paths. Given that we are working with photons from a single-photon source, a fraction of the photons needs to be delayed in time to coincide with the subsequent photon on the beamsplitter, as can be realized in an unbalanced Mach-Zehnder interferometer (further elaborated in the appendix) [81]. To reduce the decoherence effect on long timescales and facilitate the experiment, we doubled the repetition rate by introducing a second set of excitation pulses with 3 ns delay to the previous ones. Based on the resulting correlations, we assess the central peak, which ideally diminishes, in comparison to its adjacent peaks. This evaluation allows us to determine the HOM visibility, a direct measurement of the indistinguishability of the single photons.

The HOM-visibility of the trion emission under swing-up excitation is measured to be $v_{\mathrm{HOM,swing}} = 0.439^{+0.047}_{-0.049}$ in our sample as shown in Figure 4.8a in blue. The value is lower compared to its resonant counterpart of $v_{\mathrm{HOM,res}} = 0.663^{+0.032}_{-0.035}$, depicted in yellow in Figure 4.8a. A detailed analysis of the error estimation is presented in the appendix. The resonant value is reduced to typical indistinguishability values for similar systems in literature, which yield results above 0.99 [179]. We attribute the reduced HOM visibility to co-tunneling of the electron in the ground state to the reservoir provided by the n-doped layer in the sample design. Furthermore, the impact of high laser intensities on the sample during swing-up excitation which lead to broadening and spectral shift, as explained previously, inevitably negatively impact the HOM-visibility of the single photons with respect to resonant excitation. To circumvent the impact of the co-tunneling of the electron to the reservoir, we additionally investigate the crystal ground state-neutral exciton transition as the TLS. Here, the HOM-visibility for resonant excitation improves to $v_{\mathrm{HOM,res},X^0} = 0.821^{+0.019}_{-0.018}$ shown in yellow in Figure 4.8b, confirming our argumentation of co-tunneling limiting the indistinguishability. However, for swing-up excitation of the neutral exciton, in

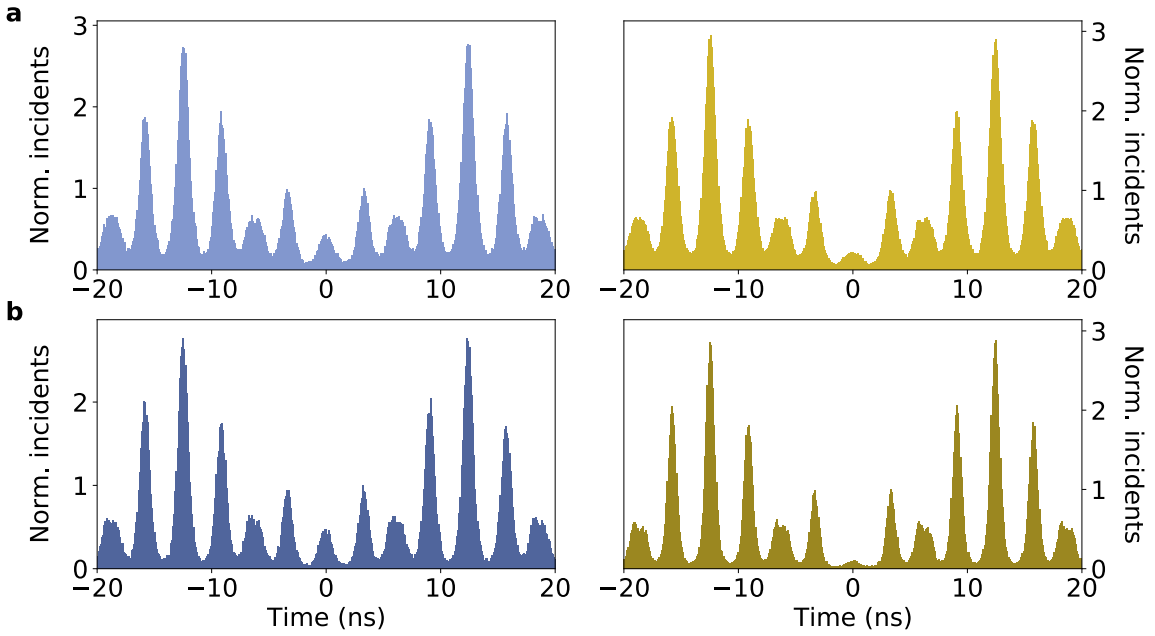

Figure 4.8 | Indistinguishability measurements for swing-up (blue) and resonant excitation (yellow), for different excitonic transitions. **a**, For the trion X^-, the measured HOM visibility with $v_{\mathrm{HOM},X^-,\mathrm{swing}} = 0.439^{+0.047}_{-0.049}$ is lower compared to **b**, the value of $0.663^{+0.032}_{-0.035}$ for resonant excitation. For the neutral exciton X^0 the HOM visibility under resonant excitation $v_{\mathrm{HOM},X^0,\mathrm{res}} = 0.821^{+0.019}_{-0.018}$ is higher, while for swing-up excitation it is further reduced to $v_{\mathrm{HOM},X^0,\mathrm{swing}} = 0.397^{+0.041}_{-0.041}$.

addition to the high laser intensities causing noise and decreasing spectral overlap, resonances with the two-photon excitation of the biexciton overlap in part with swing-up resonances. This complicated the excitation and reduces the indistinguishability further to $v_{\mathrm{HOM,swing},X^0} = 0.397^{+0.041}_{-0.041}$ (Figure 4.8b, blue), as photons emitted from the neutral exciton via the biexciton cascade are subject to and additional timing-jitter [180]. Overall, both the indistinguishability of photons under resonant excitation due to co-tunneling and under swing-up excitation due to additional high laser intensities can be enhanced by improving the sample structure as discussed earlier in this section.

Origin of limited excitation fidelity

To further investigate the nature of the limited excitation fidelity under swing-up excitation in the experiment, we look at the intensity oscillations between in the output of the Mach-Zehnder interferometer. As described by Loredo *et al.* [181], the intensity oscillations between the two detectors in un unbalanced Mach-Zehnder interferometer provide information on the purity of the excited state. High antisymmetric oscillations in integrated detection events between the two detectors, typically on the timescale of seconds, are attributed to excitation of a superposition between the vacuum and

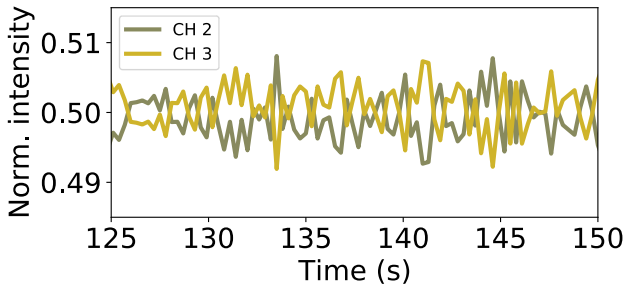

Figure 4.9 | Normalized intensity oscillations between the two detectors in the unbalanced Mach-Zehnder interferometer. CH1 and CH2 correspond to the integrated intensity of the two detectors. Antiphased oscillations with low amplitude indicate the limited excitation fidelity being of statistical mixture in nature.

first Fock state [181]. The oscillations are low in amplitude in our measurements (Figure 4.9), confirming that the limited excitation fidelity originats from a statistical mixture rather than the excitation of a superposition, i.e. not a direct excitation of the excited state. This is consistent with our previous assumptions that noise and decoherence by the high laser intensities cause a reduction of the excitation fidelity through loss of charge carriers, spectral diffusion and experimental uncertainties.

4.4 Summary

In this chapter, we have studied the recently proposed swing-up excitation method [89]. Specifically, we focused on the feasibility of exciting on feasibility for excitation of transitions in semiconductor QDs and the properties of the subsequently emitted photons. The excitation technique holds great promise as it is coherent while enabling spectral filtering at the same time. After describing the concept of the scheme and demonstrating the successful implementation in the experiment, we investigated the influence of the individual excitation pulse parameters on the scheme. Here, we found several resonances with respect to detuning and intensity variation which confirm the coherence of the scheme. Moreover, we found an optimal inversion efficiency of 0.68 in the experiment under the condition of inducing minimal background. The theoretical inversion fidelity if calculated to be near-unity in the same parameter regime. For these excitation parameters we investigated the properties of the photons emitted upon exciting the QD with this technique. The single-photon purity with $g^{(2)}(0)_{\mathrm{swing,corr}} = 0.013 \pm 0.001$ in very good agreement with the single-photon purity under resonant excitation, while the indistinguishability is limited to $v_{\mathrm{HOM,swing}} = 0.439^{+0.047}_{-0.049}$. Furthermore, we discussed that the efficiency and limited indistinguishability can be increased with improved sample structures which enhance light-matter coupling and are less susceptible to

noise.

Chapter 5

Conclusion and outlook

Contents

In this chapter, we summarize the work presented within this thesis with a focus on the main novel results presented in Chapters 3 and 4. We then move on to suggesting experiments which can be performed based on this thesis as a follow-up work and possible applications based on findings of this thesis, focusing on emission from dynamically dressed states and the swing-up excitation scheme employing semiconductor QDs.

5.1 Summary

We started this thesis in Chapter 1 with describing the relevance of quantum optics in modern photonic quantum technology and explained the current challenges with respect to fundamental understanding of the underlying physics and to optical excitation techniques for quantum emitters and qubits. In this context, we described how our work contributes to solving these challenges.

In Chapter 2 we explained the fabrication of our sample and how a single InGaAs QD is used as a quantum TLS. After explaining the growth of the QDs with MBE in a pre-defined structure including a bottom DBR and n-doped layer, we described the fabrication of diode contacts with optical lithography and metal evaporation. We then

explained charge carrier confinement to discrete states in single QDs and show charge control and fine-tuning of the QD resonances with varying voltage. In our sample, either the neutral exciton or the negatively charged trion can be optically excited. This sets the basis for our subsequent measurements.

We continued with resonance fluorescence measurements in Chapter 3. Here, we first theoretically described the coupling of a resonant cw light field to a TLS, following an experimental demonstration of the Mollow triplet in emission, with excitation-dependent properties. Afterwards, we looked at the resonance fluorescence emission spectrum under resonant but pulsed excitation using Gaussian pulses in the picosecond range. We provided an intuitive explanation of the origin of the multiple sidepeaks in the emission and showed the first experimental observation of the full resonance fluorescence spectrum from a single TLS. We confirmed that the spectral position and width of the individual sidepeaks strongly depends on the pulse length, while the number of the peaks depend on the pulse are, i.e. the Rabi rotations driven by the pulse, as predicted by earlier theoretical work [37, 33, 32]. Furthermore, we showed that the emission can be separated into the dressed part of the spectrum and the light emitted during the radiative lifetime of the QD by detuning-dependent measurements. The dressed emission behaves in analogy to the Mollow triplet under excitation with finite detuning. Theoretical calculations support our experiments and are in good agreement.

In Chapter 4 we explained how dressed states under pulsed excitation can be used for a more application-oriented concept, i.e. for the swing-up optical excitation technique. The recently proposed swing-up excitation technique [89] uses two red-detuned pulses to excite a TLS and promises coherence, while allowing for spectral filtering, which we describe in detail. We demonstrated the functionality and coherence of the scheme and studied the impact of the individual parameters on the excitation fidelity and resonances. In the experiments, we found an optimal parameter set with efficiency of 0.68, while theory suggests near-unity excitation fidelity. On the other hand, we found good agreement between experimentally and theoretically observed resonance lines. We continued with studying the single-photon properties under swing-up excitation. The time-integrated spectrum under swing-up excitation reveals a broadened and red-shifted emission peak which we attribute to the high laser intensities. We found a single-photon purity with $g^{(2)}(0)_{\mathrm{swing,corr}} = 0.013 \pm 0.001$ which is in very good agreement with the value of $g^{(2)}(0)_{\mathrm{res,corr}} = 0.016 \pm 0.001$ under resonant excitation and close to the limit given by re-excitation. The indistinguishability for the negatively charged trion with a HOM visibility of $v_{\mathrm{HOM,swing}} = 0.439^{+0.047}_{-0.049}$ is reduced with respect to resonant excitation where $v_{\mathrm{HOM,res}} = 0.663^{+0.032}_{-0.035}$ which we attribute to spectral diffusion and decoherence caused by the high laser intensities. For resonant excitation,

the indistinguishability is mainly limited by co-tunneling of the electron in the ground state to the n-doped contact which we confirmed by measuring the HOM visibility of the neutral exciton to $v_{\mathrm{HOM,res},X^0} = 0.821^{+0.019}_{-0.018}$. However, we argued that the indistinguishability of photons emitted under swing-up excitation can be improved by enhancing the sample design by better diodes or implementing the QD in a broadband cavity.

We now conclude with this summary and give an outlook on follow-up experiments and possible applications.

5.2 Outlook

Time-resolved analysis of dynamically dressed states

For more insight into the dynamics of the dressed states under pulsed excitation we propose investigating time-resolved photoluminescence as a next step. Especially the emission time of different frequency-filtered parts of the spectrum could shed further insight into the origin and dynamics of the sidepeaks. As proposed in Chapter 3 and recently shown by Liu *et al.* [147] the emission of the sidepeaks happens on timescales of the excitation pulse, while the emission of the center peak follows the radiative emission lifetime of the excited state. However, following the theoretical description of the dynamical Mollow provided in Ref. [33] we disagree with Liu *et al.* in their explanation of the origin of the sidepeaks and thus suggest an extension of the time-resolved measurements. As the sidepeaks occur only in the time-integrated spectrum due to interference, filtering of a part of the dressed emission strongly influences the spectral intensity distribution [33]. We thus propose to investigate frequency-resolved time-resolved emission characteristics, where a filter with varying width is scanned across the whole resonance fluorescence spectrum. This would strongly contribute to further detailed understanding of fundamental light-matter interaction with resonant short pulses.

Moreover, the investigation of frequency-filtered auto- and cross-correlation measurements of the resonance fluorescence spectrum is highly promising. As for frequency-filtered correlation measurements in the Mollow triplet spectrum under cw excitation [182, 183], analogous study for dynamically dressed states could reveal non-trivial two-photon spectra and give insight into virtual transitions and other complex correlations in-between the main peaks.

In the context of correlation measurements, we suggest investigating full and frequency-filtered second-order correlation measurements of the main emission peak, with the excitation laser on and near-resonance. As we have shown in Chapter 3, the dressed

part of the emission exhibits a broad peak in its center and the whole dressed emission spectrum centered at the laser frequency. This result could be used to modify and filter a large amount of the photons emitted due to re-excitation, as those photons naturally inherit a broader spectral line, while detuning the laser from resonance could increase the filtering effect. Re-excitation is a crucial challenge encountered in any resonant excitation scheme [66, 172, 175].

Dynamical Mollow for non-classical states of light

The insights into the two-frequency correlations characteristics of the dynamical Mollow spectrum could then be used to generate non-classical states of light. In analogy to the Mollow triplet [184], emission of the QD at frequencies off the main resonance could be investigated as an emitter of n-photon bundles with on-demand generation. While such states could be used for generation of NOON states [185] n-photon emitters are particularly interesting for applications in medical imaging [186, 187] and quantum metrology and lithography [188]. Furthermore, our results pave the way for generation of entangled states in the energy-time domain as has recently been shown for quantum systems interacting with cw excitation [189, 190].

Optimized swing-up excitation with broadband cavities

As discussed in Chapter 4, we attribute the limited efficiency, change in spectral shape and indistinguishability of the emitted photons using the swing-up excitation scheme to the effect of high laser powers on the solid-state environment of our QD. While the weak planar cavity in our sample already reduces the absolute laser power intensity necessary for resonant excitation by a factor of 20, embedding the QD in a broadband bullseye resonator would further strongly decrease the required powers due to enhanced light-matter coupling [173, 191, 192, 193, 194]. In this way, the interaction of the laser with the solid-state environment, i.e. unwanted generation of charges etc. would be strongly reduced, especially with the increased signal.

Furthermore, we recommend optimizing the diode structure to a cleaner Schottky diode or a p-i-n diode which would prevent trapping of charge carriers on the material interfaces. The fabrication of such structures is already well-established in the community and could be implemented in a new growth and fabrication series of QD samples. In particular, recent work has shown excellent optical properties, including single-photon purity and indistinguishability, from single QDs in Schottky and p-i-n diodes [195, 196].
Implementing the swing-up scheme in a QD transition in such a structure holds great promise for improved performance of the scheme and potential applications.

Swing-up excitation for generation of photonic graph states

Such an application of the swing-up scheme for photonic quantum technologies could be the generation of photonic graph states based on a single quantum emitter, or a system of two coupled emitters. For the generation of one of the most fundamental highly entangled states, a linear cluster state consisting of consecutively entangled photons, Lindner and Rudolph proposed a scheme [167]. It is based on repeated optical excitation and subsequent emission in a double-lambda level system of a single QD. Rotations between the ground states in-between the excitation pulses control the type of graph state in the output, while excitation of the superposition of the excited states leads to entanglement of the subsequently emitted photon in polarization with the spin in the QD. The scheme has been successfully implemented by several groups using phonon-assisted excitation [169] and excitation via the p-shell [86, 61], where the efficiency and brightness still remains challenging. After optimization of the performance of the swing-up scheme by improving the sample design, the swing-up technique could contribute as a coherent excitation method, which allows for the required full polarization degree-of-freedom, while allowing for spectral filtering to isolate emitted photons from the QD from the residual excitation light. Optimization of the Lindner-Rudolph scheme with increased efficiency, brightness and better properties of the emitted photons could pave the way for fusion to larger-dimensional cluster states or generation of two-dimensional cluster states based on two coupled QDs [88, 197]. This would lead us a step closer towards applications [154, 161, 197].

Appendix A

Setups

Contents

As this work is mainly an experimental study, the experimental setups are of crucial importance to the research results presented in this thesis. However, to enhance readability, clarity, and provide an overview of the experimental techniques, we will summarize the main experimental setups that were built, modified, and utilized for the measurements here. This approach allows the main part of the thesis to focus on the measurement results and their discussion.

At first, we sketch and present the two cryostat setups used in this thesis: The μPL setup, employed for characterization of the samples as introduced in Chapter 2, and the resonance fluorescence setup used for the main measurement discussed in Chapters 3 and 4. We then move on to explaining the principle of 4f pulseshaping and the setup enabling generation of fully customizable picosecond pulses. These were used for

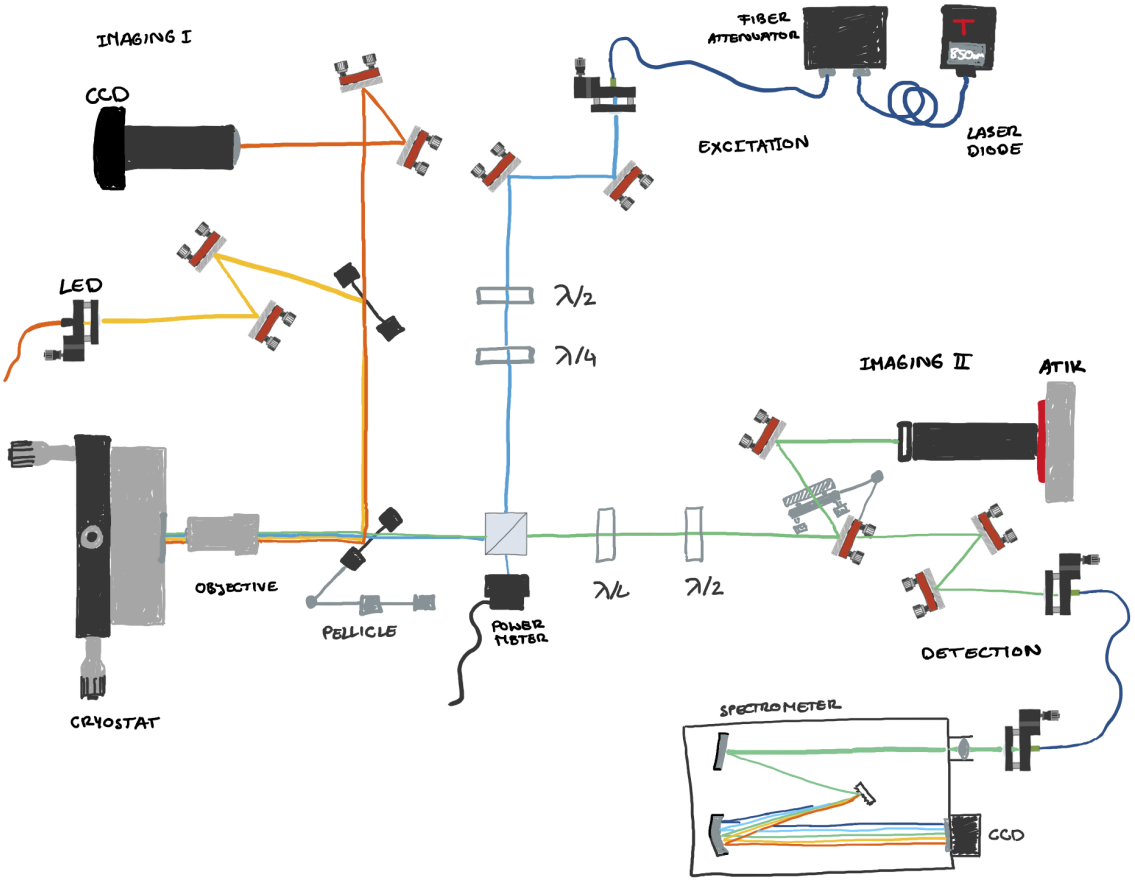

Figure A.1 | μPL setup. For sample and QD characterization, the sample is mounted in a flow-cryostat and cooled to $10\,\mathrm{K}$. The diode is connected to a Keithley 2400 voltage source. An imaging system (orange/yellow) consisting of a LED and CCD camera allow view of the sample surface over a wide range. Via the excitation path (blue), light from a $850\,\mathrm{nm}$ Thorlabs laser diode is sent over two beamsplitters and focused via the objective onto the sample surface.The emitted light (green) is collected via the same objective, filtered by a beamsplitter and long-pass filters and resolved spatially in an Atik 314L+ camera or spectral in a spectrometer and CCD system.

excitation of the TLS for the main measurements presented in Chapters 3 and 4. In a third part, we conclude with optical setups enabling time-resolved correlation analysis of the emitted signal. Specifically, we explain the Hanbury-Brown-Twiss experimental setup for quantification of the single-photon purity, and the unbalanced Mach-Zehnder interferometer used to determine the indistinguishability of the emitted photons from the QD.

A.1 μPL setup

The μPL setup is optimized for characterization of QD samples with optical excitation in the wetting-layer. It consists of a flow-cryostat mounted to the optical table which is optically accessible by an excitation and detection path on the table, as well as an imaging system as sketched in Figure A.1. The flow-cryostat is connected to a Helium dewar and cooled to 10 K. The sample is mounted inside the cryostat and the diodes are connected to pins leading to a Keithley 2400 voltage source. Optical access to the sample is enabled through a cryostat window close to the sample and an objective mounted on the optical table, which focuses and collects light to and from the sample. The cryostat itself can be moved in all three cartesian direction, allowing for adjustment of the sample area investigated, and enabling precise focusing. The optical path of the imaging system is depicted in yellow. A pellicle after the objective reflects part of the light towards an imaging CCD, where the sample surface is imaged with help of a lens system. A LED, coupled to the path with another pellicle illuminates the sample surface. A large field-of-view of about 150 µm is convenient for sample characterization. The LED is optionally used for wide-field excitation of QDs. For excitation of single QDs in the wetting-layer, a laser diode with 850 nm wavelength is connected to the excitation path. It is directed through a beamsplitter onto the sample through the objective. At the beamsplitter in transmission, the power of the excitation is measured. The intensity can be adjusted via a voltage-controlled fiber attenuator, which is connected to the diode prior to the outcoupling into the excitation path. The emitted light from the sample is directed through the objective towards the detection path, where part of it is transmitted through the beamsplitter. It is either coupled into a fiber and sent to a spectrometer or directed via a flip-mirror to a highly sensitive imaging system, where an Atik 314L+ camera allows for spatial resolving single QDs within the diode windows by detecting the emitted light of the QDs. A longpass filter before the Atik camera prevents light from the excitation or LED to overlay with the signal. Optionally, a quarter and a half waveplate in the excitation path and detection path can be inserted for polarization-resolved measurements.

A.2 Resonance fluorescence setup

The optical resonance fluorescence setup was used for the main experiments in Chapters 3 and 4. It consists of an optical head and a stick (Figure A.2), whereby the stick is enclosed in a metal casing, evacuated and filled with exchange gas. It is then immersed in liquid helium in a dewar and cooled to 4.2 K for operation. Besides imaging, the optical head allows for optical excitation and detection of the emission

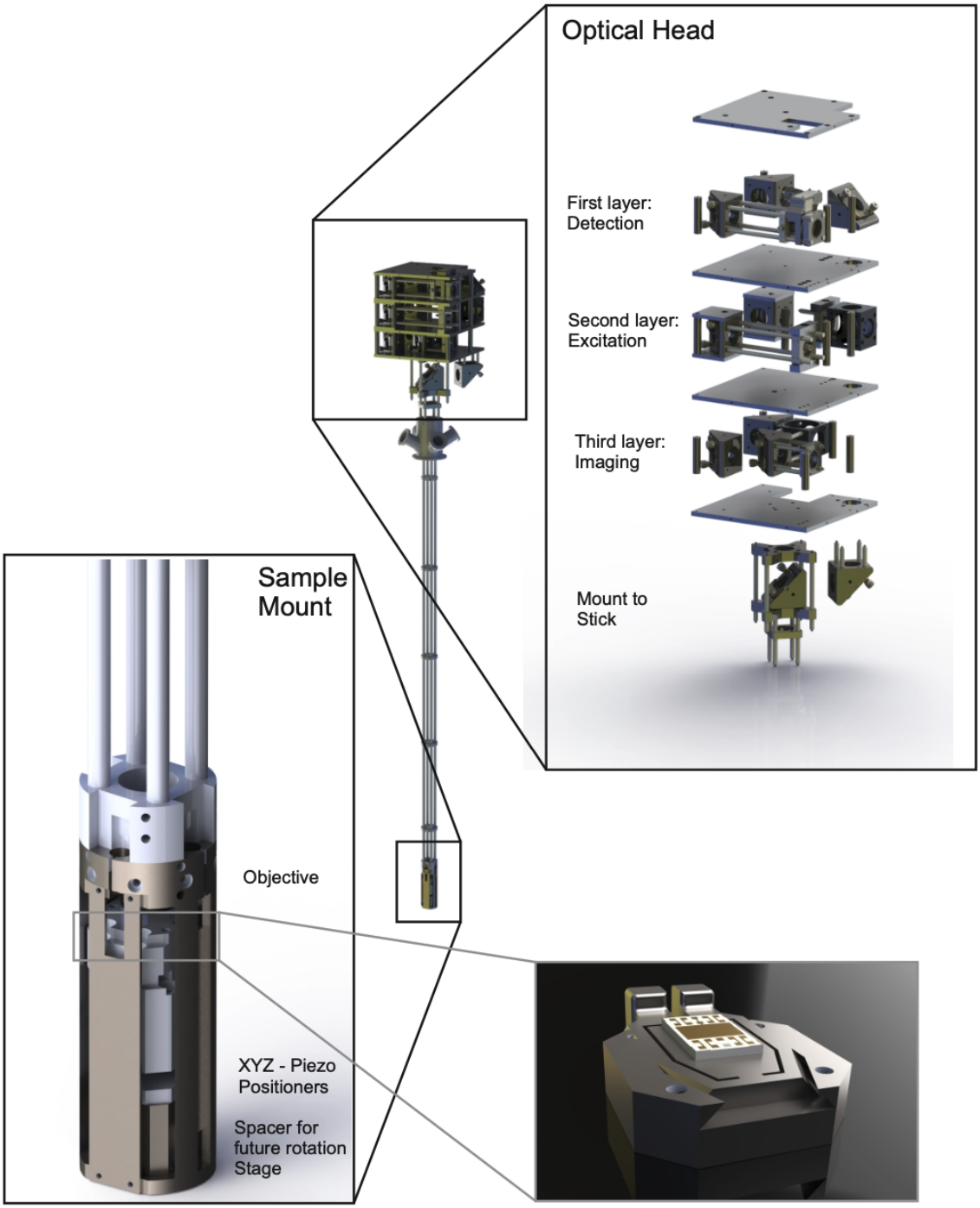

Figure A.2 | Resonance fluorescence setup. It consists of a stick with the sample mounted on piezo positioners at the bottom (bottom left) and an optical head (top right) which allows for optical access. The stick is cooled down to $4.2\,\mathrm{K}$ by inserting it in a casing into a liquid Helium bath. The optical head consists of three layers including imaging, excitation and detection. The excitation and detection path, both following the same path through the stick and focusing onto the sample through a lens at the bottom of the stick, are combined and separated via polarizing beamsplitter. The suppression of the excitation laser in the detection path is further optimized by additional polarizers and a quarter waveplate. The figure is adapted from Ref. [104].

and can be connected via polarization-maintaining optical fibers to various excitation lasers and detection setups depending on the requirements of specific experiments. The optical head and stick are arranged in a confocal microscopy configuration and allow for resonant excitation via cross-polarization filtering [17]. The optical path of head and stick is connected via a wedged cryo window in-between both. The optical path in the stick ends at the bottom with a single lens with a numerical aperture of 0.77, which focuses the excitation on the sample and collimates emitted photoluminescence. The sample is mounted on a attocube piezo stack below the lens. This allows for positioning of the sample with respect to the focus of the lens in a range of 5x5x5 mm, thus enabling to choose diode and QD within the diode window, and allows for adjusting the focus of light with respect to the lens. The contacts of the diode are connected to a Yogokawa 7651 voltage source, where a DC voltage can be applied to control the charge state and resonance of the QD. The lowest layer of the optical head serves for imaging of the sample. A removable pellicle in the optical path going to and from the stick reflects a small fraction of the light into this layer. It is then directed to a CCD camera, where a lens images the surface of the sample onto the camera. In the imaging layer, a LED is connected via a second pellicle to illuminate the sample surface for improved visibility. A field-of-view of several µm allows for orientation on the sample surface and selection of the right diode window, in particular as the real-time readout of the CCD on the PC can be operated in parallel to the piezo positioners. The mid layer of the optical head is designed for excitation. The excitation light is out-coupled from a polarization-maintaining fiber and collimated. After passing a rotatable polarizer, it is reflected off the polarizing beamsplitter, which connects excitation and detection path, and is directed through a quarter waveplate and the cryostat window down the stick. At the lens at the bottom on the stick it is focused onto to sample. A part of the emitted light from the sample is directed through the lens up the stick towards the optical head. After passing the cryo window and quarter waveplate the signal is reflected and transmitted 50/50 at the polarizing beamsplitter. The residual excitation laser that is reflected from the sample surface is now reflected at the polarizing beamsplitter. The detection signal now passes an additional adjustable polarizer, increasing the suppression of the residual excitation light. Finally, it is coupled into a polarization-maintaining fiber and sent to the optical table for spectral or temporal analysis. The coupling into the single-mode fiber acts as an additional filter, as the intensity of the suppressed laser is distributed in a cloverleaf-like shape around the center of the detection signal in cross section [198]. The suppression of the excitation laser in the detection signal is crucial for any applications and experiment relying on single photons, and can be optimized by adjustment of the two polarizers, the quarter waveplate in the optical path, and

the focus. The polarizer in the excitation optimizes the polarization of the excitation light to match the polarizing beamsplitter, while the polarizer in the detection path enhanced the filtering effect of the polarizing beamsplitter in transmission. The quarter waveplate accounts for elliptical parts in light originating from birefringence of the sample and imperfections of the optics. Overall, a suppression of down to 10^{-8} can be achieved.
While the resonance fluorescence setup is optimized to resonant excitation of single QDs, it is not necessarily limited with respect to other applications. Near-resonant and off-resonant excitation, for example excitation with a 850 nm laser diode for characterization of single QDs works equally well. The replacement of the polarizing beamsplitter with a non-polarizing one and exchange or removal of the other optical elements allows for polarization-resolved measurements or measurements relying solely on spectral filtering.

A.3 Generation of a fully customized excitation pulses

A.3.1 4f pulseshaping

The folded 4f pulseshaper is an essential element in the excitation within this work. The basic principle is sketched in Figure A.3a. An incident spectrally broad pulse with 150 fs duration is reflected off a D-shaped mirror and dispersed on a diffraction grating with 1800 lines/mm. The light is then collimated in the horizontal plane on a lens with 300 mm focal length which is positioned in this same distance with respect to the grating. Thereby the individual frequencies are focused on a combination of a slit and mirror. A small vertical angle in the beam path is induced through a vertical offset of the lens with respect to the beam. For precise adjustment of the position and the focal point and thereby minimize the chip in the frequency components of the pulse, the lens is positioned on a manual linear translation stage. The slit is tunable in position and width by being mounted on a linear translation stage and through a manual micrometer-screw. This filtering in the Fourier-plane enables precise control of the spectral width of the output pulse, i.e. the part of the input pulse that is reflected on the mirror behind the slit, and thus also the pulse duration in time. The center frequency of the output pulse is adjustable by the position of slit with help of the stage. The output pulse passes the lens on slightly higher position, parallelizing it again with respect to the table, and after passing the grating, the light is collimated and passes over the D-shaped mirror for further processing and use.
With help of an APE Pulse Check autocorrelator, the temporal duration of the pulse depending on the width of the slit can be analyzed as shown in Figure A.3b. Pulse

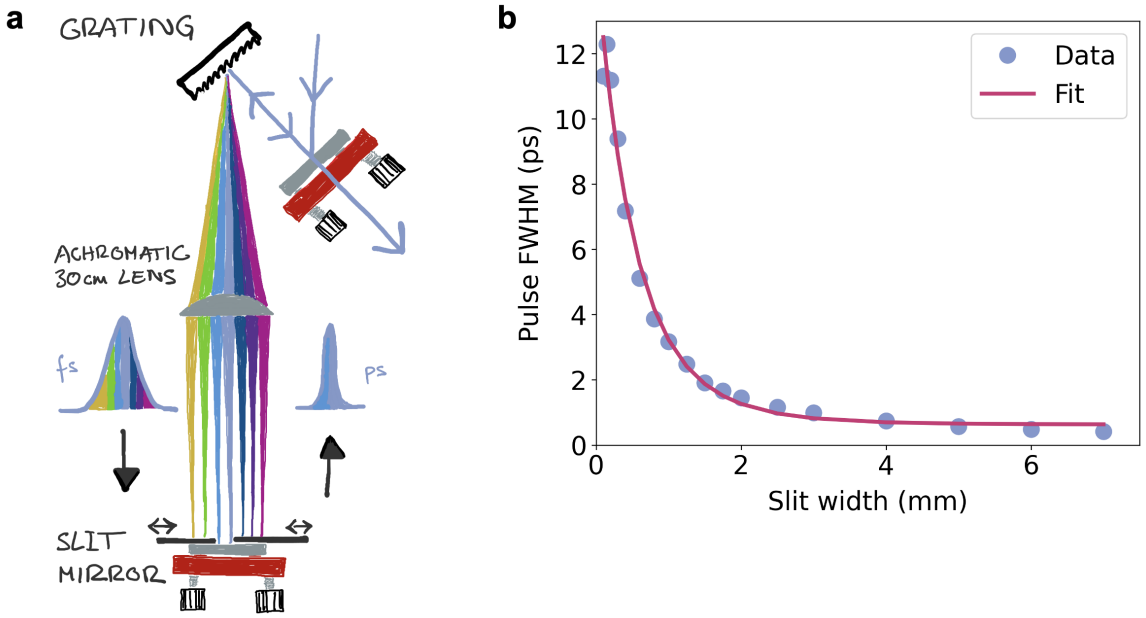

Figure A.3 | Folded 4f pulseshaper. **a**, Sketch of the optical setup of a folded pulseshaper. The incident $150\,\mathrm{fs}$ pulse is dispersed on a grating and each wavelength is focused through a lens on a different point on a combination of a slit and a mirror. The slit can be varied in width and position, allowing for selection of spectral width and center frequency. The reflected pulse with smaller spectral width passes the lens and grating, where the beam collimates again. A difference in height allows for separation of incident and outgoing pulses. **b**, The pulse duration in FWHM of intensity as a function of slit width, follows a hyperbolic function. The pulse length can be varied from about 0.5 to $12\,\mathrm{ps}$ in our setup.

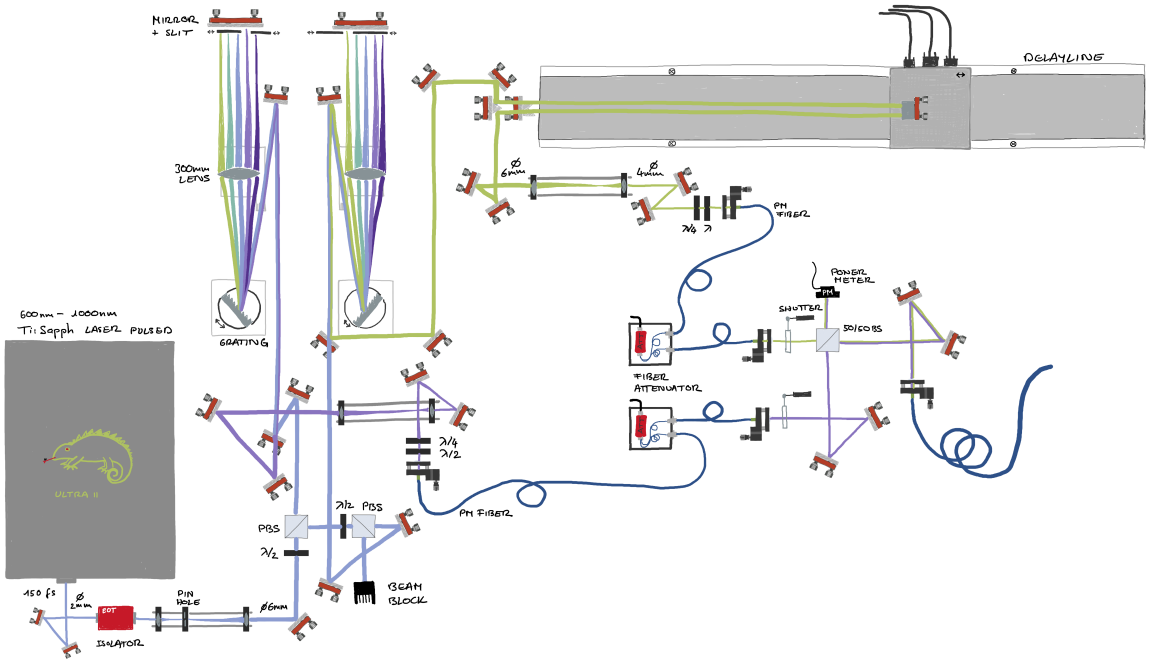

Figure A.4 | Pulseshaper setup. The 150 fs pulses of a Coherent Chameleon Ultra II are split up into two separate paths with adjustable intensity. Each of the two pulses are sent over separate 4f pulseshapers for individual choice of pulse length and center frequency. The first pulse is coupled into a PM single mode fiber, while the second pulse is sent over a delayline with adjustable delay with up to 4 m before being coupled into a PM single mode fiber as well. The intensity of both pulses is adjustable with individual fiber attenuators, before both pulses are combined in a free-space setup to a single optical path. This configuration allows for full control over pulse shape, frequency and timing.

durations between 12 ps and 0.5 ps can be generated from the 150 fs input pulse. Note that dispersion in the optical fibers becomes non-negligible below 2 ps pulse durations, limiting the use of shorter pulses in our setup.

A.3.2 Pulseshaper setup

The pulseshaper setup is used to generate two fully independent and customizable excitation pulses in the picosecond range with adjustable delay in time. To this end, the 150 fs pulses of a Chameleon Ultra II Ti:Sapph laser with repetition rate of 80 MHz are used as the input. The laser itself, based on a cavity system, is tunable from 680 nm to 1080 nm with output power up to 4 W. The optical setup is optimized to a wavelength of 920 nm. The input laser pulse passes a Faraday isolator and is then increased in diameter to 6 mm for minimal divergence in a 2-lens telescope configuration. A pellicle in the focus point ensures a clean beam profile. The pulse is then divided into three separate arms with variable intensity. Two of the paths are send to separate folded 4f pulse shapers as explained in the previous section, whereas

the third path ends in a beam block. After generation of the picosecond pulses with adjustable duration and center frequency, the first beam is reduced in diameter to 4 mm and after polarization control with a quarter and half waveplate coupled into a polarization maintaining fiber. The second pulse path is re-directed after the pulse shaper to a 1 m delayline. In a configuration of two hollow roof mirrors facing each other but rotated with respect to each other by 90deg, where one of them is mounted on the stage of the delayline, and one razor edge triangle mirror behind and above the other hollow roof mirror, the light passes the stage on the delayline twice with no angle displacement. For details on this mirror configuration and reduction of beam path displacement with translation of the stage see Ref. [199]. Passing the delayline twice gives a maximum of 4 m in adjustable path difference which allows us to fully cover the time separation between to consecutive pulses in pulse delay. After being delayed, the beam diameter is reduced to 4 mm in a configuration of two chromatic lenses, the polarization is adjusted with waveplates and the light is coupled into a second polarization-maintaining fiber. Both fibers are coupled to individual voltage-controlled Thorlabs fiber-attenuators for intensity control, and are then out-coupled to a second free-space setup. Here both pulses are combined with a 50/50 beamsplitter and coupled into a final polarization-maintaining fiber. Optical shutters in each of the two paths in this setup allow for selection of individual paths, while a powermeter at the other beamsplitter output allows for intensity-readout. The excitation pulses are then sent through the optical fiber to the resonance fluorescence setup.

A.4 Setups for time-resolved correlation analysis

A.4.1 Hanbury-Brown-Twiss setup

To analyze the single-photon purity, we approximate the second order coherence function in a Hanbury-Brown-Twiss setup [174] experimentally which is sketched in Figure A.5. The signal to be analyzed is split up into two paths by a non-polarizing 50/50 beamsplitter. Each path is then coupled into a polarization-maintaining fiber with help of two mirrors and lenses before the fiber tips. Each fiber directs the light to a SPADs, where each incident photon is converted into an electrical pulse, with a efficiency of about 0.37 at 920 nm. The signal of both SPADs is sent to a quTAG timing correlator where each electrical pulse is attributed a time stamp. Both arms of the detection signal are then correlated in time. For perfect detectors and an optimal single-photon source with only one photon emitted at a time, the two detectors can never 'click' at the same time, as a single photon in projected to either one of the two paths upon detection.

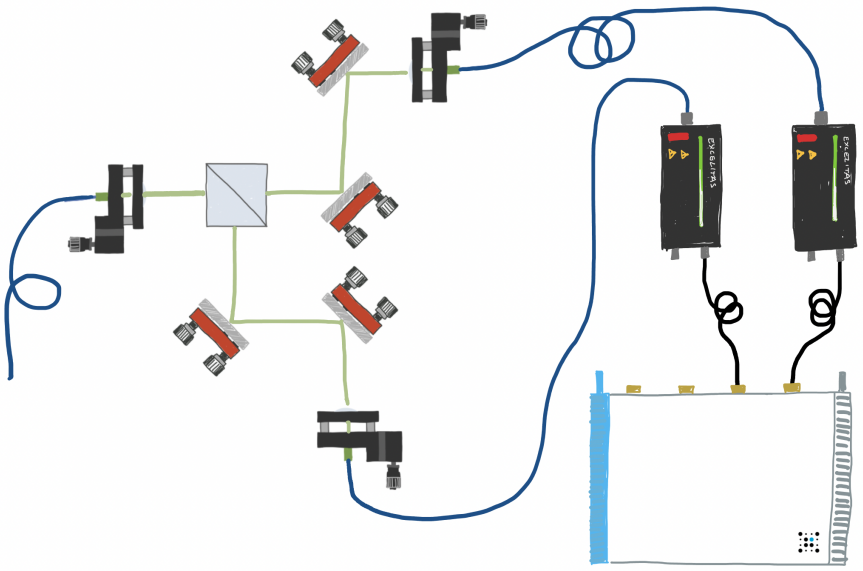

Figure A.5 | Hanbury-Brown-Twiss setup. The second order coherence function of the QD emission is estimated by splitting the signal into two paths via a 50/50 beamsplitter and measuring the correlations between the two arms. Here, both are coupled into PM single-mode fibers again and send to two individual SPADs which convert the incident photons to electrical pulses. These are sent to a quTAG timing correlator where both inputs are correlated with each other in time.

A.4.2 Unbalanced Mach-Zehnder interferometer

For indistinguishability measurements, we detect and evaluate correlations from the detection signal passing an unbalanced Mach-Zehnder interferometer.
To minimize the impact of charge noise on the result [200] of the indistinguishability measurements, the excitation pulse repetition rate is first doubled, creating two subsequent pulses with a separation of 3.3 ns, as shown in Figure A.6a. After being customized in the pulseshaper setup, the laser pulse is split up into two parts, where one is delayed by 3.3 ns. The two mirrors re-direct the delayed pulse back to another beamsplitter, where both pulses are combined The mirrors are mounted on a translation stage which allows for precise control of the pulse separation in time. Both pulses are then coupled into a polarization-maintaining fiber and sent to the resonance fluorescence setup. Note that for swing-up excitation, the combination of the two swing-up pulses is doubled in repetition rate and delayed in time, resulting in 4 pulses which are directed to the sample for excitation.
To evaluate the indistinguishability of the emitted photons, the detection signal is coupled to the unbalanced Mach-Zehnder interferometer as sketched in Figure A.6b. As only single photons are emitted at a time, subsequent photons need to be overlayed with each other on a beamsplitter. To this end, the detection signal is split up into two paths, where one is delayed by 3.3 ns, to match the separation of the two adjacent

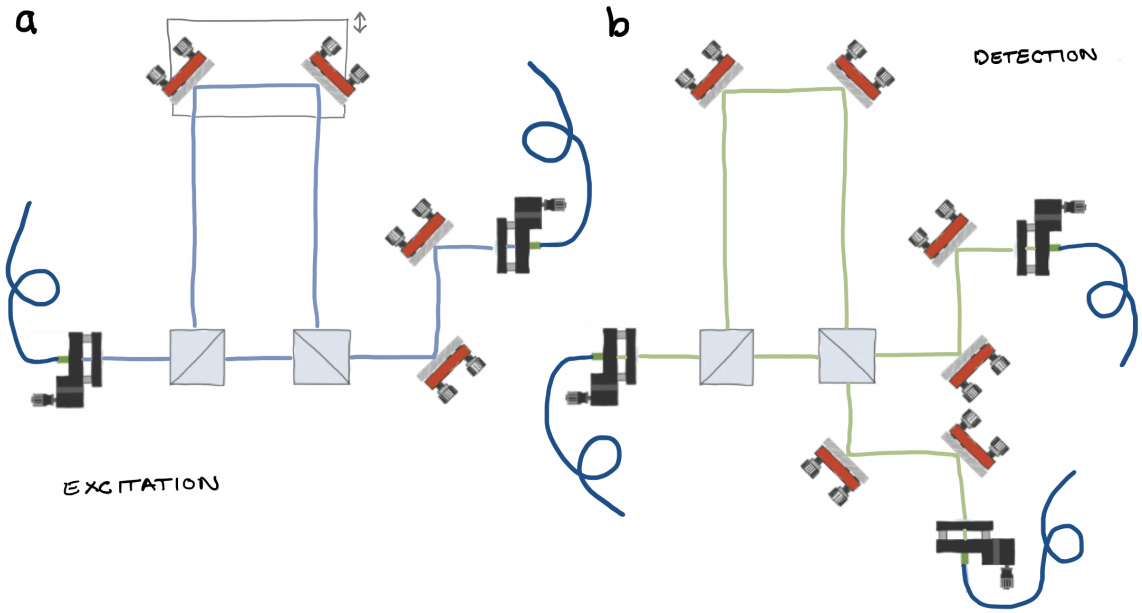

Figure A.6 | Unbalanced Mach-Zehnder interferometer with excitation pulse preparation. **a**, The initial pulse is split into two via beamsplitter 1 and one arm is delayed by $3\,\mathrm{ns}$ with respect to the other. Both are then combined to the same optical path on beamsplitter 2 and coupled into a fiber. This doubled the repetition rate of the laser and introduces two pulses separated by $3.3\,\mathrm{ns}$. **b**, For indistinguishability measurements of subsequent photons, the emitted signal is split by a beamsplitter where one arm is delayed to match the temporal distance of the photons. Photons of the two paths are interfered on a second beamsplitter, where due to the HOM effect two identical photons are always projected on either one of the outputs upon measurement. The signal of the to output arms of beamsplitter 2 are then correlated in time in analogy to the HBT measurement.

laser pulses. Both are then interfered on a second beamsplitter. For two identical photons, as explained in Chapter 4, following the HOM effect [166], they only leave the beamsplitter together at either one of the outputs. A correlation of the two output paths, in analogy to the HBT experiment, then allows for analysis of the indistinguishability. As both photons are only overlayed in time if the first photon is reflected on the first beamsplitter and the second is transmitted, both probabilistic events with a 50/50 chance, several peaks occur in the time-resolved correlation histogram. However, at zero time delay, only two photons which are overlayed in time, but are not indistinguishable can be correlated, while the directly neighboring peaks are delayed by the separation of the laser pulses and correspond to both photons being transmitted or reflected on the first beamsplitter. They don't interfere on the second beamsplitter and thus their integrated intensity can be used for normalization.

Appendix B

Supplemental simulations and analysis

This chapter includes material from

Katarina Boos*, Friedrich Sbresny*, Sang Kyu Kim*, Malte Kremser, Hubert Riedl, Frederik W. Bopp, William Rauhaus, Bianca Scaparra, Klaus Jöns, Jonathan J. Finley, Kai Müller, and Lukas Hanschke,
Coherent Swing-Up Excitation for Semiconductor Quantum Dots, Advanced Quantum Technologies 2300359 (2024)
https://doi.org/10.1002/qute.202300359

Contents

In this appendix, we discuss additional simulations, experimental results and analysis details for results presented in the main manuscript. As a start, supplemental simulations showing the full resonance spectra are presented, for varying excitation parameter series with increasing pulse intensity, time delay and detuning. Furthermore,

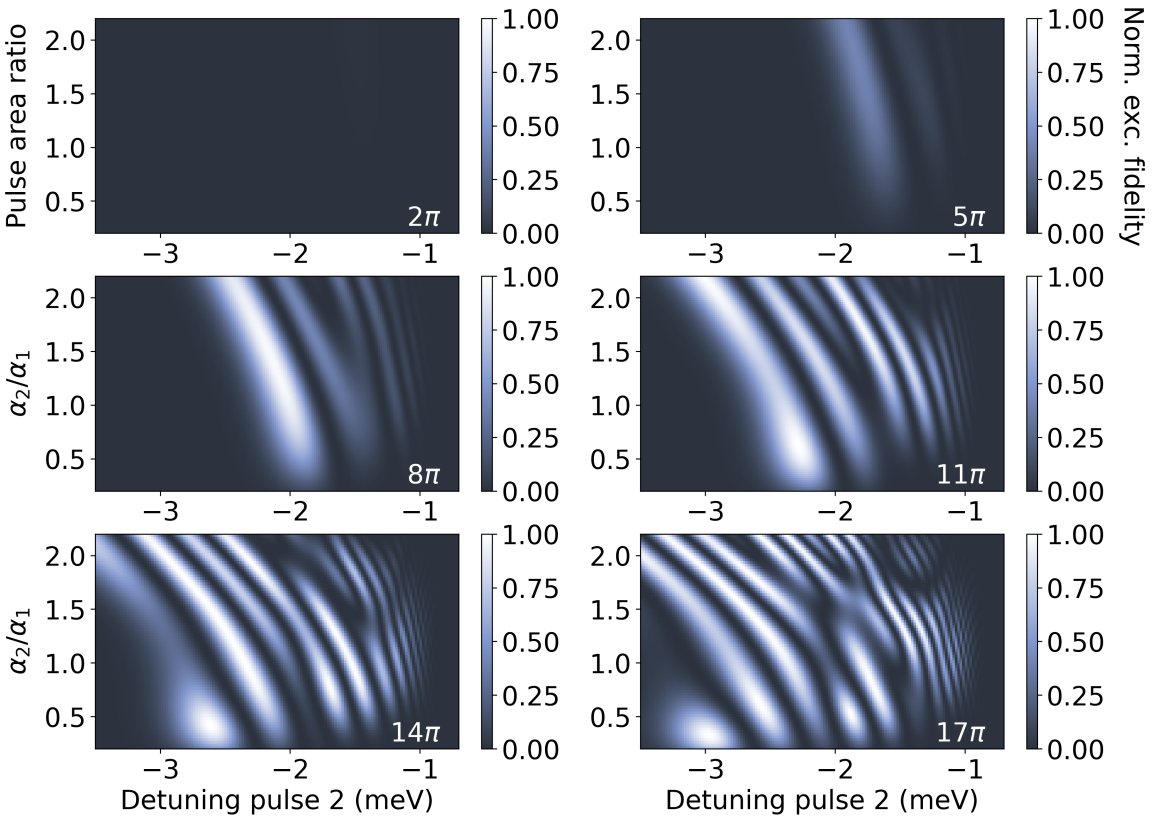

Figure B.1 | Full simulation series for increasing pulse area. The pulse intensity of the first laser is increased from 2π to 17π from panel to panel, while in each one the second laser pulse is scanned in area and detuning to resolve resonances and characterize the excitation scheme for the specific pulse 1 area. Overall, the pulse lengths and the detuning of the first pulse were kept constant at $10\,\mathrm{ps}$ and $-0.7\,\mathrm{meV}$, respectively. Below $\alpha_1 = 8\pi$ efficient excitation is not possible for the fixed detuning, while above it with increasing pulse area the resonance lines become more complex.

we show experimental spectra exhibiting broadening under two-photon excitation and phonon-assisted excitation for increasing excitation power. Finally, we explain the analysis of the correlation measurements, both for the value of second order coherence at zero time delay and the degree of indistinguishability of the emitted photons.

B.1 Supplemental simulations

B.1.1 Full simulation of power-dependent series

The full simulations for the power-dependent swing-up excitation fidelity and resonances are presented in Figure B.1. Between the different subgraphs, the intensity of the first pulse is stepwise increased from $\alpha_1 = 2\pi$ to 17π, while in each individual subgraph the detuning and intensity of the second laser pulse is scanned from $\Delta_2 = -3.5\,\mathrm{meV}$ to

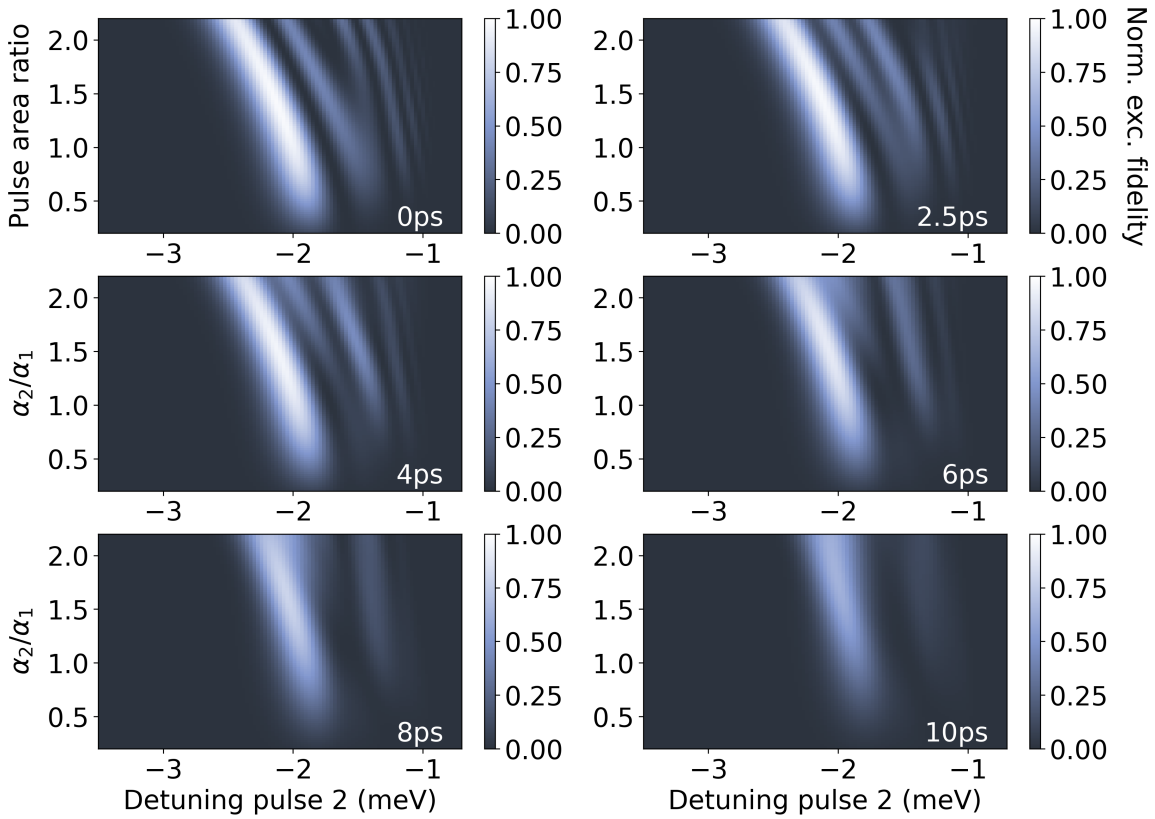

Figure B.2 | Study of the impact of the time delay on the swing-up excitation scheme in simulation. The delay between pulse 1 and pulse 2 was increased from 0 ps to 10 ps, while the other pulse parameters of the first pulse were kept constant at $\Delta_2 = -0.7\,\mathrm{meV}$ and $\alpha_1 = 8\pi$. The detuning and intensity of the second excitation pulse was scanned for resonances and optimal excitation. With increasing time delay, the efficiency of the schemes drops, while the position of the resonances changes only slightly.

$-0.7\,\mathrm{meV}$ and $\alpha_2/\alpha_1 = 0.2$ to 2.2, respectively. The detuning of the first pulse was kept constant at $\Delta_1 = -0.7\,\mathrm{meV}$, and the pulse length of both pulses with 10 ps, and the pulse separation with zero delay were not changed. The intensity in each subgraph corresponds to the upper state population after interaction of the QD with the two pulses. The scales are normalized from 0 to 1. The points of maximal population inversion for each first pulse intensity are presented in Chapter 4. As discussed in the main text, with increasing first pulse area, the resonance lines become more complex, while with decreasing pulse intensity below 8π the efficiency of the swing-up excitation decreases if keeping the detuning constant.

B.1.2 Full simulation series for increasing time delay

In Figure B.1 we present the full simulation graphs for the impact of time delay between the two swing-up pulses. The time delay is varied from 0 to 10 ps which

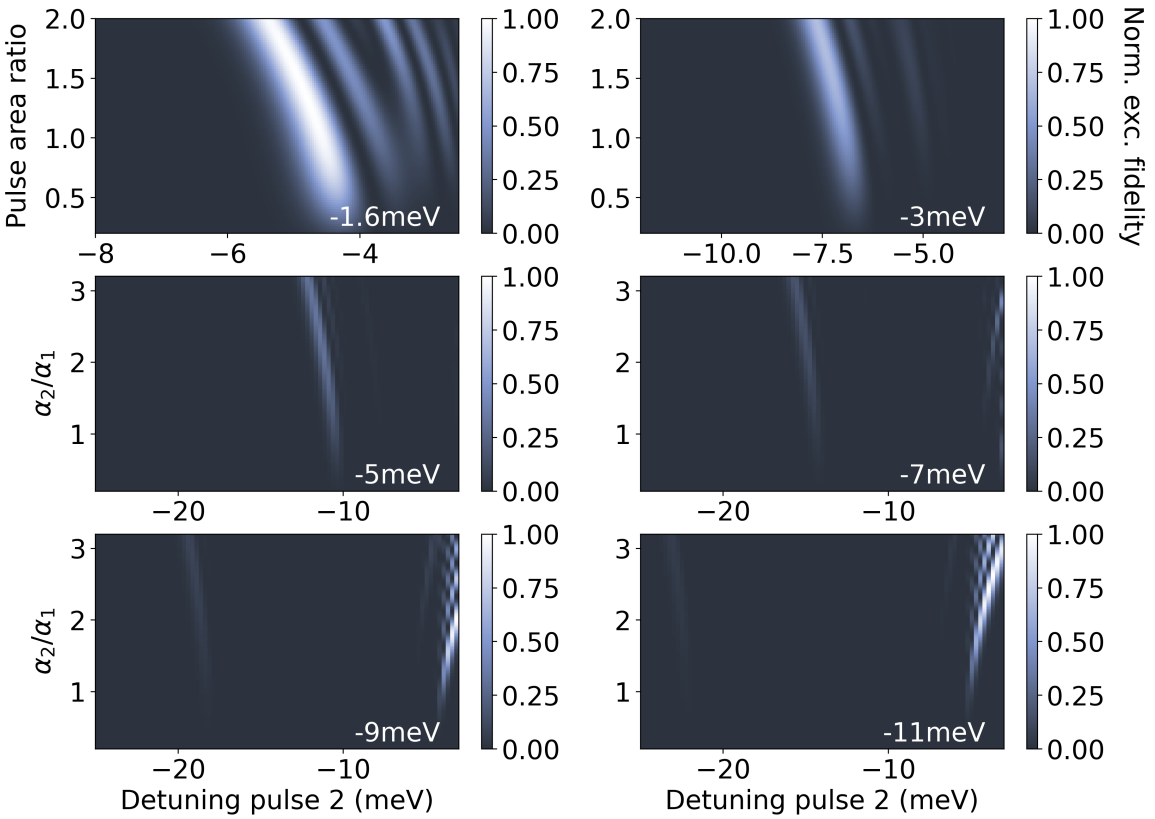

Figure B.3 | Full two-dimensional scans for the simulation series of increasing detuning of the first laser. The detuning Δ_1 is varied from $-1.6\,\mathrm{meV}$ to $-11\,\mathrm{meV}$ while both pulse lengths are kept fixed at $5\,\mathrm{ps}$ and the intensity of the first pulse remains at 9π. Both detuning and intensity of the second pulse were scanned for each detuning of the first pulse to characterize the resonance spectra. With increasing detuning the point of maximal inversion efficiency shifts to higher detuning and higher intensity for the fixes pulse 1 intensity.

corresponds to almost a full separation. The pulse lengths of 10 ps and the detuning Δ_1 and intensity α_1 of the first pulse with $\Delta_1 = -0.7\,\mathrm{meV}$ and $\alpha_1 = 8\pi$ were not changed between the different time delays. Same as for varying first pulse intensity, in each subgraph the detuning Δ_2 and intensity α_2 of the second pulse were scanned to find resonances and study the inversion efficiency. The color represents the population of the excited state after light-matter interaction, on a scale from 0 to 1. The efficiency decreases only with significant delay between the pulses, while the position of the resonances varies only minimally. A detailed analysis and discussion of the effect and sensitivity of the swing-up excitation fidelity and resonances to the time delay are provided in Chapter 4.

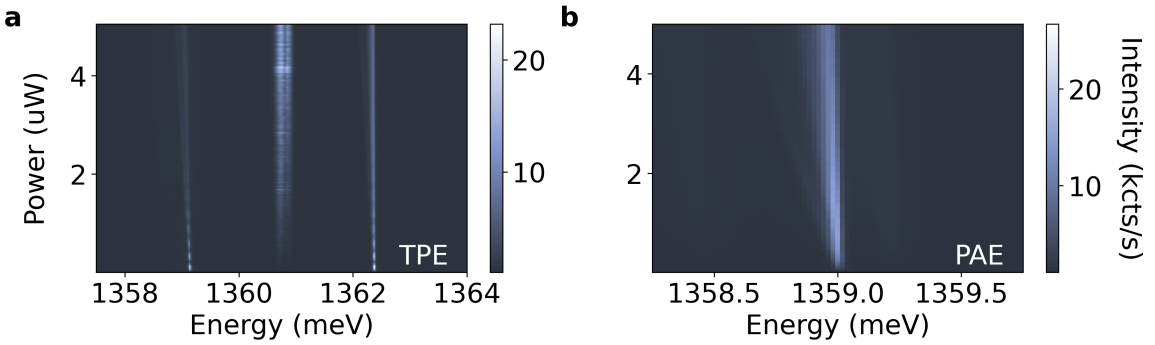

Figure B.4 | Alternative excitation methods using high excitation power. **a**, Two-photon excitation of the biexciton, resulting in the cascaded decay via the neutral exciton to the crystal ground state, visible as the lower and higher energy emission line. Following Rabi rotations with increasing excitation intensity, the emission lines broaden and red-shift. The excitation laser is visible as the center peak. **b**, Emission of the negatively charged trion under phonon-assisted excitation broadens and red-shifts with increasing excitation power, consistent with swing-up and two-photon excitation.

B.1.3 Full simulation series for detuning-dependence

Here, we present the full simulations for swing-up excitation fidelity and resonances for varying detuning Δ_1 of the first pulse that are summarized, analyzed and discussed in Chapter 4. The detuning of swing-up pulse 1 is decreased from $\Delta_1 = -1.6\,\text{meV}$ to $-11\,\text{meV}$. The pulse durations are kept constant at 5 ps, the intensity of pulse 1 is kept at $\alpha = 9\pi$. In analogy to before, the detuning Δ_2 and pulse intensity α_2 of the second pulse are scanned, while the intensity in each subgraph corresponds to the calculated upper-state population after interaction of the swing-up pulse with the TLS. Note that the scaling with respect to detuning and intensity of the second laser pulse varies between the panels. With increasing absolute detuning and fixed intensity of the first pulse, the resonance with maximal population inversion shifts towards larger detuning and higher intensity of the second pulse. The bright resonances at smaller negative detuning appearing from $\Delta_1 = -7\,\text{meV}$ to $-11\,\text{meV}$ are neglected in our analysis as they correspond to the case of swapped first and second laser pulse in detuning.

B.2 Broadening under alternative excitation methods

To confirm that the broadening and spectral shift of the emission peak under swing-up excitation originates from spectral diffusion and dephasing under high excitation powers and is not inherent to the excitation method itself, here we look at emission under alternative excitation techniques with similar high excitation intensity (Figure B.4). In particular, we investigate the power-dependent emission of the biexciton $2X$ and neutral exciton X^0 under two-photon excitation (TPE) in Figure B.4a and the emission

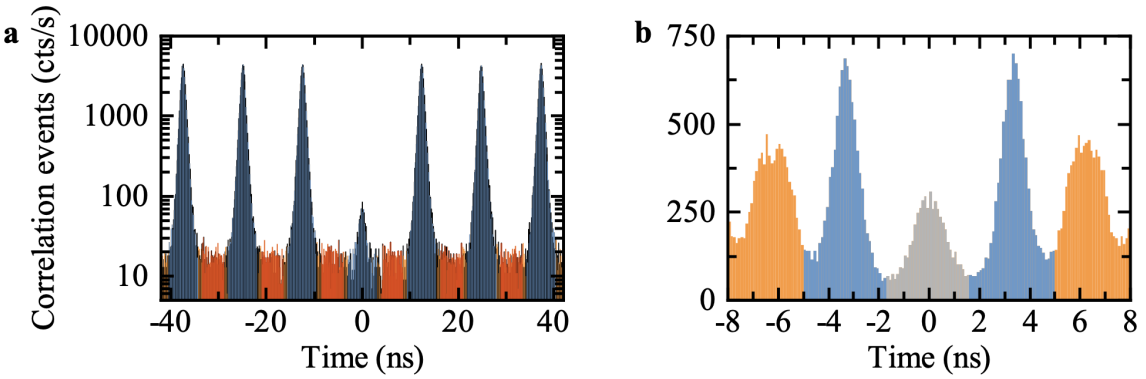

Figure B.5 | Peak integration regions for correlations analysis. **a**, Exemplary $g^2(\tau)$ measurement with colored regions that are used as integrated counts (blue) with a width of 6 ns and background (red) and are neglected (orange). **b**, A similar approach is used for indistinguishability measurements. The grey area marks the center peak, the neighboring peaks the intensity is normalized to, is marked in blue, while the orange region is not of interest. Here, all three integration regions are chosen to have the same width.

of the neutral exciton X^- with phonon-assisted excitation (PAE) in Figure B.4b. Both excitation methods are non-resonant, facilitating the observation of the QD emission peaks for high excitation powers, as the excitation laser is spectrally separated and does not induce noise at the emission peak frequencies at high intensity. The excitation of the biexciton via two photons is a coherent process, thus Rabi rotation in both the exciton and biexciton emission, visible at the left and the right of the laser energy in the spectra, are clearly visible. For higher intensity, up to 4.5 µW, decoherence causes a reduction of the Rabi rotations, while the emission lines both clearly red-shift and broaden. The same trend can be seen for emission under phonon-assisted excitation with increasing excitation power up to 4.5 µW. As similar excitation intensities were used in swing-up excitation, we attribute this effect to spectral diffusion and dephasing caused by the high intensities in our sample. Most likely, laser-generated charge carriers are trapped in the metal-semiconductor interface of the Schottky diode.

B.3 Correlation analysis and error estimation

For analysis of the single-photon purity from the correlation histograms as presented in Chapter 4, the center peak at zero time delay needs to be compared to the neighboring peaks with respect to integrated intensity. To this end, the raw data are integrated in bins of 100 ps width, as shown in Figure B.5a in dependence of time, exemplarily shown for the data for swing-up excitation. The peaks are integrated in time windows of 6 ns, marked in blue, to ensure capturing all emission while minimizing the contribution of background counts. The raw value of the second order correlation

function at zero time delay $g^{(2)}(0)_{\mathrm{raw}}$ is obtained by normalizing the integrated center peak to the average sidepeak area. Here, six sidepeaks are taken into account. For error estimation we assume Poissonian noise and thus describe it by the standard error $\mathrm{error}_{\mathrm{raw}} = \mathrm{A}_{\mathrm{center,raw}}^{-1/2} \times g^{(2)}{}_{\mathrm{raw}}$. Here, $\mathrm{A}_{\mathrm{center,raw}}$ is the integrated intensity of the center peak. To account for the contribution of the background, a region in-between the peaks with 4.5 ns width, marked in red, is averaged in subtracted from the center, as well as the sidepeaks. This gives us the background-corrected value for the single-photon purity. The error estimation for the background-subtracted value is based on the center peak area with included background giving $\mathrm{error}_{\mathrm{corr}} = \frac{\mathrm{A}_{\mathrm{center,raw}}}{\mathrm{A}^2_{\mathrm{avg.neighbor,raw}}}$.

For the indistinguishability measurements, as presented in Figure B.5b for emission under swing-up excitation, the pulse separation was adjusted to 3.3 ns as explained in relation to the unbalanced Mach-Zehnder setup. In analogy to the second order correlation data, the raw data is integrated into bins of 100 ps, as shown in the figure, and data containing the center peak (grey) and the first two sidepeaks (blue) is separated into equal time windows. The HOM visibility is then given by $v_{\mathrm{HOM}} = 1 - \frac{2\mathrm{A}_{\mathrm{center}}}{\mathrm{A}_{\mathrm{left}}+\mathrm{A}_{\mathrm{right}}}$ Assuming Poissonian noise statistics and considering the SPAD timing-jitter of 300 ps, the error can be estimated by adding and subtracting ± 150 ps to the integration windows.

Bibliography

[1] Mandel, L. and Wolf, E. *Optical Coherence and Quantum Optics* (Cambridge University Press, 1995). (Cited on page 1.)

[2] Loudon, R. *The quantum theory of light* (Oxford University Press, 2000). (Cited on pages 1 and 16.)

[3] Scully, M.O. and Zubairy, M.S. *Quantum optics* (Cambridge University Press, 1997). (Cited on pages 1, 16, 18, and 22.)

[4] Planck, M. Über das gesetz der energieverteilung im normalspectrum. *Annalen der Physik* **4**, 553–563 (1901). (Cited on page 1.)

[5] Planck, M. The nobel prize in physics 1918: in recognition of the services he rendered to the advancement of physics by his discovery of energy quanta. https://www.nobelprize.org/prizes/physics/1918/summary/ (1918). (Cited on page 1.)

[6] Einstein, A. Über einen die erzeugung und verwandlung des lichtes betreffenden heuristischen gesichtspunkt (1905). (Cited on page 1.)

[7] Einstein, A. The nobel prize in physics 1921: for his services to theoretical physics, and especially for his discovery of the law of the photoelectric effect. https://www.nobelprize.org/prizes/physics/1921/summary/ (1921). (Cited on page 1.)

[8] Aspect, A., Dalibard, J., and Roger, G. Experimental test of bell's inequalities using time-varying analyzers. *Physical Review Letters* **49**, 1804–1807 (1982). URL https://doi.org/10.1103/PhysRevLett.49.1804. (Cited on page 1.)

[9] Aspect, A., Clauser, J., and Zeilinger, A. The nobel prize in physics 2022: for experiments with entangled photons, establishing the violation of bell inequalities

and pioneering quantum information science. https://www.nobelprize.org/prizes/physics/2022/summary/ (2022). (Cited on page 1.)

[10] Bennett, C.H., Brassard, G., Crépeau, C., Jozsa, R., Peres, A., and Wootters, W.K. Teleporting an unknown quantum state via dual classical and einstein-podolsky-rosen channels. *Physical Review Letters* **70**, 1895–1899 (1993). URL https://link.aps.org/doi/10.1103/PhysRevLett.70.1895. (Cited on page 1.)

[11] Bouwmeester, D., Pan, J.W., Mattle, K., Eibl, M., Weinfurter, H., and Zeilinger, A. Experimental quantum teleportation. *Nature* **390**, 575–579 (1997). URL https://doi.org/10.1038/37539. (Cited on page 1.)

[12] Mollow, B.R. Power spectrum of light scattered by two-level systems. *Physical Review* **188**, 1969–1975 (1969). URL https://link.aps.org/doi/10.1103/PhysRev.188.1969. (Cited on pages 1, 2, 15, 22, and 23.)

[13] Dirac, P.A.M. The quantum theory of the emission and absorption of radiation. *Proceedings of the Royal Society of London. Series A, Containing Papers of a Mathematical and Physical Character* **114**, 243–265 (1927). URL https://doi.org/10.1098/rspa.1927.0039. (Cited on page 1.)

[14] Weisskopf, V. Zur theorie der resonanzfluoreszenz. *Annalen der Physik* **401**, 23–66 (1931). URL https://doi.org/10.1002/andp.19314010103. (Cited on page 1.)

[15] Heitler, W. *The Quantum Theory of Radiation*, vol. 5 of *International Series of Monographs on Physics* (Oxford University Press, Oxford, 1936). (Cited on page 1.)

[16] Muller, A., Flagg, E.B., Bianucci, P., Wang, X.Y., Deppe, D.G., Ma, W., Zhang, J., Salamo, G.J., Xiao, M., and Shih, C.K. Resonance fluorescence from a coherently driven semiconductor quantum dot in a cavity. *Physical Review Letters* **99**, 187402 (2007). URL https://link.aps.org/doi/10.1103/PhysRevLett.99.187402. (Cited on pages 1, 2, 37, and 38.)

[17] Nick Vamivakas, A., Zhao, Y., Lu, C.Y., and Atatüre, M. Spin-resolved quantum-dot resonance fluorescence. *Nature Physics* **5**, 198–202 (2009). URL https://doi.org/10.1038/nphys1182. (Cited on pages 1, 2, 15, 19, 23, 31, 38, and 67.)

[18] Matthiesen, C., Vamivakas, A.N., and Atatüre, M. Subnatural linewidth single photons from a quantum dot. *Physical Review Letters* **108**, 093602 (2012). URL

https://link.aps.org/doi/10.1103/PhysRevLett.108.093602. (Cited on page 1.)

[19] Prechtel, J.H., Kuhlmann, A.V., Houel, J., Greuter, L., Ludwig, A., Reuter, D., Wieck, A.D., and Warburton, R.J. Frequency-stabilized source of single photons from a solid-state qubit. *Physical Review X* **3**, 041006 (2013). URL https://link.aps.org/doi/10.1103/PhysRevX.3.041006. (Cited on page 1.)

[20] Tomm, N., Mahmoodian, S., Antoniadis, N.O., Schott, R., Valentin, S.R., Wieck, A.D., Ludwig, A., Javadi, A., and Warburton, R.J. Photon bound state dynamics from a single artificial atom. *Nature Physics* 1–6 (2023). URL https://doi.org/10.1038/s41567-023-01997-6. (Cited on page 1.)

[21] Kimble, H.J. and Mandel, L. Theory of resonance fluorescence. *Physical Review A* **13**, 2123–2144 (1976). URL https://link.aps.org/doi/10.1103/PhysRevA.13.2123. (Cited on page 1.)

[22] Kimble, H.J., Dagenais, M., and Mandel, L. Photon antibunching in resonance fluorescence. *Physical Review Letters* **39**, 691–695 (1977). URL https://link.aps.org/doi/10.1103/PhysRevLett.39.691. (Cited on page 1.)

[23] Dicke, R.H. Coherence in spontaneous radiation processes. *Physical Review* **93**, 99–110 (1954). URL https://link.aps.org/doi/10.1103/PhysRev.93.99. (Cited on page 1.)

[24] Origin of antibunching in resonance fluorescence. *Physical Review Letters* **125**, 170402 (2020). URL https://link.aps.org/doi/10.1103/PhysRevLett.125.170402. (Cited on page 1.)

[25] Arimondo, E., Bjoerk, C.J., and Walther, H. Observation of ramsey fringes in a coherent beam of na atoms. *Physical Review Letters* **37**, 1031–1034 (1976). (Cited on page 1.)

[26] Arimondo, E. V coherent population trapping in laser spectroscopy. In *Progress in Optics*, vol. 35, 257–354 (Elsevier, 1996). (Cited on page 1.)

[27] Ulhaq, A., Weiler, S., Ulrich, S.M., Roßbach, R., Jetter, M., and Michler, P. Cascaded single-photon emission from the mollow triplet sidebands of a quantum dot. *Nature Photonics* **6**, 238–242 (2012). URL https://doi.org/10.1038/nphoton.2012.23. (Cited on pages 2, 15, 23, and 31.)

[28] Ulhaq, A., Weiler, S., Roy, C., Ulrich, S.M., Jetter, M., Hughes, S., and Michler, P. Detuning-dependent mollow triplet of a coherently-driven single quantum

dot. *Optics Express* **21**, 4382–4395 (2013). URL https://opg.optica.org/oe/abstract.cfm?URI=oe-21-4-4382. (Cited on pages 2, 15, 23, and 31.)

[29] Reiter, D.E. Time-resolved pump-probe signals of a continuously driven quantum dot affected by phonons. *Physical Review B* **95**, 125308 (2017). URL https://link.aps.org/doi/10.1103/PhysRevB.95.125308. (Cited on pages 2, 15, and 23.)

[30] Gustin, C., Hanschke, L., Boos, K., Müller, J.R.A., Kremser, M., Finley, J.J., Hughes, S., and Müller, K. High-resolution spectroscopy of a quantum dot driven bichromatically by two strong coherent fields. *Physical Review Research* **3**, 013044 (2021). URL https://link.aps.org/doi/10.1103/PhysRevResearch.3.013044. (Cited on pages 2, 15, and 23.)

[31] Ramsay, A. A review of the coherent optical control of the exciton and spin states of semiconductor quantum dots. *Semiconductor Science and Technology* **25**, 103001 (2010). URL https://dx.doi.org/10.1088/0268-1242/25/10/103001. (Cited on pages 2, 15, 19, and 23.)

[32] Rzazewski, K. and Florjanczyk, M. The resonance fluorescence of a two-level system driven by a smooth pulse. *Journal of Physics B: Atomic, Molecular and Optical Physics* **17**, L509 (1984). URL https://dx.doi.org/10.1088/0022-3700/17/15/005. (Cited on pages 2, 16, 23, 25, 33, and 58.)

[33] Florjaczyk, M., Rzazewsk, K., and Zakrzewski, J. Resonance scattering of a short laser pulse on a two-level system: Time-dependent approach. *Physical Review A* **31**, 1558–1562 (1985). URL https://link.aps.org/doi/10.1103/PhysRevA.31.1558. (Cited on pages 2, 16, 23, 25, 26, 30, 33, 58, and 59.)

[34] Lewenstein, M., Zakrzewski, J., and Rzazewski, K. Theory of fluorescence spectra induced by short laser pulses. *Journal of the Optical Society of America B* **3**, 22–35 (1986). URL https://opg.optica.org/josab/abstract.cfm?URI=josab-3-1-22. (Cited on pages 2, 16, and 23.)

[35] Buffa, R., Cavalieri, S., Fini, L., and Matera, M. Resonance fluorescence of a two-level atom driven by a short laser pulse: extension to the off-resonance excitation. *Journal of Physics B: Atomic, Molecular and Optical Physics* **21**, 239 (1988). URL https://dx.doi.org/10.1088/0953-4075/21/2/008. (Cited on pages 2, 16, 23, and 26.)

[36] Rodgers, P. and Swain, S. Multi-peaked resonance fluorescence spectra with rectangular laser pulses. *Optics Communications* **81**, 291–296 (1991). URL https://

www.sciencedirect.com/science/article/pii/003040189190618N. (Cited on pages 2, 16, 23, 25, and 26.)

[37] Moelbjerg, A., Kaer, P., Lorke, M., and Mørk, J. Resonance fluorescence from semiconductor quantum dots: Beyond the mollow triplet. *Physical Review Letters* **108**, 017401 (2012). URL https://link.aps.org/doi/10.1103/PhysRevLett.108.017401. (Cited on pages 2, 16, 24, 25, 26, 28, 33, and 58.)

[38] Gustin, C., Manson, R., and Hughes, S. Spectral asymmetries in the resonance fluorescence of two-level systems under pulsed excitation. *Optics Letters* **43**, 779–782 (2018). URL https://opg.optica.org/ol/abstract.cfm?URI=ol-43-4-779. (Cited on pages 2 and 16.)

[39] Press, D., Ladd, T.D., Zhang, B., and Yamamoto, Y. Complete quantum control of a single quantum dot spin using ultrafast optical pulses. *Nature* **456**, 218–221 (2008). URL https://doi.org/10.1038/nature07530. (Cited on pages 2 and 23.)

[40] Stievater, T., Li, X., Steel, D.G., Gammon, D., Katzer, D., Park, D., Piermarocchi, C., and Sham, L. Rabi oscillations of excitons in single quantum dots. *Physical Review Letters* **87**, 133603 (2001). URL https://link.aps.org/doi/10.1103/PhysRevLett.87.133603. (Cited on pages 2, 19, and 23.)

[41] Zrenner, A., Beham, E., Stufler, S., Findeis, F., Bichler, M., and Abstreiter, G. Coherent properties of a two-level system based on a quantum-dot photodiode. *Nature* **418**, 612–614 (2002). URL https://doi.org/10.1038/nature00912. (Cited on pages 2, 3, 19, and 23.)

[42] Kok, P. and Lovett, B.W. *Introduction to Optical Quantum Information Processing* (Cambridge University Press, 2010). (Cited on page 2.)

[43] Carreño, J.L., Casalengua, E.Z., Laussy, F.P., and del Valle, E. Joint subnatural-linewidth and single-photon emission from resonance fluorescence. *Quantum Science and Technology* **3**, 045001 (2018). URL https://dx.doi.org/10.1088/2058-9565/aacfbe. (Cited on page 2.)

[44] Senellart, P., Solomon, G., and White, A. High-performance semiconductor quantum-dot single-photon sources. *Nature Nanotechnology* **12**, 1026–1039 (2017). URL https://doi.org/10.1038/nnano.2017.218. (Cited on pages 2, 3, 23, 36, and 37.)

[45] O'brien, J.L. Optical quantum computing. *Science* **318**, 1567–1570 (2007). URL https://doi.org/10.1126/science.1142892. (Cited on page 2.)

[46] Zhong, H.S., Wang, H., Deng, Y.H., Chen, M.C., Peng, L.C., Luo, Y.H., Qin, J., Wu, D., Ding, X., Hu, Y., et al. Quantum computational advantage using photons. *Science* **370**, 1460–1463 (2020). URL https://doi.org/10.1126/science.abe8770. (Cited on page 2.)

[47] Gisin, N. and Thew, R. Quantum communication. *Nature Photonics* **1**, 165–171 (2007). URL https://doi.org/10.1038/nphoton.2007.22. (Cited on page 2.)

[48] Chen, Y.A., Zhang, Q., Chen, T.Y., Cai, W.Q., Liao, S.K., Zhang, J., Chen, K., Yin, J., Ren, J.G., Chen, Z., et al. An integrated space-to-ground quantum communication network over 4,600 kilometres. *Nature* **589**, 214–219 (2021). URL https://doi.org/10.1038/s41586-020-03093-8. (Cited on page 2.)

[49] Ladd, T.D., Jelezko, F., Laflamme, R., Nakamura, Y., Monroe, C., and O'Brien, J.L. Quantum computers. *Nature* **464**, 45–53 (2010). URL https://doi.org/10.1038/nature08812. (Cited on page 2.)

[50] Aspuru-Guzik, A. and Walther, P. Photonic quantum simulators. *Nature Physics* **8**, 285–291 (2012). URL https://doi.org/10.1038/nphys2253. (Cited on page 2.)

[51] Hidary, J.D. and Hidary, J.D. *Quantum Computing: An Applied Approach*, vol. 1 (Springer, 2019). (Cited on page 2.)

[52] Pirandola, S., Bardhan, B.R., Gehring, T., Weedbrook, C., and Lloyd, S. Advances in photonic quantum sensing. *Nature Photonics* **12**, 724–733 (2018). URL https://doi.org/10.1038/s41566-018-0301-6. (Cited on page 2.)

[53] Stucki, D., Gisin, N., Guinnard, O., Ribordy, G., and Zbinden, H. Quantum key distribution over 67 km with a plug&play system. *New Journal of Physics* **4**, 41 (2002). URL https://iopscience.iop.org/article/10.1088/1367-2630/4/1/341/meta. (Cited on page 2.)

[54] Knill, E., Laflamme, R., and Milburn, G.J. A scheme for efficient quantum computation with linear optics. *Nature* **409**, 46–52 (2001). URL https://doi.org/10.1038/35051009. (Cited on pages 2 and 52.)

[55] He, Y.M., He, Y., Wei, Y.J., Wu, D., Atatüre, M., Schneider, C., Höfling, S., Kamp, M., Lu, C.Y., and Pan, J.W. On-demand semiconductor single-photon source with near-unity indistinguishability. *Nature Nanotechnology* **8**, 213–217 (2013). URL http://www.nature.com/articles/nnano.2012.262. (Cited on pages 2 and 38.)

[56] Kuhlmann, A.V., Prechtel, J.H., Houel, J., Ludwig, A., Reuter, D., Wieck, A.D., and Warburton, R.J. Transform-limited single photons from a single quantum dot. *Nature Communications* **6**, 8204 (2015). URL http://www.nature.com/doifinder/10.1038/ncomms9204. (Cited on pages 2 and 38.)

[57] Ardelt, P.L., Hanschke, L., Fischer, K.A., Müller, K., Kleinkauf, A., Koller, M., Bechtold, A., Simmet, T., Wierzbowski, J., Riedl, H., Abstreiter, G., and Finley, J.J. Dissipative preparation of the exciton and biexciton in self-assembled quantum dots on picosecond time scales. *Physical Review B* **90**, 241404 (2014). URL https://link.aps.org/doi/10.1103/PhysRevB.90.241404. (Cited on pages 2 and 38.)

[58] Reindl, M., Weber, J.H., Huber, D., Schimpf, C., Covre da Silva, S.F., Portalupi, S.L., Trotta, R., Michler, P., and Rastelli, A. Highly indistinguishable single photons from incoherently excited quantum dots. *Physical Review B* **100**, 155420 (2019). URL https://doi.org/10.1103/PhysRevB.100.155420https://link.aps.org/doi/10.1103/PhysRevB.100.155420. (Cited on pages 2 and 38.)

[59] Thomas, S.E., Billard, M., Coste, N., Wein, S.C., Priya, Ollivier, H., Krebs, O., Tazaïrt, L., Harouri, A., Lemaitre, A., Sagnes, I., Anton, C., Lanco, L., Somaschi, N., Loredo, J.C., and Senellart, P. Bright polarized single-photon source based on a linear dipole. *Physical Review Letters* **126**, 233601 (2021). URL https://link.aps.org/doi/10.1103/PhysRevLett.126.233601. (Cited on pages 2 and 38.)

[60] Ware, M.E., Stinaff, E.A., Gammon, D., Doty, M.F., Bracker, A.S., Gershoni, D., Korenev, V.L., Bădescu, i.m.c.C., Lyanda-Geller, Y., and Reinecke, T.L. Polarized fine structure in the photoluminescence excitation spectrum of a negatively charged quantum dot. *Physical Review Letters* **95**, 177403 (2005). URL https://link.aps.org/doi/10.1103/PhysRevLett.95.177403. (Cited on pages 2 and 38.)

[61] Cogan, D., Su, Z.E., Kenneth, O., and Gershoni, D. Deterministic generation of indistinguishable photons in a cluster state. *Nature Photonics* 1749–4893 (2023). URL https://doi.org/10.1038/s41566-022-01152-2. (Cited on pages 2, 37, 52, and 61.)

[62] He, Y.M., Wang, H., Wang, C., Chen, M.C., Ding, X., Qin, J., Duan, Z.C., Chen, S., Li, J.P., Liu, R.Z., Schneider, C., Atatüre, M., Höfling, S., Lu, C.Y., and Pan, J.W. Coherently driving a single quantum two-level system with

dichromatic laser pulses. *Nature Physics* **15**, 941–946 (2019). URL https://doi.org/10.1038/s41567-019-0585-6. (Cited on page 2.)

[63] Koong, Z.X., Scerri, E., Rambach, M., Cygorek, M., Brotons-Gisbert, M., Picard, R., Ma, Y., Park, S.I., Song, J.D., Gauger, E.M., and Gerardot, B.D. Coherent dynamics in quantum emitters under dichromatic excitation. *Physical Review Letters* **126**, 047403 (2021). URL https://doi.org/10.1103/PhysRevLett.126.047403. (Cited on page 2.)

[64] Brunner, K., Abstreiter, G., Böhm, G., Tränkle, G., and Weimann, G. Sharp-line photoluminescence and two-photon absorption of zero-dimensional biexcitons in a gaas/algaas structure. *Physical Review Letters* **73**, 1138–1141 (1994). URL https://link.aps.org/doi/10.1103/PhysRevLett.73.1138. (Cited on pages 2 and 38.)

[65] Schweickert, L., Jöns, K.D., Zeuner, K.D., Covre Da Silva, S.F., Huang, H., Lettner, T., Reindl, M., Zichi, J., Trotta, R., Rastelli, A., and Zwiller, V. On-demand generation of background-free single photons from a solid-state source. *Applied Physics Letters* **112**, 093106 (2018). URL http://aip.scitation.org/doi/10.1063/1.5020038. (Cited on pages 2, 3, 37, and 38.)

[66] Hanschke, L., Fischer, K.A., Appel, S., Lukin, D., Wierzbowski, J., Sun, S., Trivedi, R., Vučković, J., Finley, J.J., and Müller, K. Quantum dot single-photon sources with ultra-low multi-photon probability. *NPJ Quantum Information* **4**, 43 (2018). URL http://www.nature.com/articles/s41534-018-0092-0. (Cited on pages 2, 38, and 60.)

[67] Flagg, E.B., Muller, A., Robertson, J., Founta, S., Deppe, D., Xiao, M., Ma, W., Salamo, G., and Shih, C.K. Resonantly driven coherent oscillations in a solid-state quantum emitter. *Nature Physics* **5**, 203–207 (2009). URL https://doi.org/10.1038/nphys1184. (Cited on pages 2 and 38.)

[68] Simon, C. and Poizat, J.P. Creating Single Time-Bin-Entangled Photon Pairs. *Physical Review Letters* **94**, 030502 (2005). URL https://link.aps.org/doi/10.1103/PhysRevLett.94.030502. (Cited on pages 2 and 38.)

[69] Huber, T., Predojević, A., Zoubi, H., Jayakumar, H., Solomon, G.S., and Weihs, G. Measurement and modification of biexciton-exciton time correlations. *Optics Express* **21**, 9890–9898 (2013). URL https://doi.org/10.1364/OE.21.009890. (Cited on pages 2 and 38.)

[70] Sbresny, F., Hanschke, L., Schöll, E., Rauhaus, W., Scaparra, B., Boos, K., Zubizarreta Casalengua, E., Riedl, H., del Valle, E., Finley, J.J., Jöns, K.D., and Müller, K. Stimulated generation of indistinguishable single photons from a quantum ladder system. *Physical Review Letters* **128**, 093603 (2022). URL https://doi.org/10.1103/PhysRevLett.128.093603. (Cited on pages 2 and 38.)

[71] Gao, W.B., Fallahi, P., Togan, E., Miguel-Sanchez, J., and Imamoglu, A. Observation of entanglement between a quantum dot spin and a single photon. *Nature* **491**, 426–430 (2012). URL https://doi.org/10.1038/nature11573. (Cited on page 2.)

[72] Yang, Z., Gao, M., Wu, W., Yang, X., Sun, X.W., Zhang, J., Wang, H.C., Liu, R.S., Han, C.Y., Yang, H., et al. Recent advances in quantum dot-based light-emitting devices: Challenges and possible solutions. *Materials Today* **24**, 69–93 (2019). URL https://doi.org/10.1016/j.mattod.2018.09.002. (Cited on page 2.)

[73] Hepp, S., Jetter, M., Portalupi, S.L., and Michler, P. Semiconductor quantum dots for integrated quantum photonics. *Advanced Quantum Technologies* **2**, 1900020 (2019). URL https://doi.org/10.1002/qute.201900020. (Cited on page 2.)

[74] Bawendi, M., Brus, L., and Yekimov, A. The nobel prize in chemistry 2023: for the discovery and synthesis of quantum dots. https://www.nobelprize.org/prizes/chemistry/2023/summary/ (2023). (Cited on page 3.)

[75] Ramsay, A.J., Godden, T.M., Boyle, S.J., Gauger, E.M., Nazir, A., Lovett, B.W., Fox, A.M., and Skolnick, M.S. Phonon-induced rabi-frequency renormalization of optically driven single InGaAs/GaAs quantum dots. *Physical Review Letters* **105**, 177402 (2010). URL https://link.aps.org/doi/10.1103/PhysRevLett.105.177402. (Cited on pages 3, 13, 19, and 27.)

[76] Reiter, D.E., Kuhn, T., Glässl, M., and Axt, V.M. The role of phonons for exciton and biexciton generation in an optically driven quantum dot. *Journal of Physics: Condensed Matter* **26**, 423203 (2014). URL https://dx.doi.org/10.1088/0953-8984/26/42/423203. (Cited on page 3.)

[77] Zhou, X., Zhai, L., and Liu, J. Epitaxial quantum dots: a semiconductor launchpad for photonic quantum technologies. *Photonics Insights* **1**, R07 (2023). URL https://doi.org/10.3788/PI.2022.R07. (Cited on pages 3 and 23.)

[78] Gazzano, O., Michaelis de Vasconcellos, S., Arnold, C., Nowak, A., Galopin, E., Sagnes, I., Lanco, L., Lemaître, A., and Senellart, P. Bright solid-state sources of indistinguishable single photons. *Nature Communications* **4**, 1425 (2013). URL http://www.nature.com/ncomms/journal/v4/n2/full/ncomms2434. (Cited on pages 3 and 37.)

[79] Tomm, N., Javadi, A., Antoniadis, N.O., Najer, D., Löbl, M.C., Korsch, A.R., Schott, R., Valentin, S.R., Wieck, A.D., Ludwig, A., et al. A bright and fast source of coherent single photons. *Nature Nanotechnology* **16**, 399–403 (2021). URL https://doi.org/10.1038/s41565-020-00831-x. (Cited on pages 3 and 37.)

[80] Moreau, E., Robert, I., Gérard, J., Abram, I., Manin, L., and Thierry-Mieg, V. Single-mode solid-state single photon source based on isolated quantum dots in pillar microcavities. *Applied Physics Letters* **79**, 2865–2867 (2001). URL https://doi.org/10.1063/1.1415346. (Cited on pages 3 and 37.)

[81] Santori, C., Fattal, D., Vučković, J., Solomon, G.S., and Yamamoto, Y. Indistinguishable photons from a single-photon device. *Nature* **419**, 594–597 (2002). URL https://doi.org/10.1038/nature01086. (Cited on pages 3, 37, and 53.)

[82] Sun, S., Kim, H., Solomon, G.S., and Waks, E. A quantum phase switch between a single solid-state spin and a photon. *Nature Nanotechnology* **11**, 539–544 (2016). URL http://dx.doi.org/10.1038/nnano.2015.334. (Cited on page 3.)

[83] Greilich, A., Oulton, R., Zhukov, E.A., Yugova, I.A., Yakovlev, D.R., Bayer, M., Shabaev, A., Efros, A.L., Merkulov, I.A., Stavarache, V., Reuter, D., and Wieck, A. Optical control of spin coherence in singly charged (In,Ga)As/GaAs quantum dots. *Physical Review Letters* **96**, 227401 (2006). URL https://link.aps.org/doi/10.1103/PhysRevLett.96.227401. (Cited on page 3.)

[84] Delteil, A., Sun, Z., Gao, W.b., Togan, E., Faelt, S., and Imamoğlu, A. Generation of heralded entanglement between distant hole spins. *Nature Physics* **12**, 218–223 (2016). URL https://doi.org/10.1038/nphys3605. (Cited on page 3.)

[85] Stockill, R., Stanley, M.J., Huthmacher, L., Clarke, E., Hugues, M., Miller, A.J., Matthiesen, C., Le Gall, C., and Atatüre, M. Phase-Tuned Entangled State Generation between Distant Spin Qubits. *Physical Review Letters* **119**, 010503 (2017). URL https://doi.org/10.1103/PhysRevLett.119.010503. (Cited on page 3.)

[86] Schwartz, I., Cogan, D., Schmidgall, E.R., Don, Y., Gantz, L., Kenneth, O., Lindner, N.H., and Gershoni, D. Deterministic generation of a cluster state of

entangled photons. *Science* **354**, 434–437 (2016). URL https://doi.org/10.1126/science.aah4758. (Cited on pages 3, 37, and 61.)

[87] Istrati, D., Pilnyak, Y., Loredo, J.C., Antón, C., Somaschi, N., Hilaire, P., Ollivier, H., Esmann, M., Cohen, L., Vidro, L., Millet, C., Lemaître, A., Sagnes, I., Harouri, A., Lanco, L., Senellart, P., and Eisenberg, H.S. Sequential generation of linear cluster states from a single photon emitter. *Nature Communications* **11**, 1–8 (2020). URL https://doi.org/10.1038/s41467-020-19341-4. (Cited on pages 3 and 52.)

[88] Meng, Y., Faurby, C.F., Chan, M.L., Sund, P.I., Liu, Z., Wang, Y., Bart, N., Wieck, A.D., Ludwig, A., Midolo, L., et al. Photonic fusion of entangled resource states from a quantum emitter. *arXiv preprint arXiv:2312.09070* (2023). (Cited on pages 3 and 61.)

[89] Bracht, T.K., Cosacchi, M., Seidelmann, T., Cygorek, M., Vagov, A., Axt, V.M., Heindel, T., and Reiter, D.E. Swing-up of quantum emitter population using detuned pulses. *PRX Quantum* **2**, 040354 (2021). URL https://link.aps.org/doi/10.1103/PRXQuantum.2.040354. (Cited on pages 3, 35, 36, 38, 40, 44, 48, 55, and 58.)

[90] Boos, K., Kim, S.K., Bracht, T., Sbresny, F., Kaspari, J.M., Cygorek, M., Riedl, H., Bopp, F.W., Rauhaus, W., Calcagno, C., Finley, J.J., Reiter, D.E., and Müller, K. Signatures of dynamically dressed states. *Physical Review Letters* **132**, 053602 (2024). URL https://link.aps.org/doi/10.1103/PhysRevLett.132.053602. (Cited on pages 3, 16, 25, 28, and 33.)

[91] Boos, K., Sbresny, F., Kim, S.K., Kremser, M., Riedl, H., Bopp, F.W., Rauhaus, W., Scaparra, B., Jöns, K.D., Finley, J.J., Müller, K., and Hanschke, L. Coherent swing-up excitation for semiconductor quantum dots. *Advanced Quantum Technologies* 2300359 (2024). (Cited on pages 4, 36, 40, and 44.)

[92] Goldstein, L., Glas, F., Marzin, J., Charasse, M., and Le Roux, G. Growth by molecular beam epitaxy and characterization of inas/gaas strained-layer superlattices. *Applied Physics Letters* **47**, 1099–1101 (1985). (Cited on page 6.)

[93] Pohl, U.W. and Strittmatter, A. Control of self-organized in (ga) as/gaas quantum dot growth. In *Semiconductor Nanostructures (D. Bimberg)*, 41–65 (Springer, 2008). (Cited on pages 6 and 7.)

[94] Schöll, E. and Plaut, R.L. *Molecular Beam Epitaxy: Fundamentals and Current Status* (Springer, 2003). (Cited on page 6.)

[95] Findeis, F., Zrenner, A., Markmann, M., Böhm, G., and Abstreiter, G. Multi-exciton spectroscopy on a self-assembled ingaas/gaas quantum dot. *Physica E: Low-dimensional Systems and Nanostructures* **7**, 354–358 (2000). URL https://doi.org/10.1016/S1386-9477(99)00340-9. (Cited on page 6.)

[96] Fern, R. and Onton, A. Refractive index of alas. *Journal of Applied Physics* **42**, 3499–3500 (1971). URL https://doi.org/10.1063/1.1660760. (Cited on page 6.)

[97] Marple, D. Refractive index of gaas. *Journal of Applied Physics* **35**, 1241–1242 (1964). URL https://doi.org/10.1063/1.1713601. (Cited on page 6.)

[98] Bennett, B.R., Soref, R.A., and Del Alamo, J.A. Carrier-induced change in refractive index of inp, gaas and ingaasp. *IEEE Journal of Quantum Electronics* **26**, 113–122 (1990). URL https://doi.org/10.1109/3.44924. (Cited on page 6.)

[99] Talghader, J. and Smith, J. Thermal dependence of the refractive index of gaas and alas measured using semiconductor multilayer optical cavities. *Applied Physics Letters* **66**, 335–337 (1995). URL https://doi.org/10.1063/1.114204. (Cited on page 6.)

[100] Coldren, L.A., Corzine, S.W., and Mashanovitch, M.L. *Diode Lasers and Photonic Integrated Circuits* (John Wiley & Sons, 2012). (Cited on page 6.)

[101] Saleh, B.E. and Teich, M.C. *Fundamentals of Photonics* (John Wiley & sons, 2019). (Cited on page 6.)

[102] Krener, H. *Coherent Quantum Coupling of Excitons in Single Quantum Dots and Quantum Dot Molecules*. Ph.D. thesis, Technische Universität München (2013). (Cited on page 7.)

[103] Stranski, I.N. and Krastanow, L. Zur theorie der orientierten ausscheidung von ionenkristallen aufeinander. *Abhandlungen der Mathematisch-Naturwissenschaftlichen Klasse IIb* **146**, 797–810 (1938). (Cited on page 7.)

[104] Müller, K.M. *Optical Control of Quantum States in Artificial Atoms and Molecules*. Ph.D. thesis, Technische Universität München (2013). (Cited on pages 8, 11, and 66.)

[105] Fry, P., Finley, J., Wilson, L., Lemaitre, A., Mowbray, D., Skolnick, M., Hopkinson, M., Hill, G., and Clark, J. Electric-field-dependent carrier capture and escape in self-assembled inas/gaas quantum dots. *Applied Physics Letters*

77, 4344–4346 (2000). URL https://doi.org/10.1063/1.1334363. (Cited on pages 9 and 13.)

[106] Findeis, F., Baier, M., Beham, E., Zrenner, A., and Abstreiter, G. Photocurrent and photoluminescence of a single self-assembled quantum dot in electric fields. *Applied Physics Letters* **78**, 2958–2960 (2001). URL https://doi.org/10.1063/1.1369148. (Cited on pages 9 and 13.)

[107] Finley, J., Sabathil, M., Vogl, P., Abstreiter, G., Oulton, R., Tartakovskii, A., Mowbray, D., Skolnick, M., Liew, S., Cullis, A., et al. Quantum-confined stark shifts of charged exciton complexes in quantum dots. *Physical Review B* **70**, 201308 (2004). URL https://doi.org/10.1103/PhysRevB.70.201308. (Cited on pages 9 and 13.)

[108] Seidl, S., Kroner, M., Dalgarno, P.A., Högele, A., Smith, J.M., Ediger, M., Gerardot, B.D., Garcia, J.M., Petroff, P.M., Karrai, K., and Warburton, R.J. Absorption and photoluminescence spectroscopy on a single self-assembled charge-tunable quantum dot. *Physical Review B* **72**, 195339 (2005). URL https://link.aps.org/doi/10.1103/PhysRevB.72.195339. (Cited on page 9.)

[109] Warburton, R.J., Schäflein, C., Haft, D., Bickel, F., Lorke, A., Karrai, K., Garcia, J.M., Schoenfeld, W., and Petroff, P.M. Optical emission from a charge-tunable quantum ring. *Nature* **405**, 926–929 (2000). URL https://doi.org/10.1038/35016030. (Cited on pages 9 and 13.)

[110] Drexler, H., Leonard, D., Hansen, W., Kotthaus, J., and Petroff, P. Spectroscopy of quantum levels in charge-tunable ingaas quantum dots. *Physical Review Letters* **73**, 2252 (1994). URL https://doi.org/10.1103/PhysRevLett.73.2252. (Cited on page 9.)

[111] Findeis, F. *Optical Spectroscopy on Single Self-Assembled Quantum Dots*. Ph.D. thesis, Technische Universität München (2001). (Cited on page 9.)

[112] Grosso, G. and Parravicini, G.P. *Solid State Physics* (Academic Press, 2013). (Cited on page 11.)

[113] Streetman, B.G., Banerjee, S., et al. *Solid State Electronic Eevices*, vol. 4 (Prentice Hall New Jersey, 2000). (Cited on pages 11 and 12.)

[114] Sze, S.M. and Ng, K.K. *Physics of Semiconductor Devices* (Wiley, Hoboken, NJ, 2007). (Cited on page 11.)

[115] Ioffe Physical-Technical Institute of the Russian Academy of Sciences, x. Gallium arsenide. https://www.ioffe.ru/SVA/NSM/Semicond/GaAs/bandstr.html/ (2024). (Cited on page 11.)

[116] Ioffe Physical-Technical Institute of the Russian Academy of Sciences Ioffe, x. Ga in as - band structure and carrier concentration. https://www.ioffe.ru/SVA/NSM/Semicond/GaInAs/bandstr.html/ (2024). (Cited on page 11.)

[117] Michler, P. *Quantum Dots for Quantum Information Technologies* (Springer, 2017). (Cited on pages 12, 13, and 16.)

[118] Woggon, U. *Optical Properties of Semiconductor Quantum Dots*, vol. 136 (Springer, 1997). (Cited on page 12.)

[119] Warburton, R.J., Dürr, C.S., Karrai, K., Kotthaus, J.P., Medeiros-Ribeiro, G., and Petroff, P.M. Charged excitons in self-assembled semiconductor quantum dots. *Physical Review Letters* **79**, 5282–5285 (1997). URL https://link.aps.org/doi/10.1103/PhysRevLett.79.5282. (Cited on pages 12 and 13.)

[120] Klingshirn, C.F. *Semiconductor Optics* (Springer Science & Business Media, 2012). (Cited on page 12.)

[121] Warburton, R.J. Single spins in self-assembled quantum dots. *Nature Materials* **12**, 483–493 (2013). URL https://doi.org/10.1038/nmat3585. (Cited on pages 12 and 13.)

[122] Poem, E., Kodriano, Y., Tradonsky, C., Lindner, N., Gerardot, B., Petroff, P., and Gershoni, D. Accessing the dark exciton with light. *Nature Physics* **6**, 993–997 (2010). URL https://doi.org/10.1038/nphys1812. (Cited on page 12.)

[123] Schwartz, I., Schmidgall, E., Gantz, L., Cogan, D., Bordo, E., Don, Y., Zielinski, M., and Gershoni, D. Deterministic writing and control of the dark exciton spin using single short optical pulses. *Physical Review X* **5**, 011009 (2015). URL https://doi.org/10.1103/PhysRevX.5.011009. (Cited on page 12.)

[124] Schmidgall, E.R., Schwartz, I., Cogan, D., Gantz, L., Heindel, T., Reitzenstein, S., and Gershoni, D. All-optical depletion of dark excitons from a semiconductor quantum dot. *Applied Physics Letters* **106** (2015). URL https://doi.org/10.1063/1.4921000. (Cited on page 12.)

[125] Gantz, L., Schmidgall, E., Schwartz, I., Don, Y., Waks, E., Bahir, G., and Gershoni, D. Controlling the dark exciton spin eigenstates by external magnetic

field. *Physical Review B* **94**, 045426 (2016). URL https://doi.org/10.1103/PhysRevB.94.045426. (Cited on page 12.)

[126] Bayer, M., Ortner, G., Stern, O., Kuther, A., Gorbunov, A.A., Forchel, A., Hawrylak, P., Fafard, S., Hinzer, K., Reinecke, T.L., Walck, S.N., Reithmaier, J.P., Klopf, F., and Schäfer, F. Fine structure of neutral and charged excitons in self-assembled in(ga)as/(al)gaas quantum dots. *Physical Review B* **65**, 195315 (2002). URL https://link.aps.org/doi/10.1103/PhysRevB.65.195315. (Cited on pages 12, 13, and 14.)

[127] Finley, J., Ashmore, A., Lemaître, A., Mowbray, D., Skolnick, M., Itskevich, I., Maksym, P., Hopkinson, M., and Krauss, T. Charged and neutral exciton complexes in individual self-assembled in (ga) as quantum dots. *Physical Review B* **63**, 073307 (2001). URL https://doi.org/10.1103/PhysRevB.63.073307. (Cited on page 13.)

[128] Fry, P., Itskevich, I., Mowbray, D., Skolnick, M., Finley, J., Barker, J., O'Reilly, E., Wilson, L., Larkin, I., Maksym, P., et al. Inverted electron-hole alignment in inas-gaas self-assembled quantum dots. *Physical Review Letters* **84**, 733 (2000). URL https://doi.org/10.1103/PhysRevLett.84.733. (Cited on page 13.)

[129] Finley, J.J., Mowbray, D.J., Skolnick, M.S., Ashmore, A.D., Baker, C., Monte, A.F.G., and Hopkinson, M. Fine structure of charged and neutral excitons in inas-$al_{0.6}ga_{0.4}As$ quantum dots. *Physical Review B* **66**, 153316 (2002). URL https://link.aps.org/doi/10.1103/PhysRevB.66.153316. (Cited on page 14.)

[130] Meystre, P. and Sargent, M. *Elements of Quantum Optics* (Springer, 2007). (Cited on pages 16, 17, 20, and 22.)

[131] Steck, D.A. *Quantum and Atom Optics* (2007). URL http://steck.us/teaching. (Cited on pages 16, 17, 18, 19, 20, 21, 22, 51, and 52.)

[132] Cohen-Tannoudji, C., Dupont-Roc, J., and Grynberg, G. *Atom-photon interactions: basic processes and applications* (John Wiley & Sons, 1998). (Cited on page 17.)

[133] Fox, A.M. *Quantum Optics: An Introduction*, vol. 15 (Oxford University Press, 2006). (Cited on pages 19, 20, and 51.)

[134] Proakis, J.G., Salehi, M., Zhou, N., and Li, X. *Communication Systems Engineering*, vol. 2 (Prentice Hall New Jersey, 1994). (Cited on page 22.)

[135] Compton, R., Filin, A., Romanov, D.A., and Levis, R.J. Observation of broadband time-dependent rabi shifting in microplasmas. *Physical Review Letters* **103**, 205001 (2009). URL https://link.aps.org/doi/10.1103/PhysRevLett.103.205001. (Cited on page 24.)

[136] Compton, R., Filin, A., Romanov, D.A., and Levis, R.J. Dynamic rabi sidebands in laser-generated microplasmas: Tunability and control. *Physical Review A* **83**, 053423 (2011). URL https://link.aps.org/doi/10.1103/PhysRevA.83.053423. (Cited on page 24.)

[137] Fischer, K.A., Müller, K., Rundquist, A., Sarmiento, T., Piggott, A.Y., Kelaita, Y., Dory, C., Lagoudakis, K.G., and Vučković, J. Self-homodyne measurement of a dynamic mollow triplet in the solid state. *Nature Photonics* **10**, 163–166 (2016). URL https://doi.org/10.1038/nphoton.2015.276. (Cited on page 24.)

[138] Cosacchi, M., Cygorek, M., Ungar, F., Barth, A.M., Vagov, A., and Axt, V.M. Path-integral approach for nonequilibrium multitime correlation functions of open quantum systems coupled to markovian and non-markovian environments. *Physical Review B* **98**, 125302 (2018). URL https://link.aps.org/doi/10.1103/PhysRevB.98.125302. (Cited on page 25.)

[139] Cygorek, M., Cosacchi, M., Vagov, A., Axt, V.M., Lovett, B.W., Keeling, J., and Gauger, E.M. Simulation of open quantum systems by automated compression of arbitrary environments. *Nature Physics* **18**, 662–668 (2022). URL https://doi.org/10.1038/s41567-022-01544-9. (Cited on page 25.)

[140] Cygorek, M., Keeling, J., Lovett, B.W., and Gauger, E.M. Sublinear scaling in non-markovian open quantum systems simulations. *arXiv preprint arXiv:2304.05291* (2023). URL https://doi.org/10.48550/arXiv.2304.05291. (Cited on page 25.)

[141] Kaspari, J.M., Bracht, T.K., Boos, K., Kim, S.K., Sbresny, F., Mueller, K., and Reiter, D.E. Unveiling the interplay of mollow physics and perturbed free induction decay by nonlinear optical signals of a dynamically driven two-level system. *arXiv preprint arXiv:2311.14351* (2023). URL https://doi.org/10.48550/arXiv.2311.14351. (Cited on page 26.)

[142] Weiner, A.M., Heritage, J.P., and Kirschner, E.M. High-resolution femtosecond pulse shaping. *Journal of the Optical Society of America B* **5**, 1563–1572 (1988). URL https://opg.optica.org/josab/abstract.cfm?URI=josab-5-8-1563. (Cited on page 26.)

[143] Krügel, A., Axt, V.M., Kuhn, T., Machnikowski, P., and Vagov, A. The role of acoustic phonons for rabi oscillations in semiconductor quantum dots. *Applied Physics B* **81**, 897–904 (2005). URL https://doi.org/10.1007/s00340-005-1984-1. (Cited on page 27.)

[144] Besombes, L., Kheng, K., Marsal, L., and Mariette, H. Acoustic phonon broadening mechanism in single quantum dot emission. *Physical Review B* **63**, 155307 (2001). URL https://link.aps.org/doi/10.1103/PhysRevB.63.155307. (Cited on page 28.)

[145] Krummheuer, B., Axt, V.M., and Kuhn, T. Theory of pure dephasing and the resulting absorption line shape in semiconductor quantum dots. *Physical Review B* **65**, 195313 (2002). URL https://link.aps.org/doi/10.1103/PhysRevB.65.195313. (Cited on page 28.)

[146] Favero, I., Cassabois, G., Ferreira, R., Darson, D., Voisin, C., Tignon, J., Delalande, C., Bastard, G., Roussignol, P., and Gérard, J. Acoustic phonon sidebands in the emission line of single inas/gaas quantum dots. *Physical Review B* **68**, 233301 (2003). URL https://doi.org/10.1103/PhysRevB.68.233301. (Cited on page 28.)

[147] Liu, S., Gustin, C., Liu, H., Li, X., Yu, Y., Ni, H., Niu, Z., Hughes, S., Wang, X., and Liu, J. Dynamic resonance fluorescence in solid-state cavity quantum electrodynamics. *Nature Photonics* 1–7 (2024). URL https://doi.org/10.1038/s41566-023-01359-x. (Cited on pages 32 and 59.)

[148] Karli, Y., Kappe, F., Remesh, V., Bracht, T.K., Münzberg, J., Covre da Silva, S., Seidelmann, T., Axt, V.M., Rastelli, A., Reiter, D.E., and Weihs, G. Super scheme in action: Experimental demonstration of red-detuned excitation of a quantum emitter. *Nano Letters* **22**, 6567–6572 (2022). URL https://doi.org/10.1021/acs.nanolett.2c01783. (Cited on pages 35, 36, and 49.)

[149] Bracht, T.K., Seidelmann, T., Karli, Y., Kappe, F., Remesh, V., Weihs, G., Axt, V.M., and Reiter, D.E. Dressed-state analysis of two-color excitation schemes. *Physical Review B* **107**, 035425 (2023). URL https://doi.org/10.1103/PhysRevB.107.035425. (Cited on pages 36 and 40.)

[150] Bracht, T.K., Cygorek, M., Seidelmann, T., Axt, V.M., and Reiter, D.E. Temperature-independent almost perfect photon entanglement from quantum dots via the super scheme. *Optica Quantum* **1**, 103–107 (2023). URL https://opg.optica.org/opticaq/abstract.cfm?URI=opticaq-1-2-103. (Cited on page 36.)

[151] Joos, R., Bauer, S., Rupp, C., Kolatschek, S., Fischer, W., Nawrath, C., Vijayan, P., Sittig, R., Jetter, M., Portalupi, S.L., et al. Triggered telecom c-band single-photon source with high brightness, high indistinguishability and sub-ghz spectral linewidth. *arXiv* URL https://doi.org/10.48550/arXiv.2310.20647. (Cited on page 36.)

[152] Vannucci, L. and Gregersen, N. Highly efficient and indistinguishable single-photon sources via phonon-decoupled two-color excitation. *Physical Review B* **107**, 195306 (2023). URL https://link.aps.org/doi/10.1103/PhysRevB.107.195306. (Cited on page 36.)

[153] Heinisch, N., Köcher, N., Bauch, D., and Schumacher, S. Swing-up dynamics in quantum emitter cavity systems: Near ideal single photons and entangled photon pairs. *Physical Review Research* **6**, L012017 (2024). URL https://link.aps.org/doi/10.1103/PhysRevResearch.6.L012017. (Cited on page 36.)

[154] Raussendorf, R., Browne, D.E., and Briegel, H.J. Measurement-based quantum computation on cluster states. *Physical Review A* **68**, 022312 (2003). URL https://doi.org/10.1103/PhysRevA.68.022312. (Cited on pages 36 and 61.)

[155] Jozsa, R. An introduction to measurement based quantum computation. *NATO Science Series, III: Computer and Systems Sciences. Quantum Information Processing-From Theory to Experiment* **199**, 137–158 (2006). (Cited on page 36.)

[156] Briegel, H.J., Browne, D.E., Dür, W., Raussendorf, R., and Van den Nest, M. Measurement-based quantum computation. *Nature Physics* **5**, 19–26 (2009). URL https://doi.org/10.1038/nphys1157. (Cited on page 36.)

[157] Economou, S.E., Lindner, N., and Rudolph, T. Optically generated 2-dimensional photonic cluster state from coupled quantum dots. *Physical Review Letters* **105**, 093601 (2010). URL https://doi.org/10.1103/PhysRevLett.105.093601. (Cited on page 36.)

[158] Gimeno-Segovia, M., Shadbolt, P., Browne, D.E., and Rudolph, T. From three-photon greenberger-horne-zeilinger states to ballistic universal quantum computation. *Physical Review Letters* **115**, 020502 (2015). URL https://link.aps.org/doi/10.1103/PhysRevLett.115.020502. (Cited on pages 36 and 52.)

[159] Lodahl, P. Quantum-dot based photonic quantum networks. *Quantum Science and Technology* **3**, 013001 (2017). URL https://dx.doi.org/10.1088/2058-9565/aa91bb. (Cited on page 36.)

[160] Couteau, C., Barz, S., Durt, T., Gerrits, T., Huwer, J., Prevedel, R., Rarity, J., Shields, A., and Weihs, G. Applications of single photons to quantum communication and computing. *Nature Reviews Physics* **5**, 326–338 (2023). URL https://doi.org/10.1038/s42254-023-00583-2. (Cited on page 36.)

[161] Azuma, K., Tamaki, K., and Lo, H.K. All-photonic quantum repeaters. *Nature Communications* **6**, 1–7 (2015). URL https://doi.org/10.1038/ncomms7787. (Cited on pages 36 and 61.)

[162] Russo, A., Barnes, E., and Economou, S.E. Generation of arbitrary all-photonic graph states from quantum emitters. *New Journal of Physics* **21**, 055002 (2019). URL https://dx.doi.org/10.1088/1367-2630/ab193d. (Cited on pages 36 and 52.)

[163] Azuma, K., Economou, S.E., Elkouss, D., Hilaire, P., Jiang, L., Lo, H.K., and Tzitrin, I. Quantum repeaters: From quantum networks to the quantum internet. *Review of Modern Physics* **95**, 045006 (2023). URL https://link.aps.org/doi/10.1103/RevModPhys.95.045006. (Cited on pages 36 and 52.)

[164] Trivedi, R., Fischer, K.A., Vučković, J., and Müller, K. Generation of non-classical light using semiconductor quantum dots. *Advanced Quantum Technologies* **3**, 1900007 (2020). URL https://onlinelibrary.wiley.com/doi/abs/10.1002/qute.201900007. (Cited on pages 36 and 51.)

[165] Michler, P. and Portalupi, S.L. *Semiconductor Quantum Light Sources: Fundamentals, Technologies and Devices* (Walter de Gruyter GmbH & Co KG, 2024). (Cited on page 36.)

[166] Hong, C.K., Ou, Z.Y., and Mandel, L. Measurement of subpicosecond time intervals between two photons by interference. *Physical Review Letters* **59**, 2044–2046 (1987). (Cited on pages 36, 52, and 74.)

[167] Lindner, N.H. and Rudolph, T. Proposal for pulsed on-demand sources of photonic cluster state strings. *Physical Review Letters* **103**, 113602 (2009). URL https://doi.org/10.1103/PhysRevLett.103.113602. (Cited on pages 37 and 61.)

[168] Thomas, P., Ruscio, L., Morin, O., and Rempe, G. Efficient generation of entangled multiphoton graph states from a single atom. *Nature* **608**, 677–681 (2022). URL https://doi.org/10.1038/s41586-022-04987-5. (Cited on page 37.)

[169] Coste, N., Fioretto, D., Belabas, N., Wein, S., Hilaire, P., Frantzeskakis, R., Gundin, M., Goes, B., Somaschi, N., Morassi, M., et al. High-rate entanglement between a semiconductor spin and indistinguishable photons. *Nature Photonics* **17**, 582–587 (2023). URL https://doi.org/10.1038/s41566-023-01186-0. (Cited on pages 37, 38, and 61.)

[170] Schöll, E., Schweickert, L., Hanschke, L., Zeuner, K.D., Sbresny, F., Lettner, T., Trivedi, R., Reindl, M., Covre da Silva, S.F., Trotta, R., Finley, J.J., Vučković, J., Müller, K., Rastelli, A., Zwiller, V., and Jöns, K.D. Crux of using the cascaded emission of a three-level quantum ladder system to generate indistinguishable photons. *Physical Review Letters* **125**, 233605 (2020). URL https://link.aps.org/doi/10.1103/PhysRevLett.125.233605. (Cited on page 38.)

[171] Cogan, D., Su, Z.E., Kenneth, O., and Gershoni, D. A deterministic source of indistinguishable photons in a cluster state. *arXiv* (2021). URL https://arxiv.org/abs/2110.05908. (Cited on page 38.)

[172] Fischer, K.A., Hanschke, L., Wierzbowski, J., Simmet, T., Dory, C., Finley, J.J., Vučković, J., and Müller, K. Signatures of two-photon pulses from a quantum two-level system. *Nature Physics* **13**, 649–654 (2017). URL https://doi.org/10.1038/nphys4052. (Cited on pages 46 and 60.)

[173] Davanco, M., Rakher, M.T., Wegscheider, W., Schuh, D., Badolato, A., and Srinivasan, K. Efficient quantum dot single photon extraction into an optical fiber using a nanophotonic directional coupler. *Applied Physics Letters* **99** (2011). URL https://doi.org/10.1063/1.3617472. (Cited on pages 50 and 60.)

[174] Hanbury Brown, R. and Twiss, R. A test of a new type of stellar interferometer on sirius. *Nature* **178**, 1046–1048 (1956). (Cited on pages 51 and 71.)

[175] Fischer, K.A., Hanschke, L., Kremser, M., Finley, J.J., Müller, K., and Vučković, J. Pulsed Rabi oscillations in quantum two-level systems: beyond the area theorem. *Quantum Science and Technology* **3**, 014006 (2018). URL https://iopscience.iop.org/article/10.1088/2058-9565/aa9269. (Cited on pages 52 and 60.)

[176] Browne, D.E. and Rudolph, T. Resource-efficient linear optical quantum computation. *Physical Review Letters* **95**, 010501 (2005). URL https://link.aps.org/doi/10.1103/PhysRevLett.95.010501. (Cited on page 52.)

[177] Kiesel, N., Schmid, C., Weber, U., Tóth, G., Gühne, O., Ursin, R., and Weinfurter, H. Experimental analysis of a four-qubit photon cluster state. *Physical Review Letters* **95**, 210502 (2005). URL https://link.aps.org/doi/10.1103/PhysRevLett.95.210502. (Cited on page 52.)

[178] Chen, K., Li, C.M., Zhang, Q., Chen, Y.A., Goebel, A., Chen, S., Mair, A., and Pan, J.W. Experimental realization of one-way quantum computing with two-photon four-qubit cluster states. *Physical Review Letters* **99**, 120503 (2007). URL https://link.aps.org/doi/10.1103/PhysRevLett.99.120503. (Cited on page 52.)

[179] Somaschi, N., Giesz, V., De Santis, L., Loredo, J., Almeida, M.P., Hornecker, G., Portalupi, S.L., Grange, T., Anton, C., Demory, J., et al. Near-optimal single-photon sources in the solid state. *Nature Photonics* **10**, 340–345 (2016). URL https://doi.org/10.1038/nphoton.2016.23. (Cited on page 53.)

[180] Schöll, E., Schweickert, L., Hanschke, L., Zeuner, K.D., Sbresny, F., Lettner, T., Trivedi, R., Reindl, M., Covre Da Silva, S.F., Trotta, R., Finley, J.J., Vučković, J., Müller, K., Rastelli, A., Zwiller, V., and Jöns, K.D. Crux of using the cascaded emission of a three-level quantum ladder system to generate indistinguishable photons. *Physical Review Letters* **125**, 233605 (2020). URL https://link.aps.org/doi/10.1103/PhysRevLett.125.233605. (Cited on page 54.)

[181] Loredo, J., Antón, C., Reznychenko, B., Hilaire, P., Harouri, A., Millet, C., Ollivier, H., Somaschi, N., De Santis, L., Lemaître, A., et al. Generation of non-classical light in a photon-number superposition. *Nature Photonics* **13**, 803–808 (2019). URL https://doi.org/10.1038/s41566-019-0506-3. (Cited on pages 54 and 55.)

[182] Gonzalez-Tudela, A., Laussy, F.P., Tejedor, C., Hartmann, M.J., and Del Valle, E. Two-photon spectra of quantum emitters. *New Journal of Physics* **15**, 033036 (2013). URL https://10.1088/1367-2630/15/3/033036. (Cited on page 59.)

[183] Peiris, M., Petrak, B., Konthasinghe, K., Yu, Y., Niu, Z., and Muller, A. Two-color photon correlations of the light scattered by a quantum dot. *Physical Review B* **91**, 195125 (2015). URL https://doi.org/10.1103/PhysRevB.91.195125. (Cited on page 59.)

[184] Muñoz, C.S., Del Valle, E., Tudela, A.G., Müller, K., Lichtmannecker, S., Kaniber, M., Tejedor, C., Finley, J., and Laussy, F. Emitters of n-photon

bundles. *Nature Photonics* **8**, 550–555 (2014). URL https://doi.org/10.1038/nphoton.2014.114. (Cited on page 60.)

[185] Afek, I., Ambar, O., and Silberberg, Y. High-noon states by mixing quantum and classical light. *Science* **328**, 879–881 (2010). URL https://www.science.org/doi/abs/10.1126/science.1188172. (Cited on page 60.)

[186] Denk, W., Strickler, J., and Webb, W. Two-photon laser scanning fluorescence microscopy. *Science* **248**, 73–76 (1990). URL https://www.science.org/doi/abs/10.1126/science.2321027. (Cited on page 60.)

[187] Horton, N., Wang, K., Kobat, D., Clark, C., Wise, F., Schaffer, C., and Xu, C. In vivo three-photon microscopy of subcortical structures within an intact mouse brain. *Nature Photonics* **7**, 205–209 (2013). URL https://doi.org/10.1038/nphoton.2012.336. (Cited on page 60.)

[188] Giovannetti, V., Lloyd, S., and Maccone, L. Quantum-enhanced measurements: Beating the standard quantum limit. *Science* **306**, 1330–1336 (2004). URL https://www.science.org/doi/abs/10.1126/science.1104149. (Cited on page 60.)

[189] Peiris, M., Konthasinghe, K., and Muller, A. Franson interference generated by a two-level system. *Physical Review Letters* **118**, 030501 (2017). URL https://doi.org/10.1103/PhysRevLett.118.030501. (Cited on page 60.)

[190] Carreño, J.C.L., Feijoo, S.B., and Stobińska, M. Entanglement in resonance fluorescence. *arXiv preprint arXiv:2302.04059* (2023). URL https://doi.org/10.48550/arXiv.2302.04059. (Cited on page 60.)

[191] Schall, J., Deconinck, M., Bart, N., Florian, M., von Helversen, M., Dangel, C., Schmidt, R., Bremer, L., Bopp, F., Hüllen, I., et al. Bright electrically controllable quantum-dot-molecule devices fabricated by in situ electron-beam lithography. *Advanced Quantum Technologies* **4**, 2100002 (2021). URL https://doi.org/10.1002/qute.202100002. (Cited on page 60.)

[192] Abudayyeh, H., Lubotzky, B., Blake, A., Wang, J., Majumder, S., Hu, Z., Kim, Y., Htoon, H., Bose, R., Malko, A.V., et al. Single photon sources with near unity collection efficiencies by deterministic placement of quantum dots in nanoantennas. *APL Photonics* **6** (2021). URL abudayyeh2021. (Cited on page 60.)

[193] Barbiero, A., Shooter, G., Muller, T., Skiba-Szymanska, J., Stevenson, R.M., Goff, L.E., Ritchie, D.A., and Shields, A.J. Polarization-selective enhancement of telecom wavelength quantum dot transitions in an elliptical bullseye resonator. *Nano Letters* **24**, 2839–2845 (2024). URL https://doi.org/10.1021/acs.nanolett.3c04987. (Cited on page 60.)

[194] Xiong, K., Li, X., Wei, Y., Wu, W., Zhang, C., Liu, J., Chen, Y., and Chen, P. Efficient generation of single photons by quantum dots embedded in bullseye cavities with backside dielectric mirrors. *Optics Express* **31**, 19536–19543 (2023). URL https://doi.org/10.1364/OE.492962. (Cited on page 60.)

[195] Löbl, M.C., Söllner, I., Javadi, A., Pregnolato, T., Schott, R., Midolo, L., Kuhlmann, A.V., Stobbe, S., Wieck, A.D., Lodahl, P., et al. Narrow optical linewidths and spin pumping on charge-tunable close-to-surface self-assembled quantum dots in an ultrathin diode. *Physical Review B* **96**, 165440 (2017). URL https://doi.org/10.1103/PhysRevB.96.165440. (Cited on page 60.)

[196] Nowak, A., Portalupi, S., Giesz, V., Gazzano, O., Dal Savio, C., Braun, P.F., Karrai, K., Arnold, C., Lanco, L., Sagnes, I., et al. Deterministic and electrically tunable bright single-photon source. *Nature Communications* **5**, 3240 (2014). URL https://doi.org/10.1038/ncomms4240. (Cited on page 60.)

[197] Buterakos, D., Barnes, E., and Economou, S.E. Deterministic generation of all-photonic quantum repeaters from solid-state emitters. *Physical Review X* **7**, 041023 (2017). URL https://link.aps.org/doi/10.1103/PhysRevX.7.041023. (Cited on page 61.)

[198] Novotny, L., Grober, R.D., and Karrai, K. Reflected image of a strongly focused spot. *Optics Letters* **26**, 789–791 (2001). URL https://doi.org/10.1364/OL.26.000789. (Cited on page 67.)

[199] Bopp, F.W. *Electrical, Magnetic and Optical Control of an Artificial Molecule*. Ph.D. thesis, Technische Universität München (2023). (Cited on page 71.)

[200] Thoma, A., Schnauber, P., Gschrey, M., Seifried, M., Wolters, J., Schulze, J.H., Strittmatter, A., Rodt, S., Carmele, A., Knorr, A., Heindel, T., and Reitzenstein, S. Exploring dephasing of a solid-state quantum emitter via time- and temperature-dependent hong-ou-mandel experiments. *Physical Review Letters* **116**, 033601 (2016). URL https://link.aps.org/doi/10.1103/PhysRevLett.116.033601. (Cited on page 72.)

List of publications

Chris Gustin*, Lukas Hanschke*, **Katarina Boos***, Jonathan R. A. Müller, Malte Kremser, Jonathan J. Finley, Stephen Hughes, and Kai Müller
High-resolution spectroscopy of a quantum dot driven bichromatically by two strong coherent fields, Physical Review Research **3**, 013044 (2021)
https://doi.org/10.1103/PhysRevLett.128.093603

Friedrich Sbresny*, Lukas Hanschke*, Eva Schöll, William Rauhaus, Bianca Scaparra, **Katarina Boos**, Eduardo Zubizarreta Casalengua, Hubert Riedl, Elena del Valle, Jonathan J. Finley, Klaus D. Jöns, and Kai Müller
Stimulated Generation of Indistinguishable Single Photons from a Quantum Ladder System, Physical Review Letters **128**, 093603 (2022)
https://doi.org/10.1103/PhysRevLett.128.093603

Frederik Bopp, Jonathan Rojas, Natalia Revenga, Hubert Riedl, Friedrich Sbresny, **Katarina Boos**, Tobias Simmet, Arash Ahmadi, David Gershoni, Jacek Kasprzak, Arne Ludwig, Stephan Reitzenstein, Andreas Wieck, Dirk Reuter, Kai Müller, Jonathan J. Finley
Quantum Dot Molecule Devices with Optical Control of Charge Status and Electronic Control of Coupling , Advanced Quantum Technologies 2270101 (2022)
https://doi.org/10.1002/qute.202270101

Frederik Bopp, Johannes Schall, Nikolai Bart, Florian Vögl, Charlotte Cullip, Friedrich Sbresny, **Katarina Boos**, Christopher Thalacker, Michelle Lienhart, Sven Rodt, Dirk Reuter, Arne Ludwig, Andreas D. Wieck, Stephan Reitzenstein, Kai Müller, and Jonathan J. Finley
Coherent driving of direct and indirect excitons in a quantum dot molecule, Physical Review B **107**, 165426 (2023)
https://doi.org/10.1103/PhysRevB.107.165426

Katarina Boos*, Friedrich Sbresny*, Sang Kyu Kim*, Malte Kremser, Hubert Riedl, Frederik W. Bopp, William Rauhaus, Bianca Scaparra, Klaus Jöns, Jonathan J. Finley, Kai Müller, and Lukas Hanschke
Coherent Swing-Up Excitation for Semiconductor Quantum Dots, Advanced Quantum Technologies 2300359 (2024)
https://doi.org/10.1002/qute.202300359

Katarina Boos*, Sang Kyu Kim*, Thomas Bracht, Friedrich Sbresny, Jan M. Kaspari, Moritz Cygorek, Hubert Riedl, Frederik W. Bopp, William Rauhaus, Carolin Calcagno, Jonathan J. Finley, Doris E. Reiter, and Kai Müller
Signatures of Dynamically Dressed States, Physical Review Letters **132**, 053602 (2024)
https://doi.org/10.1103/PhysRevLett.132.053602

Jan M. Kaspari, Thomas K. Bracht, **Katarina Boos**, Sang Kyu Kim, Friedrich Sbresny, Kai Müller, and Doris E. Reiter
Unveiling the interplay of Mollow physics and perturbed free induction decay by nonlinear optical signals of a dynamically driven two-level system, Physical Review Research (accepted 2024)
https://doi.org/10.48550/arXiv.2311.14351

Frederik Bopp, Charlotte Cullip, Christopher Thalacker, Michelle Lienhart, Johannes Schall, Nikolai Bart, Friedrich Sbresny, **Katarina Boos**, Sven Rodt, Dirk Reuter, Arne Ludwig, Andreas D. Wieck, Stephan Reitzenstein, Filippo Troiani, Guido Goldoni, Elisa Molinari, Kai Müller, Jonathan J. Finley
Magnetic tuning of the tunnel coupling in an optically active quantum dot molecule, arXiv, 2303.12552 (submitted to Physical Review Letters 2023)
https://doi.org/10.48550/arXiv.2303.12552

Acknowledgements

I would like to express my heartfelt gratitude and acknowledge all those people without whom this work would have hardly been possible and my PhD time definitely would not have been the same.

First of all, I want to thank my supervisor, **Kai Müller**, for giving me the opportunity to pursue my doctoral research in his group, particularly as a part of the QD team. Kai, thanks for being such a great supervisor! It was great having the freedom to choose my own projects while still always being able to discuss ideas, measurement results or basic physics concepts with you. Moreover, I very much appreciate the chance to spend several months in Canada.

A special thanks to **Friedrich Sbresny**, for being a great friend and colleague through all these PhD and covid years. Working with you was fun, whether we were building up (or accidentally breaking) equipment in the lab during the pandemic, supervising students, discussing physics politics, or debating over the pellicle mount. I even kind of got used to your taste of music :) But seriously, I truly value our teamwork, it was a great balance between working together on diverse projects while sharing and dividing responsibilities and tasks, and always helping each other out.

Sang Kyu Kim, thank you for your tireless work and big contributions to both of my projects. I greatly appreciate your constant availability and willingness to help with literally anything, along, of course, with your exchange of the best restaurant and coffee recommendations in Munich. I hope that the RF stick doesn't let you down either and that you have a great time during the rest of your PhD!

Frederik Bopp, thanks for always being there, or across the hallway, to discuss physics, setups or life in general :) Your support and encouragement during various stages during my phd has meant a lot to me. Thanks as well for all the fun time and a lot of great laughs during walks and coffee breaks, at various conferences, or while drinking wine or bouldering.

Big thanks to my QD team colleagues **Lukas Hanschke, William Rauhaus** and **Carolin Calcagno** for all their help and support, and for making the time in the lab and during various other occasions outside of it so enjoyable. Thanks **Lukas**, for the blessing and curse of passing me all your responsibilities including RF stick, office place, lab course and WSI coffee machine ;) **Willy**, thanks for introducing me to all the fab processes with such great patience and attention to detail.

Thank you to **Marko Petrić, Bianca Scaparra, Matteo Barbone, Eduardo Zubizarreta-Casalengua, Malte Kremser,** and the whole **QEC** and former **QC group** for so many things I can't even count. Malte, thanks so much for fabricating the diodes on that one sample a decade ago, that eventually contained the one QD on which all measurements were performed. Thanks to all, in particular, for great lunch and coffee breaks, several wonderful times in Mauterndorf, and your unwavering support, especially when things weren't going as planned.

To **Jon Finley**, **E24**, and the whole **WSI**, thank you for upholding a great working environment at the institute. Big thanks to everyone sharing their equipment and taking care of devices in common use, particularly the ungrateful ones.

A special thanks to **Hubert Riedl** and **Ade Ziegeltrum** for their tireless work at the WSI, ensuring that everything ran smoothly without ever letting yourselves get rattled by anything. Thanks as well for great and fun chats and all your support for N107 in particular! Hubert, thank you for all your work on the MBE and for growing all those QD samples back in the days.

Claudia, **Linda**, **Lisa**, **Mina** and all the rest of the **WSI** and **Zeit employees**, thanks so much for keeping the institute running. Huge thanks, **Daniela**, for your tireless fight with the Reisekostenstelle and for what turned into endless chats every time I just intended to drop something off at your office. And many thanks to **Hannes** and **Nick**, for your patience with my hand-drawn technical drawings which with your help became some essential parts of our setups.

My thanks go to **Thomas Bracht** and **Doris Reiter** at the Dortmund university, along with the entire theory team, for your significant contribution to my main projects, both intentional and unintentional. It was great collaborating with you!

Big thanks to **Daniel Higginbottom** and **Stephanie Simmons** from Simon Fraser

University in Vancouver, for welcoming and including me so warmly into the SQT group for three month, which made the experience very productive and enjoyable.

Camille Bowness, **Michael Dobinson** and **Nick Brunelle**, thanks for an amazingly fun teamwork on a project which shall remain confidential :) Thanks for the great time and for teaching me so many things about T-centres. And with that big thanks as well to the whole **SQT group** and my grotto office-mates for a wonderful time, numerous discussions about physics, cats and everything else. I miss you!

Lastly, I extend my sincere thanks to **my family** and **friends**, besides my colleagues, for your relentless support and belief in me, during the PhD and all of the 11 years of my physics career. Special thanks to **Isabel Wallace** and **Adina Klink** for helping me navigate critical situations with a refreshing outside perspective. Thanks for listening to lots of complaints and unnecessarily detailed stories, for lengthly discussions about phd life issues and, of course, for celebrating my successes with me!